Northumbria Research Link

Northumbria Research Link

Orthogonal Frequency Division Multiplexing for Indoor Visible Light Communication Links

Osama Dhawi Saied

PhD

2018

Orthogonal Frequency Division Multiplexing for Indoor Visible Light Communication Links

By

Osama Dhawi Saied

A thesis submitted in partial fulfilment of the requirements

of the University of Northumbria at Newcastle for the

degree of Doctor of Philosophy

Research undertaken in the School of Computing,

Engineering and Information Sciences

February 2018

I dedicate this work to my family

Declaration

I declare that the work contained in this thesis has not been submitted for any other award and that it is all my own work. I also confirm that this work fully acknowledges opinions, ideas and contributions from the work of others.

I declare that the Word Count of this Thesis is 40957 words

Name: Osama Saied

Signature:

Date: 22/10/2018

Acknowledgment

First and foremost, I would like to thank my principal supervisor Professor Zabih Ghassemlooy for providing me endless support, guidance and encouragement throughout my research work. Ghassemlooy offered his full confidence, enthusiasm and showed a lot of patience toward me at every turn.

I wish to express my gratitude to Northumbria University, Mathematics, Physics and Electrical Engineering centre and all wonderful people who I met during this journey. I would also like to thank the Libyan Ministry of Higher Education and Scientific Research for their financial support.

I wish to thank, Dr Hoa Le-Minh and Dr Sujan Rajbhandari for their help and support as well as I am also grateful for all help from Optical Communication Research Group (ORCG) members.

Last but not the least, I hereby would like to offer my heartfelt thanks to my family and friends, especially to my parents and my wife. They never left my back and removed the happy encouraging smile from their faces.

Abstract

Visible light communications (VLC) is an attractive technique that uses white light emitting diodes (WLEDs) to provide illumination, data communications and indoor localization. The modulation bandwidth of WLEDs is limited to a few MHz, due to the long photoluminescence lifetime of yellow phosphors. Orthogonal frequency division multiplexing (OFDM) has been extensively investigated in VLC systems to compensate the limited LED bandwidth, along with the capability of improving the performance at frequencies beyond the 3dB modulation bandwidth.

In intensity modulation and direct detection (IM/DD) based VLC systems, the complex and bipolar signal formats, such as the traditional OFDM, cannot be used. Therefore, a DC-biased optical OFDM (DCO-OFDM), and asymmetrically clipped optical OFDM (ACO-OFDM) are proposed. However, the use of DCO-OFDM comes at the cost of reduced power efficiency, while the adoption of ACO-OFDM results in reducing the spectral efficiency.

Despite the OFDM advantages, its performance is adversely affected by non-linear distortion (from LEDs) due to its high peak to average power ratio (PAPR). Recently, interleaving frequency division multiple access (IFDMA) used in IM/DD is been proposed as a modified optical OFDM scheme to address the PAPR issue. However, this scheme is still not satisfying the PAPR reduction level as compared with the single carrier modulation such as OOK. Therefore, the two main aims of this research are to increase the ACO-OFDM data rates as well as to further improve the IFDMA PAPR for IM/DD based VLC systems.

The first aim is achieved by reducing the ACO-OFDM symbol duration, where only the first half of the asymmetrical ACO-OFDM time domain symbol is used to carry the data samples, after inverting its negative samples to positive ones to meet the IM/DD requirements. Two schemes have been proposed in this research to identify the positions of the inverted samples at the receiver side. The schemes are known as the pilot aided ACO-OFDM (PA-ACO-OFDM) scheme and the position encoded-ACO-OFDM (PE-ACO-OFDM) scheme. Simulation results show that data rates of the proposed schemes are enhanced by up to 33% compared to the traditional ACO-OFDM scheme.

The second aim is achieved by adapting the IFDMA scheme for IM/DD based VLC systems in three innovative ways, resulting in a new unipolar modified OFDM scheme known as unipolar pulse amplitude modulation frequency division multiplexing (U-PAM-FDM), and two bipolar modified OFDM schemes known as the bipolar pulse amplitude modulation frequency division multiplexing (B-PAM-FDM), and the optical interleaved frequency division multiplexing (OIFDM) schemes. As such UPAM-FDM proposed to address the PAPR of the unipolar OFDM schemes (i.e. ACO-OFDM) while the B-PAM-FDM and OIFDM are presented to reduce the PAPR of the bipolar OFDM schemes (i.e. DCO-OFDM).

Simulation results show that the PAPR of ACO-OFDM is reduced by 3.8 dB when U-PAM-FDM is considered. They also demonstrate that the PAPR value of DCO-OFDM is reduced by 7 dB and 10 dB when B-PAM-FDM and OIFDM are implemented respectively. Furthermore, the reduction in the PAPR value for U-PAM-FDM and B-PAM-FDM has been experimentally investigated, where the results show that the B-PAM-FDM and U-PAM-FDM can provide 2 dBm and 3 dBm higher average transmitted power compared to ACO-OFDM and DCO-OFDM respectively. For B-PAM-FDM, further investigation has been experimentally carried out in terms of the achievable maximum distance between the transmitter (Tx) and the receiver (Rx). The results show that a 44% increase in the distance between the Tx and the Rx can be attained in comparison with DCO-OFDM.

Table of Contents

List of Figures

List of Tables

Glossary of Abbreviations

5G	Fifth generation
(M-PAM)	Multi-level pulse amplitude modulation
AC	Alternative Current
ACO-OFDM	Asymmetrically clipped optical OFDM
ACO-SCFDE	ACO-Single Carrier Frequency Domain Equalization
ADC	Analog to Digital Converter
APD	Avalanche PD
AWGN	Additive white Gaussian noise
BER	Bit error rate
B-PAM-FDM	Bipolar pulse amplitude modulation frequency division multiplexing
C2C	Car-to-car
C2I	Car-to-infrastructure
CCDF	Complementary cumulative distribution Function
CDS	Channel-dependant scheduling
Ce:YAG	Yellowish cerium doped yttrium aluminium garnet
CP	Cyclic prefix
CRI	Colour rendering index
CT	Colour temperature
DAB	Digital audio broadcasting
DAC	Digital to analogue converters
DACDR	DAC dynamic range
DC	Direct Current
DCO-OFDM	DC-biased optical OFDM
DSL	Digital subscriber line
DTV	Digital television
DUC	Digitally up-converted
EOC	Electrical to Optical Converter
EVM	Error vector magnitude
FDM	Frequency division multiplexing
FFT	Fast Fourier Transform
GaN	Gallium nitride

GHz	Giga Hertz
HS	Hermitian Symmetry
ICI	Inter channel interference
IDP	Intensity demodulation process
IFDMA	Interleaved frequency division multiple access
IFFT	Inverse Fast Fourier Transform
IM/DD	Intensity modulation/Direct detection
IMP	Intensity modulation process
IOT	Internet of things
IR	Infrared
ISI	Inter symbol interference
LED	Light emitting diode
LFDMA	Localized frequency division multiple access
lm/W	lm/W
LOS	Line of sight
LPF	Low pass filter
LS	least square
LTE	Long term evaluation
M2M	Machine-to-machine
MCM	Multi-carrier modulation
MHz	Mega Hertz
MIMO	Multi input multi output
MMSE	Minimum mean square error algorithm
M-PPM	Multi-level pulse position modulation
MSPS	Mega samples per second
NLOS	Non line of sight
NRZ	Non-return to zero
NSs	Negative samples
OFDM	Orthogonal frequency division multiplexing
OIFDM	Optical interleaved frequency division multiplexing
OLEDs	Organic LEDs
O-OFDM	Optical OFDM
OOK	ON-Off-Keying
OWC	Optical wireless communications
P/S	Parallel to serial

PA-ACO-OFDM	Pilot aided ACO-OFDM
PAM	Pulse amplitude modulation
PAM-DMT	pulse-amplitude-modulated discrete multitone modulation
PAPR	peak to average power ratio
PCs	Pilot chips
PD	Photo detector
PIN	Positive-intrinsic-negative
PLC	Power line communication
PoE	Power-over-Ethernet
PoSs	Positive samples
PTS	Partial transmit sequence
QAM	Quadrature amplitude modulation
QoS	Qualities of service
RCPSF	Raised cosine pulse shaping filter
RF	Radio frequency
RGB	Red-Green-Blue
RGB LEDs	READ GREEN BLUE LED
RM	Repeating mapping
RMS	Root mean square
Rx	Receiver
RZ	Return to zero
S/P	Serial to parallel
SC-FDMA	Single carrier-frequency division multiple access
SCG	Subcarrier conjugate
SCM	Single carrier modulation
SER	Symbol error rate
SINR	Signal to interference plus noise
SLM	Selective mapping
SNR	Signal to noise ratio
SSL	Solid state lighting
TDM	Time division multiplexing
TI	Tone Injection
TR	Tone reservation
Tx	Transmitter
U-PAM-FDM	Unipolar pulse amplitude modulation frequency division Multiplexing

VLC	Visible light communication
VPPM	Variable pulse-position modulation
WDD	Wavelength division duplexing
WDM	Wavelength division multiplex
Wi-Fi	Wireless Fidelity
WLAN	Wireless local area network
WLED	White LED
WMAN	Wireless metropolitan area networks
WP LED	White phosphor LED
ZF	Zero forcing

Glossary of Symbols

a_i	The ith path attenuation
δ_x	The chronicle delta
τ_i	The delay of the ith path
τ_{max}	The delay spread of the channel
σ_τ	The root mean square value of the delay spread delay spread
$\overline{\tau^2}$	The first central moment of the power delay profile
p_i	The power at the ith path.
B_C	The frequency correlation function
T_S	The symbol period of the transmitted signal
B_S	The bandwidth of the transmitted signal
$N_{ISI-SCM}$	The number of ISI for SCM scheme
N_c	The number of subcarriers
Δf	Subcarrier spacing
N	The number of OFDM samples
T_{cp}	The duration of CP
N_p	The number of pilots
T_P	The transmitted pilot
T_D	The transmitted data
H_k	The kth transfer function of the channel at the frequency domain
R_P	The received pilots
H_P	The transfer function of pilot
$\hat{s}$	The estimated signal
W^H	The complex matrix optimized under the MMSE criterion
r	The received signal
W^{opt}	The equaliser matrix
σ_s^2	The noise power variance
σ_s^2	The normalized signal power variance
H	The equivalent channel matrix
H^H	The complex channel matrix
de	The distance between Tx and Rx
$R_{sc}(d)$	The energy of the received signal

$\theta(m)$	The correlation term
$\varphi(m)$	The energy term
$\hat{\epsilon}$	The frequency offset
ρ	The magnitude of a correlation coefficient
$\angle$	The argument of a complex number
H	The power amplifier efficiency
Δf_c	The frequency offset
lm/W	Luminous per watt
$P(\omega)$	The LED output optical power at a frequency ω
P_0	The DC power
τ_v	The minority carrier lifetime
mW	Mille watts
Mm	Micro watts
Lx	lux
A/W	Ampere per watt
nm	Nanometre
nA	Nano ampere
pF	Pico farad
ns	Nano second
σ_S^2	The shot noise
σ_T^2	The thermal noise
B_f	The bandwidth of the filter following the photodetector
q	The charge of an electron
I_d	The dark current
T_e	The equivalent temperature
Gb/s	Giga bits per second
σ	The standard deviation, and the mean
σ^2	The variance
μ	The mean
A_d	The confidence interval
A_p	The amplitude of PC
α , β	coefficients are related to the noise power
N_{PA}	The number of PCs inserted prior to the inversion process
α_{OP} , β_{OP}	The optimal values of α and β

N_{PE}	The total number of samples
σ_{ACO}	Standard deviations of the time domain signal for DCO-FDM
σ_{PE-ACO}	Standard deviation of the time domain signal for PE-ACO-FDM
R	The responsivity of the PD
$*$	The linear convolution
$r_k(t)$	The waveform of RCPSF at the kth subcarrier
$\max |x_n|^2$	the peak power of $x(t)$,
$E\{|x(t)|^2\}$	The average power of $x(t)$
p_{error}	The average error vector power
p_{ref}	The average ideal reference vector power
P_{day}	The dynamic range of the LED
P_{max}	The maximum transmitted average power
d_{max}	The maximum achievable distance between the Tx and Rx
P_{opt}	The optimum average power
B_{DC}	The DC-bias
ξ	The proportionality constant
$T_s(\psi)$	The optical filter gain
$g(\psi)$	The optical concentrator gain
Ψ	The irradiance angle

CHAPTER 1

INTRODUCTION

1.1 Background

In recent years, the demand for very high speed mobile connection has been significantly increasing, as broadband communication services are still of great importance. The need to communicate anywhere at any time has pushed the research and development towards further enhancing existing infrastructures, and evolving future technologies that will meet the requirements of next generation communication networks (i.e., 5th generation - 5G). As the number of wireless devices such as smartphones increases (reaching 50% of global devices by 2020), more data traffic capacity will be utilized for multimedia applications. For instance, video content is expected to be 75% of the world's mobile data traffic by 2020. Moreover, mobile data traffic is expected to grow exponentially and increased by 53% by 2020 as compared to 2015, resulting in 30.6 exabytes transferred through mobile networks every month. The data traffic of mobile services will be approximately doubled, thus creating what is known as the mobile spectrum crunch [1, 2]. Therefore, 5G networks, expected to be deployed by 2020, must address a series of critical challenges induced from the increasing mobile data demand, such as optimal spectrum allocation, power consumption and low cost, to name but a few [3]. 5G will be based on the cellular architecture, and will consist of microcells and femtocells to support sufficient user mobility [4].

Optical wireless communications (OWC) is a technology that has been gaining increased attention in the last few decades as a promising solution to fulfil the increased demand for

capacity. Due to its features, high speed data infrastructures can be based on OWC for both indoor and outdoor applications. OWC systems offer cost-effective and highly secured communications in the license-free wavelengths within a practically unlimited bandwidth, thus uncovering several advantages over the radio frequency technologies that utilize the limited, licensed and regulated part of the electromagnetic spectrum (between 30 kHz and 300 GHz). Thus, OWC systems are supposed to meet the requirements for future communications networks for a range of applications, such as voice and data transmission, video and entertainment, disaster recovery, and surveillance [5]. Nevertheless, radio frequency (RF) based wireless technologies offer mobility, which is a much-desired feature in today's mobile communications. However, if a high data rate (R_b), is a requirement at the cost of mobility, OWCs can then represent a good choice, as RF and optical wireless technologies can be considered as complementary techniques, rather than rivals [6]

Visible light communication (VLC), which is mostly used in indoor environment for now, refers to a communication technology that is utilized for the role of illumination, data transmission, and localization, within the visible wavelength range of 380 to 700 nm [6, 7]. Compared to traditional light sources, such as fluorescent lamps and incandescent bulbs, light emitting diodes (LEDs) offer lower power consumption, longer lifetimes, better reliability, and higher brightness, and thus can contribute to a reduction in greenhouse gases. Based on these characteristics, a national programme in Japan has recommended that traditional light sources should be replaced by LEDs [8]. VLCs also offer several advantages over infrared (IR) links, such as, being safe for the human eye and skin, easy-to-install lighting equipment, high power, and lighting distribution, leading to low shadowing areas and offering illumination throughout the room [6].

White LEDs can be implemented in two ways: (*i*) combining three primary colour (RGB) LEDs, or (*ii*) mixing a single blue LED with a yellow phosphor coating (YB), in order to emit a white light. RGB LEDs allow different data to be sent on each device, whereas YB LEDs are simpler and more attractive for general communications [6, 9]. However, the

2

bandwidth of both types of white LEDs is typically only a few MHz, due to their slow time constant [6, 10, 11]. A blue filter is commonly employed to filter the slow yellow components at the receiver. In addition, a driving circuitry equalization is also utilised, pushing the achieved modulation bandwidth to around 20 MHz. However, the disadvantages of the two aforementioned solutions is that they reduce the signal power, which results in an extremely low signal-to-noise ratio (SNR) [10, 12]. Presently, an increasing number of researchers have put their focus and attention on spectrally efficient modulation formats such as orthogonal frequency division multiplexing (OFDM) because it is believed to resolve the issue of bandwidth limitations of VLC systems [11, 13].

OFDM is known to have the capability of producing a very strong solution that could minimize the inter-symbol interference (ISI) in band-limited systems. Because the data transmission in OFDM is in parallel, the OFDM symbol period is much longer than the serial data communication with same R_b. Therefore, ISI affects most one symbol which simplifies the equalization process. In addition, the low frequency noise caused by the DC wandering and flickering interference that came from florescent lights was further reduced as a result of un-modulating the first OFDM subcarrier [10, 14-16]. Furthermore, OFDM will be able to improve the unsatisfying performance at frequencies passed the 3 dB modulation bandwidth by making use of its bit- and power-loading feature [10, 14]. In general, OFDM is described as a sturdy modulation scheme that is able to handle high R_b occurring in VLC systems; for example, a 3 Gb/s VLC system reported in [16].

1.2 Problem statement

In VLC systems, intensity modulation (IM) is the most popular modulation scheme, where the electrical signals are intensity modulated by the LEDs, which require a real and positive signal. The IFFT property of OFDM is exploited in order to convert the OFDM signal to a real one, at a cost of halving the available electrical bandwidth. This is achieved by imposing Hermitian Symmetry (HS) to the data symbols before the IFFT implementation.

In VLC systems, a DC bias is usually added to the bipolar signals to make them positive. In OFDM, such a scheme is referred to as DC-bias optical OFDM (DCO-OFDM) [17]. However, adding a DC-bias to a large peak to average power ratio (PAPR) signal, such as an OFDM signal, and passing it though the limited LED linear dynamic range, makes this schemes undesirable in some VLC applications where power efficiency is a crucial requirement [14, 17, 18].

Alternatively, the IFFT property can be exploited to make the OFDM signal a unipolar signal without needing to DC-bias [19, 20]. This comes at the cost of halving the spectral efficiency in comparison to the DCO-OFDM scheme, and is achieved in [19] by only demodulating the odd subcarriers, resulting in a scheme that is referred to as asymmetrically clipped optical OFDM (ACO-OFDM). Alternatively, in [20], only the imaginary parts of the symbols are demodulated, giving rise to a scheme known as the pulse-amplitude-modulated discrete multi-tone modulation (PAM-DMT) scheme. However, despite their lower spectral efficiency compared to DCO-OFDM, the two aforementioned schemes (i.e. ACO-OFDM and PAM-DMT schemes) still possess a high PAPR compared to single carrier modulation (SCM) [10, 21, 22]

Recently, a low PAPR modified RF OFDM scheme, known as the interleaved frequency division multiple access (IFDMA) scheme, has been adapted to be suitable for IM and direct detection (IM/DD) based VLC systems [23-25]. However, because of the IM/DD requirements in VLC systems, all IFDMA schemes are exposed to HS, which makes the PAPR of these schemes higher in comparison to the RF IFDMA schemes [26, 27].

1.3 Aims and Objectives

In VLC systems based IM, the transmitted signal is modulated regarding to its intensity. Therefore, the bipolar and the complex signal such as OFDM should be adapted to be presented as a real and positive value signals prior to passing it to the LED.

These modifications comes either at the cost of power consumption as in DCO-OFDM, or at the cost of the spectral efficiency as in ACO-OFDM (see subsection 1.2). Therefore, the first aim is to propose an optimal model that presents trade-off between ACO-OFDM's low spectral efficiency and DCO-OFDM's low power efficiency.

Furthermore, the limited range of LED impose a critical challenge for the OFDM signal utilisation in VLCs, since the OFDM has high PAPR. Thus, the other aim is to enhance the OFDM PAPR in VLC systems. The full set of objectives are outlined as follows:

- To analyze how OFDM contributes towards enhancing the performance of indoor visible light communications systems.

- To increase the data rates of the unipolar optical OFDM schemes by proposing a novel unipolar OFDM scheme.

- To carry out full system implementation and obtain measurement results for the system performance indicators (bit error rate (BER), symbol error rate (SER), etc.) of the proposed unipolar OFDM scheme, and compare them with the traditional unipolar OFDM schemes.

- To decrease the PAPR of the OFDM signal in IM/DD based VLC systems, and subsequently improve its transmitted power as well as increase the distance between the transmitter (Tx) and the receiver (Rx), by proposing another novel OFDM scheme.

- To theoretically and mathematically identify how the proposed scheme has a lower PAPR compared to other optical OFDM schemes as well as to compare the PAPR and BER of the proposed scheme with other optical OFDM schemes using a MATLAB program.

- To experimentally demonstrate how the proposed scheme outperforms the traditional OFDM schemes in terms of average transmitted power and Tx-Rx distance.

- To provide recommendations for indoor VLC system applications in light of our OFDM study finding.

5

1.4 Original Contributions

The key contributions to knowledge that have been achieved in this thesis can be summarised as follows:

The asymmetrical time domain characteristics of ACO-OFDM signal are investigated in Chapter 4 to increase R_b by up to 33%. This is achieved by reducing the ACO-OFDM time symbol duration, where the second half of the symbol is removed and only the first half is maintained. To meet requirements of IM/DD, the negative samples of the first half of the ACO-OFDM symbol are inverted to positive. However, to enable the receiver to detect the inverted samples and subsequently convert them back to negative samples, two schemes are introduced to fulfil this purpose, known as the pilot aided ACO-OFDM (PA-ACO-OFDM) scheme [J1] and, the position encoded ACO-OFDM (PE-ACO-OFDM) scheme [J2].

- In PA-ACO-OFDM, the receiver inversion detection is achieved by inserting several high amplitude pilots at the PA-ACO-OFDM Tx prior to the negative inversion process. However, although the insertion of higher amplitude pilots in PA-ACO-OFDM can be utilized for illumination, localization, and synchronization purposes, the limited linear range of LEDs makes this scheme only desirable when a low SNR is required.

- In PE-ACO-OFDM, the positions of the negative and positive samples are encoded using a QAM constellation order, to enable the receiver to detect and convert the inverted samples. However, R_b of PE-ACO-OFDM increases by increasing the encoded QAM constellation order, which mean this scheme is only applicable for high SNR environment.

Remarkably, the reduction of ACO-OFDM time domain symbol duration in both proposed schemes does not cause any ISI, as their symbol duration is still higher than the indoor VLC delay spread duration even after being reduced. Furthermore, in general,

increasing and decreasing the OFDM symbol duration can be achieved by increasing or decreasing the number of sub-carriers, respectively.

❖ In IFDMA, FFT and interleaving mapping blocks are added to the OFDM Tx, to make the PAPR of the signal as low as that of SCM. However, this scheme is mainly proposed to improve the OFDM PAPR in RF systems. In this work, the IFDMA scheme is adapted for IM/DD based VLC systems using three different methods, thus resulting in three new optical OFDM schemes known as, the unipolar pulse amplitude modulation frequency division multiplexing (U-PAM-FDM) scheme, the bipolar pulse amplitude modulation frequency division multiplexing (B-PAM-FDM) scheme, and the optical interleaved frequency division multiplexing (OIFDM) scheme.

▪ In U-PAM-FDM (see Chapter 5), the input data symbols of the FFT block at the IFDMA Tx are made real (i.e. PAM), which makes the output subcarriers of the FFT block symmetrically conjugated, except the first and middle ones. Two new subcarriers are added to the output of the FFT block at the U-PAM-FDM Tx to make all the subcarriers symmetrically conjugated, before being fed to the interleaving mapping and IFFT blocks, thus making the time domain samples of U-PAM-FDM real asymmetrical samples suitable for IM/DD. This process is achieved by what is referred to in this work as the subcarrier conjugate (SCG) block. However, although the PAPR of this scheme is lower than the PAPRs of the traditional unipolar OFDM schemes, it is still higher than the PAPR of the RF IFDMA scheme. This is because the insertion of the SCG block in U-PAM-FDM means only some subcarriers enjoy the interleaving mapping features.

▪ In B-PAM-FDM (Chapter 6, section 6.2), IFDMA is adapted for IM/DD without the inclusion of the SCG block, which makes the PAPR of B-PAM-FDM as low as that of IFDMA. The only difference between B-PAM-FDM and IFDMA, is that the interleaving mapping block at the IFDMA Tx is replaced by the repeating mapping (RM) block. In RM block, the output FFT subcarriers vector is repeated twice before

7

being fed to the IFFT block, thus making the odd IFFT samples the same as the data symbol, while making the odd samples zeros. Therefore, letting the data symbols be real symbols (i.e. PAM) results in real time domain samples suitable for IM/DD. Note that since the imaginary parts of B-PAM-FDM data symbols are not modulated, and due to the presence of the RM block, the spectral efficiency of B-PAMP-FDM is a half that of DCO-OFDM (i.e. the same as the spectral efficiency of ACO-OFDM and PAM-DMT). However, since the odd samples of B-PAM-FDM do not carry any data, another B-PAM-FDM symbol can be transmitted by theses samples using the time division multiplexing (TDM) technique. In addition, the odd samples can be utilized for other VLC applications besides data transmission, such as illumination, positioning and localization applications. Furthermore, due to the presence of the RM block, any affected subcarrier in the frequency domain can be easily compensated. Finally, because of the low PAPR of B-PAM-FDM, the impact of the DC-bias on the system performance is reduced (the simulation and experimental results of B-PAM-FDM are presented in subsection 6.2.2).

▪ In OIFDM, the symmetrical characteristics of the IFDMA time domain signal are exploited in order to introduce a new OFDM scheme suitable for IM/DD based VLC systems, with as high a spectral efficiency as that of the DCO-OFDM scheme, and as low a PAPR as that of the IFDMA scheme. This is accomplished by setting the interleaving mapping factor (Q) at the frequency domain to 2, and subsequently repeating the time domain samples of IFDMA twice through each IFDMA time domain symbol. Unlike all previous OFDM schemes, the first OIFDM subcarrier is modulated, and can therefore be affected by the DC-bias and the ambient noise. As such, after the IFFT implementation, all time domain samples can be affected by the aforementioned noise sources. However, in this research work, a new simple algorithm is proposed to remove the impact of these noise sources, at the cost of increasing the required SNR compared to the traditional DCO-OFDM scheme.

The research road map is illustrated in Figure 1.1, where the uncoloured blocks indicate the contributions of this work.
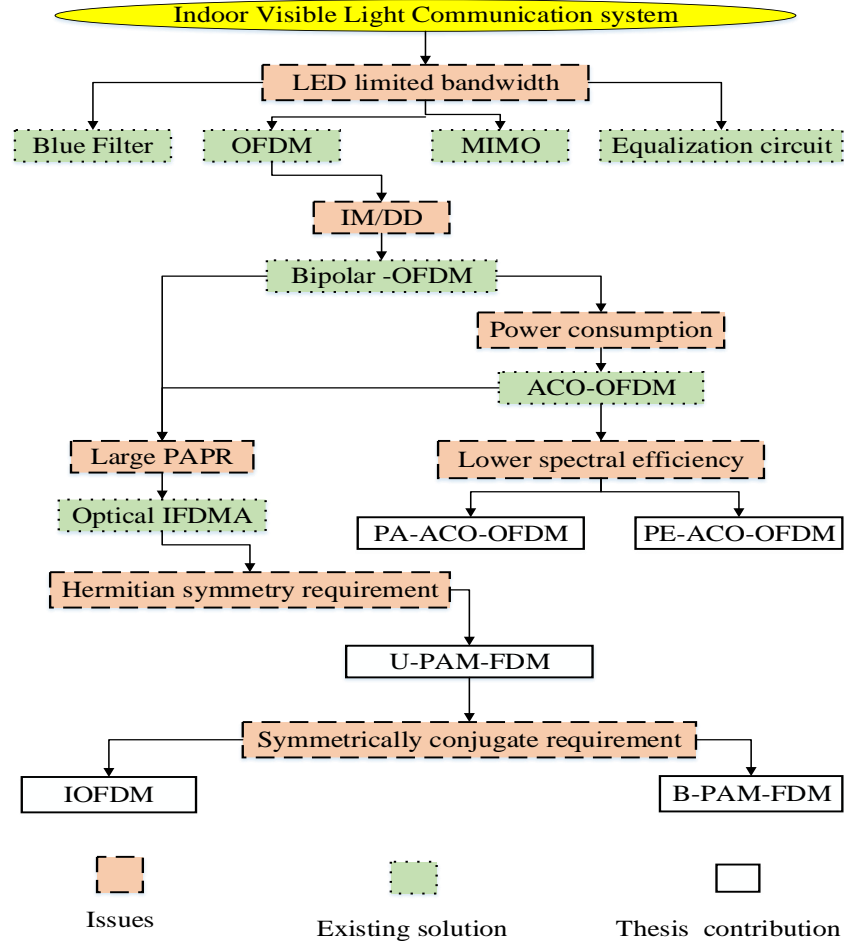
Figure 1.1. Summary of thesis contributions

1.5 List of publications

The outcomes of this research have either been published in conferences or peer-reviewed in journal papers.

Journals

[J1] **O. Saied**, Z. Ghassemlooy, X. Dai, H. Le Minh, W. O. Popoola, S.-K. Liaw, and M. Zhang, "Pilot-aided asymmetrically clipped optical OFDM in visible light communication [J]," *The Mediterranean Journal of Electronics and Communications,* vol. 12, pp. 64-71, 2016.

[J2]   **O. Saied**, Z. Ghassemlooy, X. Tang, X. Dai, H. Le Minh, and B. Lin, "Position encoded asymmetrically clipped optical orthogonal frequency division multiplexing in visible light communications," *Journal of Communications and Information Networks,* vol. 2, pp. 1-10, 2017.

   Conferences

[C1]   **O. Saied**, Z. Ghassemlooy, R. C. Kizilirmak, X. Dai, C. Ribeiro, M. Zhang, and S. Rajbhandari, "Single carrier optical FDM in visible light communication," in *Communication Systems, Networks and Digital Signal Processing (CSNDSP), 2016 10th International Symposium on*, 2016, pp. 1-5.

1.6 Thesis Outline

This thesis is structured as follows. The theoretical concepts behind the OFDM scheme are presented in Chapter 2. In Chapter 3, a brief review of the theory of VLC systems, including the challenges behind the implementation of an OFDM scheme in IM/DD based VLC systems, is provided.

Chapter 4 presents the proposed PA-ACO-OFDM and PE-ACO-OFDM schemes as a means to increase the ACO-OFDM data rates, where the simulation results demonstrate that the R_b of ACO-OFDM are increased by 33% when these schemes are considered.

 In Chapter 5, the U-PAM-FDM scheme is introduced to improve the PAPR of the unipolar OFDM schemes in IM/DD based VLC systems, where the simulation results show that the PAPR of the proposed scheme is 3.8 dB lower than the PAPR of the ACO-OFDM scheme. Furthermore, the experimental results of this chapter demonstrate that the proposed scheme provides 2 dBm more transmitted power compared to the traditional ACO-OFDM scheme.

In Chapter 6, the B-PAM-FDM scheme is introduced in Section 6.2 as a means to reduce the PAPR of bipolar OFDM schemes, where the simulation results show that the PAPR of B-PAM-FDM is 7 dB lower than that of DCO-OFDM. Furthermore, this reduction in the PAPR is experimentally investigated in this chapter, where results demonstrate that the distance between the Tx and Rx is increased by 44% compared to DCO-OFDM. In addition, the IOFDM scheme is presented in Section 6.3 to achieve the same goals, where the simulation results show that the PAPR of OIFDM is lower by 10 dB in comparison to DCO-OFDM.

Finally, a summary of this thesis is presented in Chapter 7, along with the conclusions drawn from the findings of this research work.

CHAPTER 2

ORTHOGONAL FREQUENCY DIVISION MULTIPLEXING

2.1 Introduction

The basic concept behind OFDM modulation scheme will be introduced in this chapter as it is the foundation of this research work.

OFDM is an attractive multi-carrier modulation (MCM) scheme that can deal with multipath propagation challenges such as ISI and offer higher R_b with no need to deploy a complex equaliser at the Rx [28-30]. OFDM has been widely used as a modulation and a multiplexing technology in a number of RF applications such as digital television (DTV), digital audio broadcasting (DAB), digital subscriber line (DSL) and in standards for wireless local area network (WLANs), wireless metropolitan area networks (WMANs) and long term evaluation (LTE) 4th generation mobile communication networks [31-33]. Recently, OFDM has also attracted significant research attention for its use in OWC including VLC [34-38]. This chapter is divided into two main sections: section 2.2 gives a brief introduction about wireless multipath propagation challenges and how OFDM deals with such challenges. The basic principle of OFDM including the orthogonality of the scheme, OFDM modulation principles, cyclic prefix (CP), OFDM channel estimation and the peak average power ratio of an OFDM signal are discussed in detail in section 2.3.

2.2 Wireless Multipath Propagation

In wireless communications the signal may reach the Rx via a number of paths (L-path), i.e., the line of sight (LOS) and non-LOS (NLOS) as shown in Figure 2.1. The sources of multipath propagation are atmospheric ducting, ionospheric reflection and refraction. One major cause of this phenomenon is reflection from water bodies and terrestrial objects like mountains and buildings[15, 39].
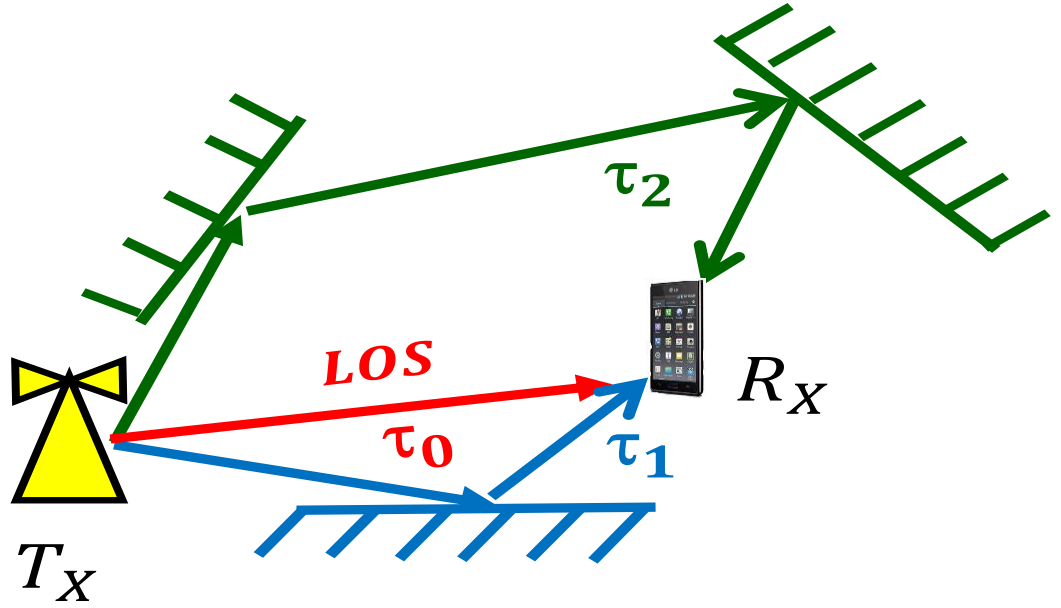
Figure 2.1. Multi path propagation in a wireless channel

As a result, the channel impulse response $\tilde{h}_t$ is given as [15]:

$$\tilde{h}_{(\tau,\ t)} = \sum_{i=0}^{L-1} a_i(t)\, \delta_{(t-\tau_i)} \tag{2.1 (a)}$$

where, a_i is the ith path attenuation, δ_x is the chronicle delta, which is equal to one only when $x = 0$ and is zero otherwise, and τ_i is the delay of the ith path. The Equation (2.1 (a)) illustrates the impulse response of the outdoor channel varies with time (t), whereas the indoor channel is a static channel and its impulse response is defined as follows:

$$\tilde{h}_{(t)} = \sum_{i=0}^{L-1} a_i \, \delta_{(t-\tau_i)} \qquad \text{(2.1 (b))}$$

However, receiving the same transmitted symbol with different amplitudes and phases at different times leads to ISI at the Rx [15, 40]. The amount of ISI depends on the type of channel fading, which in turn depends on parameters such as the delay spread and the coherence bandwidth. These will be further elaborated upon in the next subsections.

2.2.1 The delay spread

The delay spread of the channel (τ_{max}) is defined as the duration between the received signal from the LOS path and the received signal from the longest NLOS path. However, only some of the reflected received signals are important to consider since they have higher amount of power, which can affect the system performance. Other NLOS paths lead to received signals that can be considered ineffective with negligible amount of power [31]. Therefore, the root mean square (rms) value of the delay spread (σ_τ) is often used instead of τ_{max}, which is given as [15]:

$$\sigma_\tau = \sqrt{\overline{\tau^2} - (\overline{\tau})^2}, \qquad (2.2)$$

where $\overline{\tau^2}$ is the first central moment of the power delay profile defined as:

$$\overline{\tau^2} = \frac{\sum_i \tau_i \, p_i}{\sum_i p_i}, \qquad (2.3)$$

and $\overline{\tau}$ is the second central moment of the power delay profile, which is given by:

$$(\overline{\tau})^2 = \frac{\sum_i \tau_i^2 \, p_i}{\sum_i p_i}, \qquad (2.4)$$

Note that, p_i is the power at the ith path.

2.2.2 The coherence bandwidth

The coherence bandwidth (B_C) is the fraction of the channel bandwidth where the frequency components have a strong correlation and as a result the spectral components pass through this bandwidth with almost the same gain and linear phase. In general B_C is defined as [15]:

$$B_C \approx \frac{1}{\sigma_\tau}. \tag{2.5}$$

However, if the frequency correlation function of B_C is ≥ 0.5, then (2.5) will be as in [15]:

$$B_C \approx \frac{1}{5\sigma_\tau}. \tag{2.6}$$

2.2.3 Flat fading and frequency selective fading

Fading is the variations of the amplitude, phases, and/or multipath delays of a signal through the duration of time or a transmission span. Wireless channels introduce different types of fading, which have different effects, and occur due to different reasons. Table 2.1 illustrates the various types of fading present in a wireless channel [15, 40-42].

Table 2.1 Comparison between wireless channel fading [15]

Fading Type	Fading Reason	Fading Effects
Path loss	Long distance between the Tx and the Rx	Transmitted power drops in proportion to the square of the distance between Tx and Rx
Shadowing	Objects among the Tx and the Rx paths	Transmitted signal may lose some part of power due to absorption, reflection, scattering, and diffraction
Time variance	Movement of the Tx, Rx or the surrounding objects	Spread in the frequency domain, (Doppler shift)
Multipath	Multipath propagation	ISI

Multipath fading is one of the most detrimental and can degrade system performance significantly. This fading is a result of multipath propagation where the signal takes different

reflecting and refracting paths before arriving at the Rx. The amplitude and the phase of the signal change after each reflection and refraction, and as a result different signals with different amplitudes and phases are received either at different times or at the same time, thus giving rise to ISI [15, 42].

Multipath fading has been extensively studied and is generally classified into two types:

a) **Flat fading:** is the most common and simplest type of multipath fading. In flat fading, the multipath arrangement of the channel is held in a way that the spectral properties of the modulated signal are preserved at the Rx end. However, the power of the received signal fluctuates over time due to the changes in the channel gain that occur as a result of multipath propagation. Flat fading results whenever the bandwidth of the transmitted signal (B_S) is less than B_C. In other words, when the symbol period of the transmitted signal (T_S) is greater than σ_τ. Therefore, the transmitted signal is subject to flat fading if $B_S \ll B_C$ and $T_S \gg \sigma_\tau$.

The flat fading's characteristics are shown in Figure 2.2. The figure clearly illustrates how the amplitude of the transmitted signal varies over a time interval according to the changes in the channel gain, while the signal spectrum remains unchanged [42].
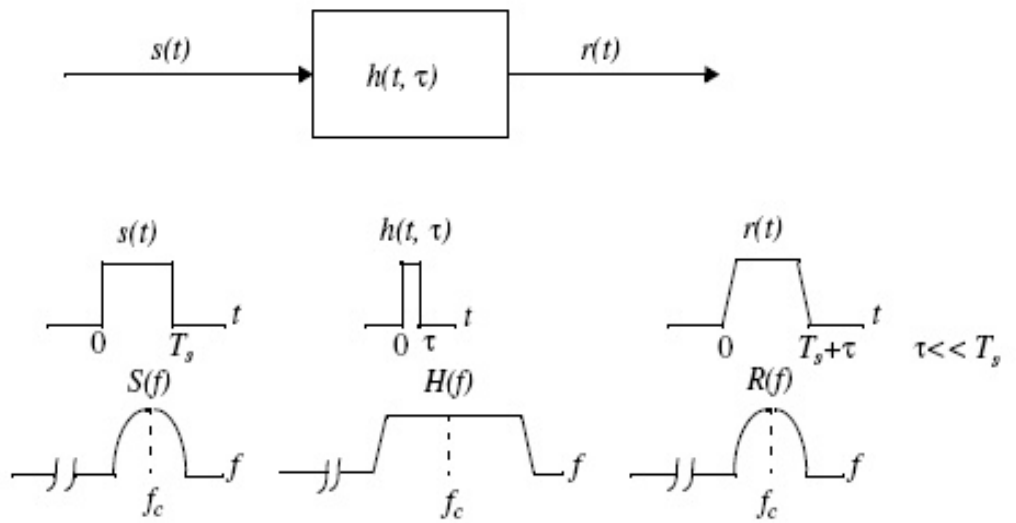
Figure 2.2. Characteristics of flat fading channel due to multipath propagation [42]

16

b) **Frequency selective fading:** occurs due to time dispersion of the transmitted signals while propagating through the channel. Considering the frequency domain, some frequency components in the received signal spectrum possess higher gains relative to others. Frequency selective fading occurs when $B_s \gg B_C$ and $T_s \ll \sigma_\tau$. As such, we receive different version of the transmitted signal at the receiving end. All these signals experience time difference and as such the channel experiences ISI. However, a common rule of thumb is that the channel is a selective fading channel when [15]:

$$\frac{T_s}{\sigma_\tau} < 10 .$$

(2.7)

The frequency selective fading characteristics are illustrated in Figure 2.3.
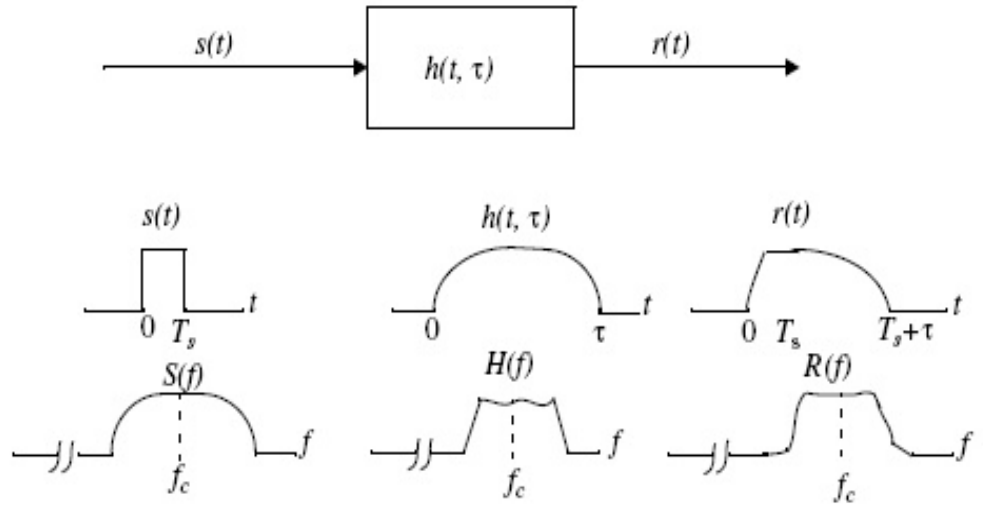
Figure 2.3. Characteristics of selective fading channel due to multipath propagation [42]

2.2.4 ISI mitigation

ISI is one of the most prominent multipath distortions that affects the system performance significantly. The number of interfering symbols for the SCM scheme is defined as [31]:

(2.8)

$$N_{ISI-SCM} = \frac{\tau_{max}}{T_s} .$$

From Equation 2.8, the straightforward solution to mitigate ISI is to make the symbol duration of the transmitted signal less than or equal to the maximum delay spread of the channel. However, an increase of T_s means a decrease in data rates as [43]:

$$R_b = \frac{log_2(M)}{T_s},$$ (2.9)

where, M is the constellation order. For example, if T_{max} is 3.7 µs (as in an outdoor pedestrian channel) [43], then by making $T_s = \tau_{max}$, R_b will be only 1.08 Mbps for 16-QAM.

Another prominent technique that can deal with ISI is equalization. This technique uses a filter with an impulse response equal to the inverse impulse response of the channel. However, equalization may not be practical in high data rate systems, as such systems require more complex equalizers [10, 15, 43]. A better solution was first utilised by military HF radio links in 1950s and is known as multicarrier modulation (MCM) scheme [44]. In this scheme, the available signal bandwidth is divided to a number of narrow bandwidth slots (subcarriers) where the bandwidth of each subcarrier is less than coherence bandwidth. In other words, the symbol duration of each subcarrier is greater than the delay spread of the channel. The number of interfering symbols for the MCM scheme is defined as [31]:

$$N_{ISI-MCM} = \frac{T_{max}}{N_c T_s},$$ (2.10)

where N_c is the number of subcarriers. The carriers in a multicarrier transmission system carry data symbols based on the modulation technique used. OFDM is the best example of a multicarrier transmission system that can mitigate ISI and support higher data rates.

2.3 Orthogonal Frequency Division Multiplexing (OFDM)

OFDM was first proposed by Chang in 1966 as a special MCM scheme [45] that expands the principle of single carrier transmission technique by employing more than one carrier in the same single channel, and in which the bandwidth of each carrier is less than the coherence bandwidth of the channel. In another words, instead of transmitting a high data rate using a

18

single subcarrier, OFDM employs multiple closely spaced orthogonal subcarriers transmitted in parallel using the IFFT algorithm. Every subcarrier is transmitted using a traditional digital modulation technique such as QPSK or 16 QAM at a low symbol rate [46]. OFDM is based on the principles of the popular frequency division multiplexing (FDM) technique, which uses different streams of data mapped into different parallel frequency channels. To avoid inter channel interference (ICI); a guard band is inserted between each adjacent two channels. However, in OFDM all the channels (subcarriers) are orthogonal to each other, i.e., when one subcarrier is at its peak, all other subcarriers should be at zero. Therefore, OFDM is much more bandwidth efficient compared to a standard FDM scheme [15], as Figure 2.4 illustrate the frequency domain of an OFDM and FDM.
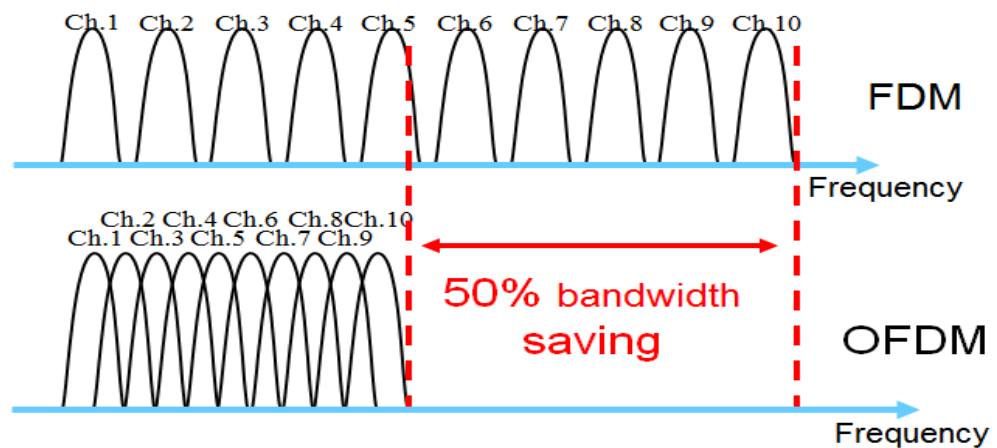
Figure 2.4. Spectrums of FDM and OFDM systems.

Different symbols in the frequency domain are used among adjacent subcarriers that have been independently transmitted with a complex data. The IFFT is performed on frequency domain subcarriers to obtain the OFDM symbol in the time domain. In the time domain, the guard intervals between every symbol are used so that ISI, occurring due to the multi-path delay spread in the radio channel, can be overcome at the Rx. Different symbols are joined to produce the OFDM signal. A FFT is then performed on the OFDM symbols at the Rx end so that the original data bits can be reconstructed [40].

2.3.1 Orthogonality of OFDM subcarriers

The signals are orthogonal if they are uncorrelated to each other. Orthogonality in OFDM is achieved by making the space between each adjacent two subcarriers (subcarrier spacing (Δf)) equal to the inverse of the OFDM symbol duration (T_s), which can be easily obtained at the Tx through the implementation of IFFT. This ensures that all other OFDM subcarriers are at zero value if one subcarrier is at its peak value (overlapping with no ICI (see Figure 2.5) and as a result the transmitted subcarriers can be easily detected and reconstructed at the Rx through the implementation of FFT [47].
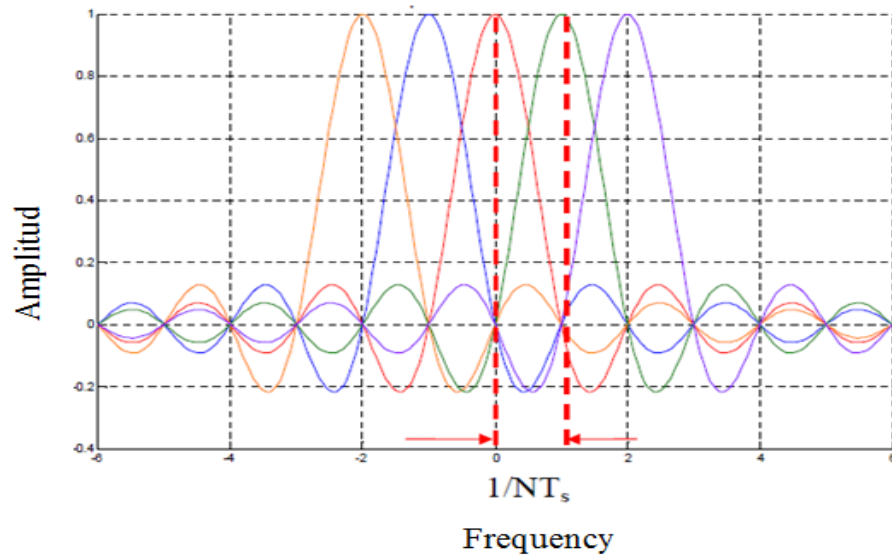
Figure 2.5. Frequency spectrum of OFDM with five subcarriers [47]

The representation of OFDM with three subcarriers in the time domain is illustrated in Figure 2.6. As it can be clearly seen, each subcarrier in the frequency domain is represented by an integer number of cycles at the time domain [48].
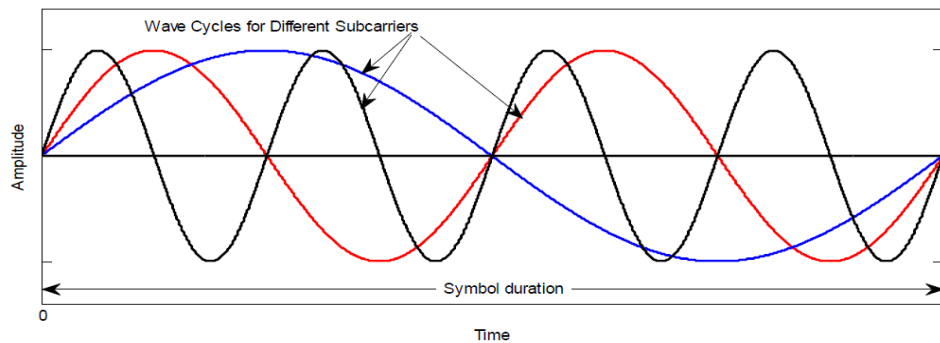
Figure 2.6. Time domain representation of OFDM with three subcarriers [48]

20

Mathematically, OFDM subcarriers are orthogonal to each other if the integration of the products is zero. Considering an OFDM signal $\{e^{j2\Pi\Delta f_k t}\}_{k=0}^{N-1}$ where $0 \le t \le T_s$ and Δf_k is the frequency of the kth subcarrier, then [15]:

$$\frac{1}{T_s}\int_0^{T_s} e^{j2\pi\Delta f_k t} e^{-j2\pi\Delta f_i t} dt = \frac{1}{T_s}\int_0^{T_s} e^{j2\pi\frac{k}{T_s}t} e^{-j2\pi\frac{i}{T_s}t} dt.$$

$$= \frac{1}{T_s}\int_0^{T_s} e^{j2\pi\frac{(k-i)}{T_s}t} dt. \qquad (2.11)$$

$$= \begin{cases} 1, & \forall \; integer \; k = i \\ 0, & otherwise \end{cases}.$$

2.3.2 OFDM modulation

As illustrated in Figure 2.7, OFDM modulation is based on the concept of changing a serial symbol flow to a parallel one, with every symbol flow from the parallel set modulating a different carrier. The space between the carriers is $\frac{1}{T_S}$. Here T_S denotes the time period of the OFDM symbol. The orthogonality of the carriers ensures that the carriers remain separate without any interference. Adding the orthogonal carriers transmitted by parallel symbol flows is achieved via performing the IFFT of the parallel symbol set. This contrasts with what takes place at the Rx end, where the opposite operation, i.e., FFT, is performed and the parallel symbol streams are changed to serial symbol streams.

(a) OFDM modulation/demodulation

(b) Realization of subcarrier orthogonality
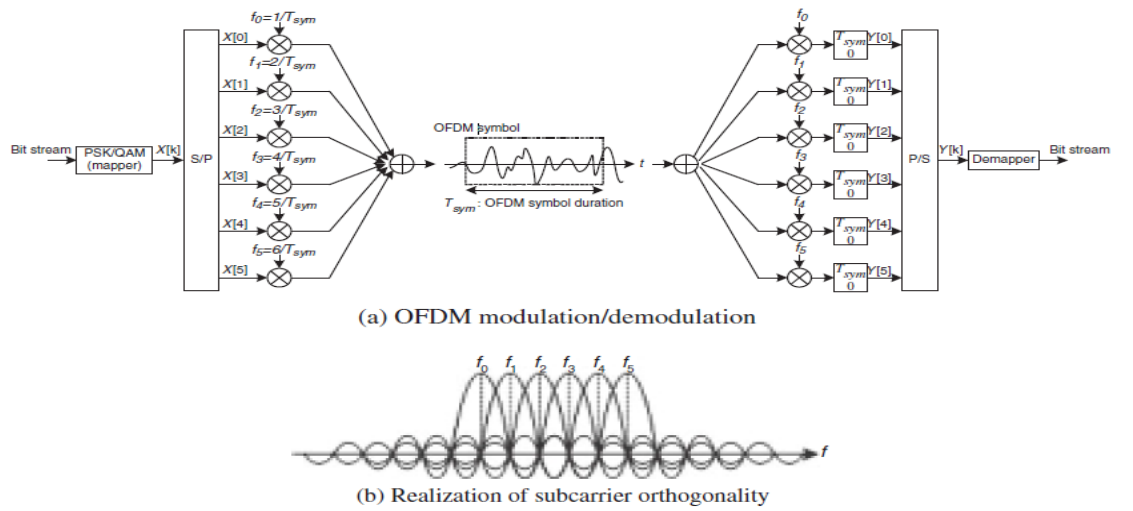
Figure 2.7. An OFDM modulator demodulator with N=6 [15].

21

The basic benefit of this technique, in addition to converting frequency selective channel fading to flat channel fading, is that one carrier might suffer excessive fading while other carriers can still carry the data. Because of FFT and the CP extension, the equalization on OFDM is much simpler than the equalization on wideband channels. ISI harms the signal in the time domain and is tackled through the addition of the CP [30].

2.3.3 Cyclic prefix (CP)

Cyclic prefix was first adopted by A. Peled and A. Ruizin in 1980 [49] to overcome interference between received multipath symbols. The concept of CP is shown in Figure 2.8, where the last fraction of every OFDM symbol is copied and added to the beginning of the symbol. To mitigate ISI, the duration of CP must be equal to or greater than τ_{max}. In addition to mitigating ISI, CP also converts the linear convolution induced by the channel to circular convolution, which is equivalent to multiplication in the frequency domain, and as a result only one tap equalizer is required to remove the effect of the channel [33].
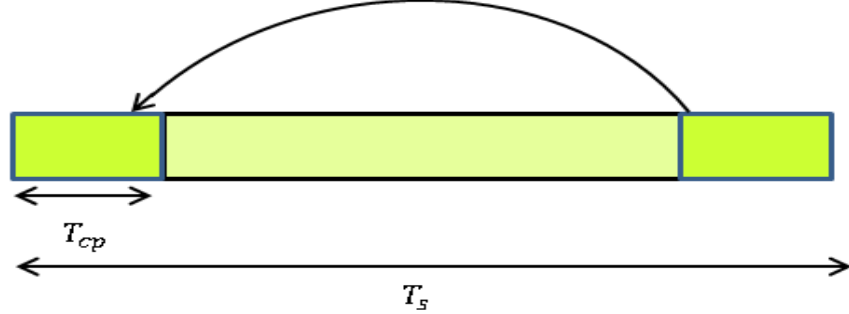
Figure 2.8. OFDM guard band

To clarify this, let x be an OFDM symbol where $x = [x_0, x_1, x_2, \ldots, x_{N-1}]$ and N is the number of OFDM time domain samples.

After parallel to serial conversion, a CP of length D is added to x thus resulting in $\check{x}$ of length $(D + N)$ where $\check{x} = [\check{x}_{N-D}, \check{x}_{N-D+1}, \ldots \check{x}_{N-1}, \check{x}_0, \check{x}_1, \check{x}_2 \ldots, \check{x}_{N-D}, \check{x}_{N-D+1}, \ldots \check{x}_{N-1}]$.

Subsequently, $\check{x}$ is then transmitted through a multipath channel of length L where its impulse response is denoted by $h = [h_0, h_1, \ldots \ldots h_L]$. For the sake of simplicity, we assume that $N = 4$, $D = L - 1 = 2$ and the duration between each successive arrival symbol is E

22

seconds, where E is the OFDM sample duration. Consequently, three version of $\check{x}$ will interfere with each other and with other symbols at the Rx, thus causing ISI (see Figure 2.9). However, as illustrated in Figure 2.9, the interference between other symbols can be easily eliminated by removing the CP, thus obtaining y, where $y = [y_0, y_1, y_2, y_3]$ and is given by:

$$y_0 = h_0 x_0 + h_1 x_3 + h_2 x_2 \tag{2.12}$$

$$y_1 = h_0 x_1 + h_1 x_0 + h_2 x_3 \tag{2.13}$$

$$y_2 = h_0 x_2 + h_1 x_1 + h_2 x_0 \tag{2.14}$$

$$y_3 = h_0 x_3 + h_1 x_2 + h_2 x_1 \tag{2.15}$$

From Equations 2.12, 2.13, 2.14 and 2.15, it can be clearly observed that:

$$y[n] = \sum_{m=0}^{2} h[m] \quad x[(n-m)4]. \tag{2.16}$$

$$y[n] = \sum_{m=0}^{L-1} h[m] \quad x[(n-m)N]. \tag{2.17}$$

Thus,

$$y = h \circledast x. \tag{2.18}$$

where $\circledast$ denotes circular convolution. Figure 2.9 and Equation 2.18 clearly illustrate how the CP removes ISI and converts the linear convolution to circular convolution.
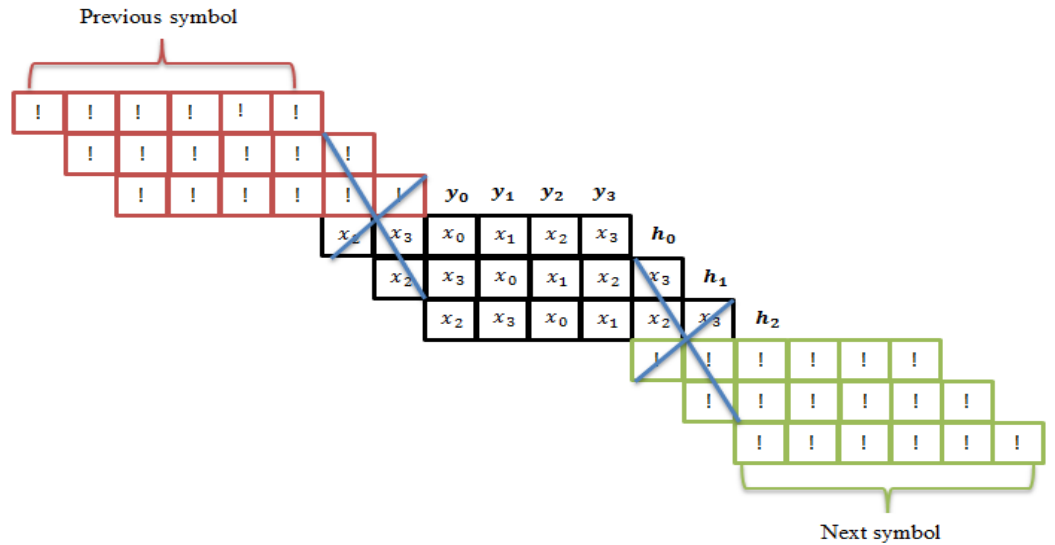
Figure 2.9. Interference between different versions of a symbol and with its adjacent symbols, where L=3, CP=N/2 and N=4

23

However, replacing the last part of an OFDM symbol decreases the data rates as well as the SNR as is illustrated by Equations 2.19 and 2.20, respectively [30, 50]:

$$R_b = \frac{log_2(M)}{T_s + T_{cp}},$$ (2.19)

$$SNR = -10 \log 10 \left(1 - \frac{T_{cp}}{T_s}\right),$$ (2.20)

where T_{cp} is the duration of CP and T_s is the duration of the whole symbol.

2.3.4 OFDM channel estimation

Channel estimation is defined as the procedure of estimating or interpreting the impact of the physical medium on the input data being transmitted. The main advantage of channel estimation is that it grants the Rx the ability to check the impact of the channel on the transmitted signal. Furthermore, channel estimation is also important in eliminating ISI and in noise rejection techniques. Wideband mobile communication systems use a dynamic estimation of the channel prior to the demodulation of the OFDM signals due to the time variation of the channel response and frequency selection. The main channel estimation procedure block diagram is shown in Figure 2.10 [15].
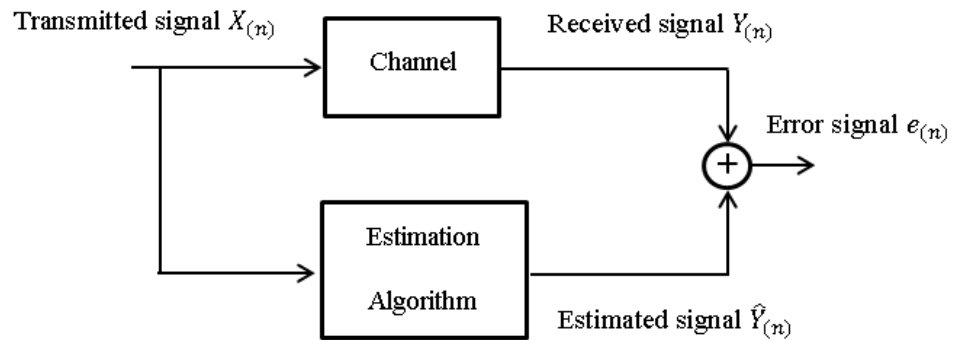
Figure 2.10. Channel estimation procedure [15]

However, OFDM channels can be estimated in the frequency domain by inserting pilot tones. There are two main types that are commonly used for pilot insertion:

a) Comp type is used when the channel rapidly changes even in one OFDM block. It places several pilots uniformly in each OFDM symbol as illustrated in Figure 2.11 (a). At the Rx, only channels that are located in the pilot tones are estimated and the rest are estimated using one of the interpolation techniques (e.g., linear interpolation).

To elaborate, let the input of the IFFT at the Tx is X, where $X = X_0, X_1, X_2, ..., X_{N-1}$, N is the IFFT points and N_p is the number of pilots, which is given by [51]:

$$X_k = \begin{cases} T_P & \text{if } k = G.g \\ T_D, & \text{otherwise}' \end{cases} \qquad (2.21)$$

Where k is the kth OFDM symbol, T_P is the transmitted pilot symbol, T_D is the transmitted data symbol, $G = \dfrac{N}{N_p}$ and $g = (0,1,2, ... N_p - 1)$. At the Rx, the CP is removed and the received signal y_k is converted from the time domain to the frequency domain (Y_k) where $Y_k = X_k. H_k + n$. Here, H_k is the kth frequency response of the channel and n is additive white Gaussian noise (AWGN). The received pilots R_P can then be easily extracted from the received signal Y_k:

$$Y_k = \begin{cases} R_P & \text{if } k = G.g \\ R_D, & \text{otherwise} \end{cases} \qquad (2.22)$$

Subsequently, a least square (LS) algorithm, which is one of the simplest methods for the channel frequency response estimation, can be applied to R_P to estimate the frequency response of the channel located in the pilot tones (H_P) as [52]:

$$H_P = \frac{R_P}{T_P}. \qquad (2.23)$$

Finally, the rest of the channels are estimated using one of the interpolation techniques.

a) Block type is implemented under the assumption of a slow fading and is performed by inserting pilot tones in all OFDM subcarriers as shown in Figure 2.11 (b). The f response of the channel is estimated once and then implemented for the incoming symbols [51].
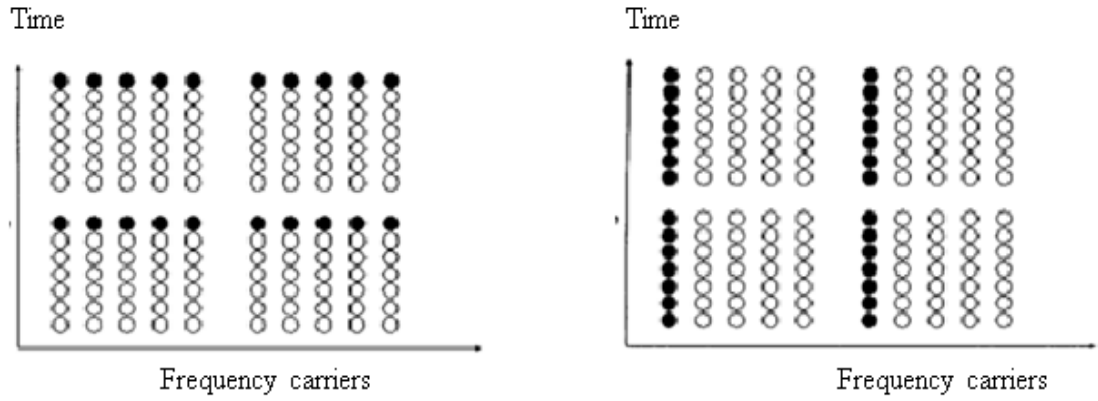
Figure 2.11 (a) comp type pilot   (b) block type pilot [51]

2.3.5 OFDM equalization

ISI has a negative impact on the system performance and can be caused by multipath propagation, a large RMS delay spread and/or a low-pass frequency response of some system components (such as an LED in the case of VLC systems). Additionally, the time variations of the OFDM symbol period in a fading channel have a negative impact on the subcarriers orthogonality as it introduces ICI.

Thus, equalization techniques are employed to compensate for the detrimental ISI and ICI effects and to increase the achievable data rates. In multicarrier systems such as an OFDM, a single-tap equalizer can be utilised since the RMS delay spread is significantly shorter than the symbol duration and the frequency selective channel is transformed into a flat channel fading over the subcarrier bandwidth, which considerably simplifies the equalization process. However, the SNR penalties must be considered when utilising an equalizer. There are several commonly employed equalization techniques such as linear equalization which is based on the zero forcing (ZF) and minimum mean square error (MMSE) algorithms [53, 54], and nonlinear equalization which is based on a decision feedback or on ICI cancellation [55, 56]. Although nonlinear equalizers based on ICI cancellation have been shown to outperform linear filtering, linear equalizers are still used due to their low complexity.

The MMSE equalizer is based on the estimation on the minimal mean square error between the equalized and the transmitted signal. The output of the MMSE equalizer (i.e., the equalized symbols) can be given as [57]:

$$\hat{s} = W^H r, \tag{2.24}$$

where r is the received signal and W^H is the complex matrix optimized under the MMSE criterion and expressed as [57, 58]:

$$W^{opt} = arg \, min \, |s - W^H r|^2, \tag{2.25}$$

where s is the transmitted signal. Then the solution to (2.21) is given by [58, 59]:

$$W^H = \left[H^H H + \frac{\sigma_n^2}{\sigma_s^2} I \right]^{-1} H^H, \tag{2.26}$$

where σ_n^2 and $\sigma_s^2 = 1$ are the noise and normalized signal power variance, respectively, and H is the channel vector. The ZF equalizer restores the received signal by applying the inverse of the channel frequency response. However, such an algorithm is prone to noise in low SNR channels. The output symbols estimated by the ZF algorithm are updated according to (2.24) and the ZF solution is given by [57, 58]:

$$W^H = (H^H H)^{-1} H^H = H^+, \tag{2.27}$$

where $(\cdot)^+$ is the pseudo-inverse vector (or matrix). It sets ISI to zero in a noise free scenario, i.e., when the ISI is significant compared to noise. In a high SNR channel ($SNR \to \infty$), both MMSE and ZF equalizers have asymptotic performance. However, in [58] an in-depth analysis comparing the performance of both schemes in terms of output SNR, un-coded error and outage probability, SNR gain and diversity-multiplexing gain trade off was proposed for a MIMO system analytically showing significant differences.

2.3.6 OFDM synchronization

OFDM based systems are prone to synchronization errors such as frequency sampling and symbol synchronization resulting in ICI or ISI and thus leading to link performance

degradation [60, 61]. Synchronization schemes can be typically divided into two groups: (*i*) data aided methods using pilot or training symbols sequences [62, 63] and (*ii*) non-data aided (or blind) methods, which do not require additional data transmission and are thus more bandwidth efficient [64, 65]. Timing synchronization methods are usually based on the autocorrelation of two training sequences [$A_{N/2}$ $A_{N/2}$] embedded in the OFDM signal using Schmidl-Cox algorithm [66].

The auto-correlation function using a sliding window of length $N/2$ samples is given by [66]:

$$P_{sc}(d) = \sum_{m=0}^{\frac{N}{2}-1} x_{d+m} \cdot x_{d+m+N/2}$$ (2.28)

where x_d is the received signal and d denotes the sampling index. The timing metric is then given by [66]:

$$M_{sc}(d) = \frac{|P_{sc}(d)|^2}{(R_{sc}(d))^2}$$ (2.29)

where $R_{sc}(d)$ is the energy of the received signal given by [66]:

$$R_{sc}(d) = \sum_{m=0}^{\frac{N}{2}-} \left| x_{d+m+N/2} \right|^2$$ (2.30)

The peak of the time metric M_{sc} ensures the beginning of the OFDM symbol. The auto-correlation algorithm has low computational requirements. However, the time metric shows a flat region resulting in inaccurate time synchronization estimation. Van de Beek's blind algorithm finds symbol and frequency offsets based on the maximum likelihood (ML) estimation. Considering $2N+D$ consecutive samples of the received signal x, one complete OFDM symbol is included having $N+D$ samples, where N is the number of samples per OFDM symbol and D is the length of CP. The beginning of the symbol is unknown at the Rx due to the channel delay. The two functions, i.e., a correlation term and an energy term are given by [67]:

$$\theta(m) = \sum_{k=m}^{m+D-1} x(k)x^*(k+N).$$ (2.31)

$$\varphi(m) = \frac{1}{2} \sum_{k=m}^{m+D-1} |x(k)|^2 + |x(k+N)|^2. \tag{2.32}$$

Then the time $\hat{\tau}$ and the frequency offset $\hat{\epsilon}$ are calculated by the joint ML estimation via [67]:

$$\hat{\tau} = \arg\max\{|\theta(\tau) \cdot \rho\varphi(\tau)|\}, \tag{2.33}$$

$$\hat{\epsilon} = -\frac{1}{2\pi} \angle\theta(\hat{\tau}), \tag{2.34}$$

where ρ is the magnitude of a correlation coefficient between *x(k)* and *x(k+N)* and $\angle$ denotes the argument of a complex number.

2.3.7 Peak to average power ratio of OFDM signal

While OFDM certainly offers numerous advantages, it also suffers from some performance-related problems. The high PAPR of the OFDM signal is the underlying problem that makes OFDM very sensitive to non-linear distortion. PAPR is defined as the maximum transmitted power in a given OFDM symbol divided by the average power of this OFDM symbol [68]:

$$\text{PAPR} = \frac{\text{peak power of } x(t)}{\text{average power of } x(t)}. \tag{2.35}$$

The high PAPR in OFDM is a result of adding *N* number of subcarriers through the IFFT operation. An OFDM has several independently modulated subcarriers that attains a high value of PAPR whenever they are added coherently. In other words, the addition of *N* signals having a similar phase, results in a peak power which is *N* times the average power of the OFDM signal. Thus, applying OFDM signal through nonlinear components (such as radio frequency power amplifiers or digital to analogue converters (DAC)) often results in signal distortion.

Furthermore having power amplifiers and DACs with a large dynamic range increase the cost and the complexity of the system significantly [44, 69]. In RF, the power amplifier efficiency (η) is inversely proportional to the PAPR and is given by [15, 31]:

$$\eta = \frac{0.5}{\text{PAPR}}. \qquad (2.36)$$

2.3.4.1 PAPR reduction techniques

Several techniques have been proposed to decrease the PAPR of OFDM signals, the simplest method being to clip the signal amplitude above a threshold level (*A*) such as:

$$x(t) = \begin{cases} A & \text{if } A \le x(t) \\ x(t) & \text{otherwise} \end{cases}. \qquad (2.37)$$

However, this scheme introduces in-band distortion as well as out-of-band radiation which affect the BER performance as well as introducing adjacent channel interference. Other schemes such as selective mapping (SLM), block coding, partial transmit sequence (PTS), interleaving, tone reservation (TR) and tone injection (TI)) can also decrease the PAPR of OFDM signals without introducing any distortion but at the cost of data rates, complexity or increasing transition power. A comparison between these different schemes is illustrated in Table 2.2 [44, 70].

Table 2.2 A comparison of PAPR reduction techniques [70]

Reduction scheme	Coast paid
SLM	Data rates, X_{SLM} times IFFTs operations at the Tx. Side information extraction and reverse SLM at RX
Interleaving	X_{INT} times IFFTs operation and V-1 interleaving times at the Tx, side information extraction and de-interleaving at the Rx
PTS	Data rates, X_{PTS} times IFFTs at the Tx, side information extraction and inverse PTS at the Rx
TR	Data rates and increased transmission power
Block coding	Data rates, coding or table searching at the Tx and decoding or table searching at the Rx
TI	Increased transmission power

2.3.4.2 Single carrier-frequency division multiple access (SC-FDMA)

SC-FDMA uses the same OFDMA transceiver structure with additional mapping and FFT

blocks at the Tx and de-mapping and IFFT blocks at the Rx as shown in Figure 2.12.
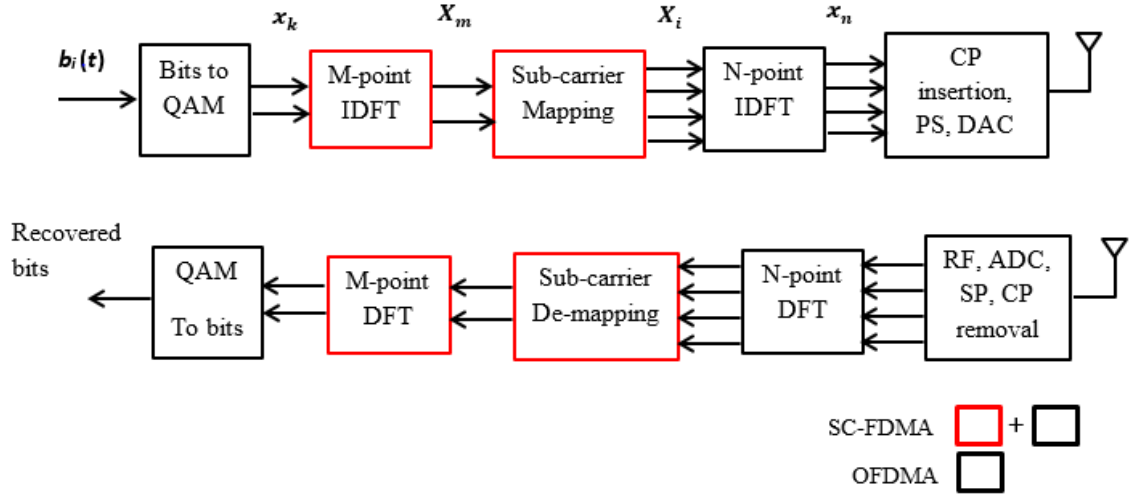
Figure 2.12. Block diagram of a SC-FDMA transciever [71]

This attractive scheme has been extensively studied in the RF domain, and is currently used

for LTE as uplink modulation schemes where a lower PAPR is essential to improve the

performance of mobile terminals in terms of transmission power efficiency [71].

Inserting FFT and subcarrier mapping blocks before the IFFT block at the OFDM Tx as

denoted by the red blocks at Figure 2.12, results in a SC-FDMA signal which shares some

charectarestics with SCM such as a low PAPR. Unlike OFDM signals, the data symbol in

SC-FDMA is distrebuted among all subcarriers which offers frequency diversity gain

through selective frequency channel [72].

Subcarrier mapping can be performed by inserting $Q - 1$ numbers of unmodulated

subcarriers between each adjacent output FFT modulated subcarriers as shown in Figure

(2.13a) (known as an interleaving mapping), or by adding C numbers of unmodulated

subcarriers after the modulated output FFT subcarriers as illustrated in Figure (2.13b)

(known a localized mapping), where Q and C are the interleaving factors of interleaving and

localization mapping resperctivesly.

31

Interleaving mapping can offer more frequncy diversity gain since the modulated subcarriers are distributed uniformly over the entire bandwidth, whereas the localized method can be combined with channel-dependant scheduling (CDS) to provide a multi-user diversity since information is spread among only a fraction of the system bandwidth. The localized and interleaving subcarrier mapping modes of SC-FDMA are denoted by LFDMA and IFDMA respectively [73].
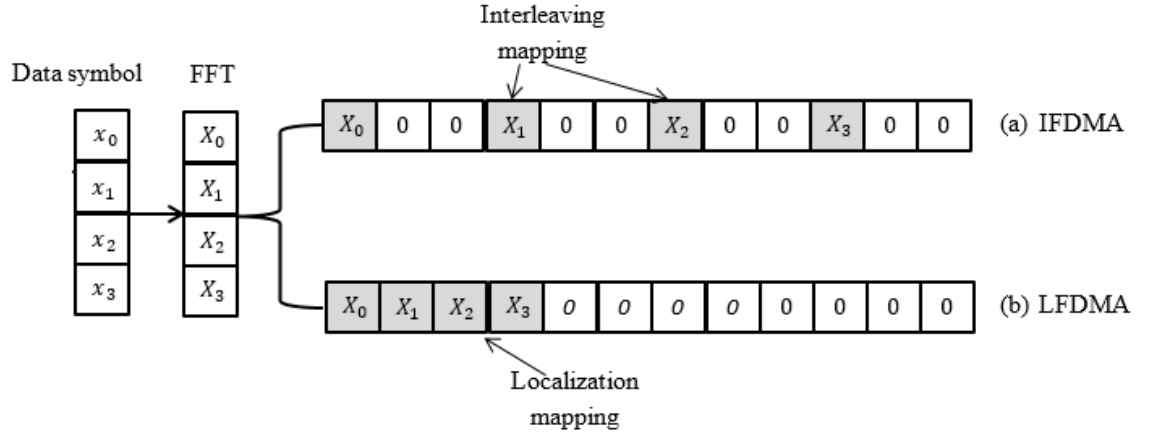
Figure 2.13. Interleaving and localization mapping where $Q = 3$ and $C = 8$ [74].

2.3.4.2.1 PAPR of SC-FDMA signals

To examine the PAPR of a SC-FDMA signal, let us analyse the baseband time domain signal (x_n) with reference to Figure (2.12) as follows: firstly, the serial binary bits $bi(t)$ are mapped into a group of a complex quadrature amplitude modulation (QAM) signals x_k where $[k = 0,1,2,3,\dots\dots\dots\dots,M-1]$ and M is the number of data per an OFDM symbol. Then x_k is transformed to the frequency domain by implementing an FFT operation where the resulting frequency domain signal X_m is given by:

$$X_m = \sum_{k=0}^{M-1} x_k\ e^{-j2\Pi\frac{k}{M}m},$$

(2.38)

Here, X_m refers to the mth subcarrier where $m = \{0,1,2,3,4,\dots\dots\dots M-1\}$. Subsequently, X_m is passed through the mapping process to result in a frequency domain mapped signal X_i where $i = \{0,1,2,\dots\dots\dots N-1\}$, $N = Q.M$ for IFDMA and $N = C + M$ for LFDMA .

Finally, the baseband discrete time domain signal x_n is obtained by passing X_i through the IFFT block. Since IFDMA and LFDMA have different mapping processes, their baseband time domain signal characteristics (or PAPR value) should also be different as will be demonstrated below.

Baseband time domain IFDMA symbol

The frequency domain mapped signal of IFDMA can be defined as:

$$X_i = \begin{cases} X_m, & \text{if } i = Q.m \text{ where } 0 \le m \le M-1 \\ 0, & \text{otherwise} \end{cases} \tag{2.39}$$

By letting $n = (M.q + m)$ for $0 \le q \le Q-1$ in (2.35) we obtain [68]:

$$x_n = x_{M.q+m} = \frac{1}{N} \sum_{i=0}^{N-1} X_i \, e^{j2\Pi\frac{i}{N}(M.q+m).}$$

$$= \frac{1}{Q} \cdot \frac{1}{M} \sum_{i=0}^{M-1} X_m \, e^{j2\Pi\frac{k}{M}m}. \tag{2.40}$$

$$= \frac{1}{Q} \cdot \left[\frac{1}{M} \sum_{i=0}^{M-1} X_m \, e^{j2\Pi\frac{k}{M}m} \right].$$

$$= \frac{1}{Q} x_k.$$

From (2.40), it can be observed that the base band time domain signal x_n is a scaled and repeated version of the original signal x_k. Hence, the PAPR of the baseband IFDMA is the same as the PAPR of the single carrier modulation signal.

Base band time domain LFDMA symbol

The frequency domain mapped signal of LFDMA can be described as:

$$X_i = \begin{cases} X_m, & \text{if } 0 \le i \le M-1 \\ 0, & \text{otherwise} \end{cases}. \tag{2.41}$$

By letting $m = (Q.n + q)$ for $0 \le n \le N-1$ and $0 \le q \le Q-1$ in (2.38), we obtain [68]:

$$x_m = x_{Q.n+q} = \frac{1}{M} \sum_{i=0}^{M-1} X_i \, e^{j2\Pi\frac{m}{M}i}.$$

$$= \frac{1}{Q} \cdot \frac{1}{N} \sum_{i=0}^{N-1} X_i \, e^{j2\Pi\frac{Qn+q}{QN}i}. \tag{2.42}$$

However, after a number of derivations as in [68], the LFDMA baseband time domain signal x_n can be given by [68]:

$$x_n = \begin{cases} \frac{1}{Q} x_k & for \; q = 0 \\ x_{Q.n+q} & for \; q \# 0 \end{cases}. \tag{2.43}$$

From (2.43), it can be clearly seen that, the base band time domain signal x_n is a scaled version of x_k only at M-multiple samples position. However, between theses possessions x_n is a sum of x_k.

Form (2.40) and (2.43) we can conclude that the PAPR of OFDMA is a larger than that of SC-FDMA. Furthermore, through the same Equations it can be observed that IFDMA has a lower PAPR value than that of LFDMA. However, the PAPR value of IFDMA can be increased if a pulse shaping filter is deployed as proved in [68].

2.3.8 OFDM frequency offset

Another major disadvantage of OFDM systems is the sensitivity to the frequency offset in comparison to the single carrier systems. Generally, frequency offset is defined as the difference between the nominal frequency and the original output frequency. OFDM has an ambiguity in the carrier frequency that occurs due to the difference in the frequencies of the local oscillators at the Tx and Rx, which in turn leads to a change in the frequency domain. This change is also known as the frequency offset. The demodulation of a signal having an offset in the carrier frequency may lead to a significant bit error rate and might also affect the output of a symbol synchronizer. Thus it is essential to calculate the frequency offset and remove or decrease its effect [75].

Let us denote the frequency offset by Δf_c, the transmitted OFDM signal by $s(t)$, and the received signal by $y(t)$. In such a case, the followings hold [67]:

$$s(t) = e^{jwt}x(t). \tag{2.44}$$

$$y(t) = e^{j(w-w')t}x(t). \tag{2.45}$$

$$\Delta w = w - w' = 2\pi\Delta fc. \tag{2.46}$$

The received signal will have an offset equal to:

$$Y(nT) = e^{j\Delta wnT}. \tag{2.47}$$

The frequency output of every sub channel must be equal to 0 at all other subcarrier frequencies which means that the sub-channels must not disturb one another. The impact of frequency offset leads to the fall of orthogonality among the subcarriers and causes inter carrier interference [75].

2.4 Summary

As an OFDM modulation scheme is the foundation of this research work, the attractive benefits of OFDM were discussed in detail in this chapter. Those benefits include converting the selective fading channel into a flat fading channel by dividing the available bandwidth into a number of sub-bands, mitigating ISI as well as reducing Rx complexity through the insertion of a CP. Furthermore, the challenges facing OFDM such as OFDM PAPR and OFDM offset and their proposed solutions were also discussed in this chapter.

The SC-FDMA signal scheme was also introduced in this Chapter as an attractive OFDM modified version that can offer most OFDM features (i.e. reducing ISI) with lower PAPR value. These modifications were done by adding interleaving mapping and FFT blocks before the implementation of the IFFT operation at the OFDM Tx (i.e. IFDMA), or by inserting the location mapping block and FFT block before the IFFT block at the OFDM Tx (i.e. LFDMA). A comparison between IFDMA PAPR and LFDMA PAPR was also conducted, where IFDMA had lower PAPR (see section 5.7).

CHAPTER 3

OFDM IN VISIBLE LIGHT COMMUNICATION SYSTEM

3.1 Introduction

As the main concept of this research is to improve the performance of OFDM in VLC system, VLC background including the implementation of OFDM in VLC will be illustrated in this chapter. VLC represents unique technology combining illumination, data transmission and localization (mostly indoor).

Due to the white LEDs utilisation, VLC has become a suitable candidate for future generation communication networks offering energy efficient service, almost unlimited bandwidth within the unregulated part of the electromagnetic spectrum and potentially low-cost solution [6, 76]. Despite the fact that LEDs are bringing most of the mentioned advantages, they also behave as a limiting factor in the communication network due to their very low modulation bandwidth in the region of units of few MHz. Thus, most of the research works have been focused on the increasing data rates [9, 12, 34, 77].

The chapter structure is as a follow; the basic concepts behind VLC system such as VLC transceiver structure, LED modulation bandwidth, VLC channel model and, VLC challenges will be illustrated in section 3.2. The benefits and the challenges behind the implementation of OFDM in VLC system will be illustrated in section 3.3 as a number of modified OFDM

schemes will be demonstrated in this section. Finally, a summary of this chapter is introduced in Section 3.4.

3.2 Visible Light Communications

Recently, VLCs have been the focus of enormous attention as the candidate for future broadband networks by utilising white LEDs in the existing solid-state lighting (SSL) infrastructure. LEDs can be switched on and off very rapidly without any perceptible effect on human eye to offer multiple use such as illumination, high speed data transmission and localization in various applications.

Moreover, the LEDs have been installed into cars, aircrafts, traffic lights or street lamps spreading the possible utilisation of VLC to various applications: (*i*) visible light positioning [78, 79]; (*ii*) car-to-car (C2C) or car-to-infrastructure (C2I) communication [80, 81]; (*iii*) machine-to-machine (M2M) communication or the internet of things (IOT) [82, 83]; and (*iv*) toys and there park entertainment [84, 85] as illustrated in Figure 3.1.

In spite of the outstanding results achieved by the research and industry, the history of VLC is quite short. The first publications based on the theoretical investigation were reported in the beginning of the 2000s by the Keio University in Japan [86, 87]. Since that time VLC has experienced rapid development from the standardization processes [88] to several Gbit/s transmission systems [89, 90].

According to the processes within the IEEE 802.15.7r1 working group, four use cases for high data rate VLC were adopted: (*i*) indoor office/home applications (museums, general offices, shopping centres, railways, airports, hospitals); (*ii*) data centre, industrial and secure wireless scenarios (factories, hangers, manufacturing cells); (*iii*) vehicular communications (C2C and C2I); and (*iv*) wireless backhaul (small cell backhaul, surveillance backhaul, local area network (LAN) bridging) [91].

Another important VLC feature is the possibility of safe communication since optical radiation does not penetrate walls. Additionally, VLC is ideal for being used in hospitals,

aircraft cabins or in petrochemical industries since it does not interfere with any RF systems and does not induce any health issues. The deployment of VLC is based on the installation of the existing technologies like power line communication (PLC) and power-over-Ethernet (PoE) and usage of SSL infrastructures based on LEDs, which significantly reduces energy consumption by combining illumination and data transmission at the same time.
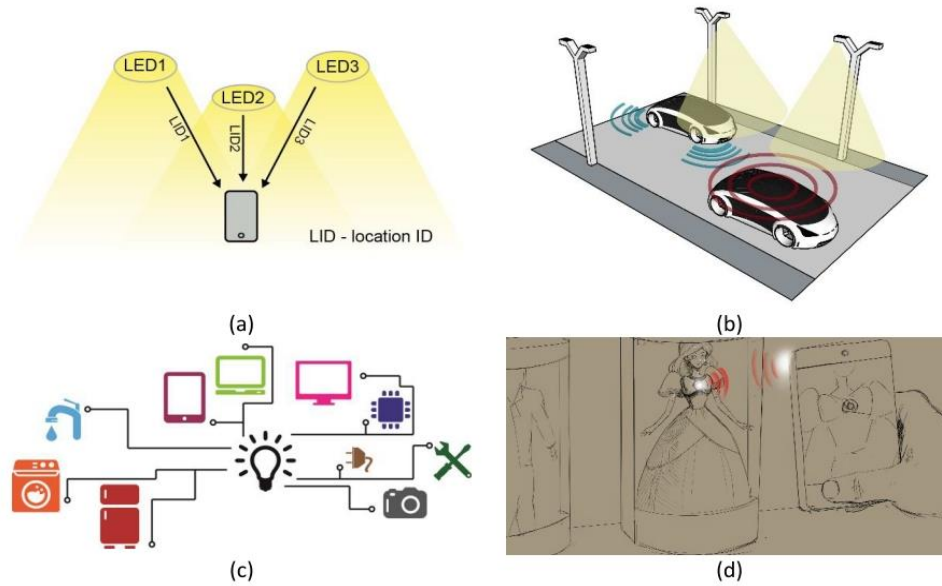
Figure 3.1. VLC applications

3.2.1 Comparison between VLC and RF

VLC cannot avoid being compared with the well-established and known RF based communication systems. As mentioned, one of the key advantages for VLC lies in the utilisation of the unregulated and practically unlimited visible part of electromagnetic spectrum in contrast to strictly regulated and congested RF spectrum becoming a bottleneck of the system.

Since VLC is based on the utilisation of LEDs as transmitters, it provides several possible services without any electromagnetic interference in contrast to the RF systems with the only communication purpose. Moreover, such technology will be energy efficient offering relatively low-cost solution for the future communication networks.

On the other hand, VLC suffers from numerous disadvantages compared to traditional RF communications. The achievable data rates decrease very quickly with increasing distance between a transmitter and a receiver limiting the range of high speed VLC usage. The VLC path loss is inversely proportional to the distance raised to the power of four unlike RF where it is power of two [92]. Additionally, LED lights must be turned on to provide the same high-speed connections as Wi-Fi. Thus, VLC is not going to replace RF based systems as both technologies are complementary offering together superior performance. The comparison of both technologies is outlined in Table 3.1.

Table 3.1 VLC and RF communication technologies comparison [6].

PROPERTY	VLC	RF
Bandwidth	Unlimited	Limited and regulated
Electromagnetic interference	No	Yes
Distance	Short	Short to long
Security	Good	Poor
Services	Illumination, communication, localization	Communication
Noise sources	Sun light, other ambient lights	All electrical appliances
Power consumption	Relatively low	Medium
Mobility	Limited	Good
Coverage	Narrow and wide	Mostly wide

3.2.2 Light emitting diode

In recent years, LEDs have replaced traditional lights in the home/office lighting systems due to their high energy efficiency. For instance, compared to the traditional incandescent and fluorescent lamps, whose luminous efficiency is limited to 51 lm/W and 90 lm/W, respectively, the efficiency of white LEDs exceeding 200 lm/W was already demonstrated [6, 93].

The last but not least benefits are long life expectancy, low power consumption, the absence of mercury or high tolerance to humidity. Thus, high power white LEDs are ideal sources to be used for both illumination and communication purposes.

3.2.2.1 Types of LEDs

The LEDs used as VLC transmitters emit white light that can be produced by two different processes. Thus, there are two types of LEDs as illustrated in Figure 3.2: (*i*) RGB LED that emits white light by combining three basic colours red (R, 625 nm), green (G, 525 nm) and blue (B, 470 nm) and (*ii*) white phosphor LED (WP LED) utilising a blue chip covered by a yellowish phosphor layer causing the shift to the longer wavelengths. The RGB LEDs are attractive since three individual chips can be used for simultaneous data transmission adopting wavelength division multiplex (WDM) [94, 95]. However, the latter approach is usually preferred by manufacturers due to the lower complexity and cost [96]. The most dominant inorganic LED is made of gallium nitride (GaN) coated by the yellowish cerium doped yttrium aluminium garnet (Ce:YAG) phosphor layer.
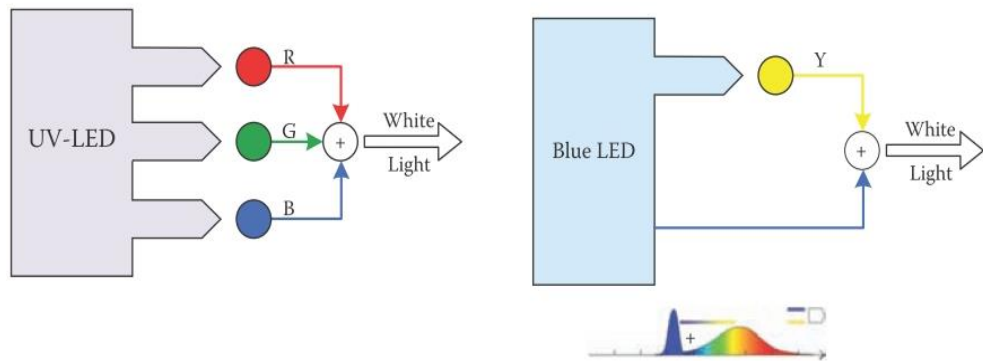
 Figure 3.2. Two types of LED with different way of producing white light [6]

However, both RGB LEDs and WP LEDs are not suitable for producing large area panels desirable for SSL and VLC applications due to the manufacturing methods. Thus, organic LEDs (OLEDs) appear as a candidate for certain VLC applications. OLEDs have several advantages over inorganic LEDs such as large and arbitrarily shaped panels, smoother lighting effects, mechanical flexibility, longer lifetime and mechanical flexibility.

3.2.2.2 LED Modulation Bandwidth

Although using LEDs brings many advantages as stated, their low modulation bandwidth is a bottleneck of a VLC network while behaving as a first order low pass filter (LPF) [9]. The bandwidth is affected by the (*i*) injection current; (*ii*) junction capacitance; and (*iii*) parasitic capacitance however, the capacitance values are usually given.

Increasing the input current can further improve the LED bandwidth on the other hand, the effect of capacitances can be reduced by superimposing an AC signal on a constant DC-bias. The LED output optical power P_0 at a frequency ω is given as [97].

$$\frac{P(\omega)}{P_0} = (1 + (\omega\tau_v)^2)^{-\frac{1}{2}}, \tag{3.1}$$

where τ_v is the minority carrier lifetime. The 3 dB bandwidth is then obtained when (3.1) is equal to 0.5. The 3 dB modulation bandwidth of inorganic LEDs is limited within the few MHz region [9, 12]. For instance, blue light emitting GaN based LED have a bandwidth up to 20 MHz, however slow transient response of the yellowish phosphor layer significantly degrades it below 5 MHz (depends on the manufacturer) [98]. On the other hand, micro-LEDs with a bandwidth exceeding 800 MHz have already been introduced [99]. Nevertheless, such a micro-LED has active area of hundreds of μm^2 resulting in very low optical output power (units of mW), which significantly limits its applications.

Thus, there exist several approaches on how to combat LEDs bandwidth limitation phenomenon and increase the transmission speed such as blue filtering where the slow yellowish component is filtered out, which increases the 3 dB bandwidth up to tens of MHz [12, 98]. On the other hand, using a blue filtering causes the signal power reduction which resulting in much lower SNR [100]. Alternatively, equalization can be used to increase the data rates such as pre- and post-equalization techniques using analogue circuits [101, 102] and digital equalizers based on the signal processing [103, 104]. In recent years, utilisation of spectrally efficient modulation formats has focus of huge attention how to combat a band limitation in VLC systems [13, 105, 106].

3.2.3 IM/DD and LED nonlinearities

The transmitting and receiving the signal using LED and photodetector (PD) is based on the IM/DD technique (i.e. the signal must be real and positive signal). To transmit the signal the intensity of an LED source is directly modulated by varying the drive current (see Figure. 3.3). At the receiver, a PD generates the electrical current which is proportional to the optical power incident on the PD. Thus, DD technique is also known as the envelope detection. Unlike coherent detection, DD systems do not require any local oscillator. Each LED is characterized by the transfer function known as *L-I* curve where *L* stands for the optical output power and *I* stand for the driver current as illustrated in Figure. 3.3. An LED must operate in the proper operating in the linear region of the *L-I* curve to ensure the optimal transmitter performance. The operation point is set by the DC drive current (denoted by red circle in Figure. 3.3). If the operating point (or drive current) is pushed too high to the nonlinear region of the LED or beyond the signal distortion occurs is results in system performance degradation [6, 10].

Single carrier modulation such as multi-level pulse position modulation (*M*-PPM) or multi-level pulse amplitude modulation (*M*-PAM) can be adjusted within the LED linear region due to their finite limited intensity levels resulting in negligible impact of LED nonlinearity. On the other hand, multi-carrier modulation schemes such as optical orthogonal frequency division multiplexing (O-OFDM) generate signals with high PAPR. Such signals are affected by the nonlinear region of an LED resulting in the increased BER.

However, the linear region on the transfer function can be maximized using a pre-distortion of the transmitter transfer characteristic as demonstrated in [107]. Besides the nonlinear region of an LED transfer function, LED degradation caused by aging and junction temperature variations have also negative impact on the system performance, which has been published in [108].
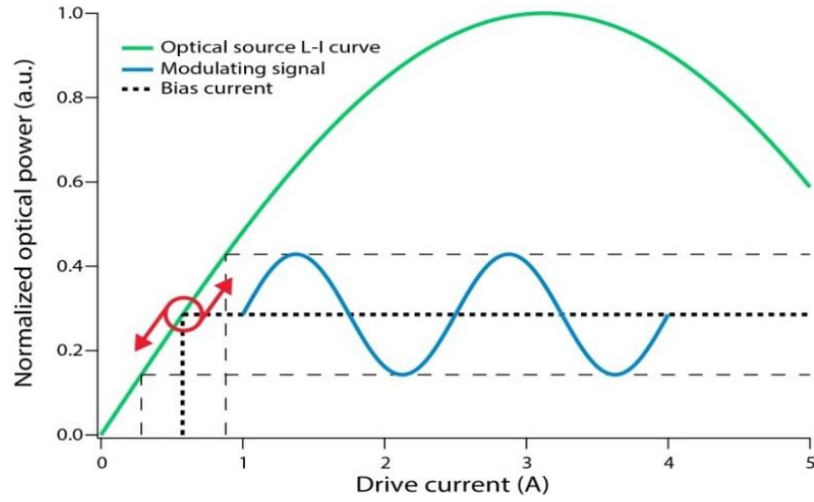
Figure 3.3. LED L-I curve and intensity modulation, the operating point is denoted by red circle

3.2.4 Illumination using white LEDs

As the LEDs serve originally for the illumination of the indoor environments it is necessary to pay attention when designing the VLC system to stay within lightning constraints. The illumination level requires being within the limit 400 – 1000 lx for typical office room at a desk level. However, even if no illumination is required, energy-efficient IM/DD techniques have been developed to maintain data transmission, even if the lights are visually off [109]. Basically, the constraints can be divided into two categories (*i*) illumination perception constraints and (*ii*) LED luminaires constraints [92].

The first category includes mainly illumination level (or dimming level), colour temperature (CT), colour rendering index (CRI) and finally, aesthetics and practical reasons when placing LED lights inside the rooms. The dimming control is crucial since VLC system must keep its functionality even when users change the illumination level by dimming the lights. Thus, several methods combating dimming issue were introduced in IEEE 802.15.7 standard such as adjusting the amplitude of on-off keying (OOK) pulses or changing the pulse width in electronics and optical system should enable numerous functionalities such as dimming control, heat sinking, and efficient power supply to name few. Thus, it is necessary that the lighting conditions and VLC system performance will not be distorted meeting the above-mentioned specifications.

3.2.5 Photodetectors

The PD is an optoelectronic device that generates electrical current proportional to a square of the optical power incident on its surface. Thus, the output electrical current is proportional to the received optical power and is given by the responsivity of the photodetector based on the used semiconductor material. The semiconductor material responsivity R (A/W) is illustrated in Figure 3.4, showing the most common materials for inorganic receivers. Clearly, the Si semiconductors are usually utilised for detection in VLC.
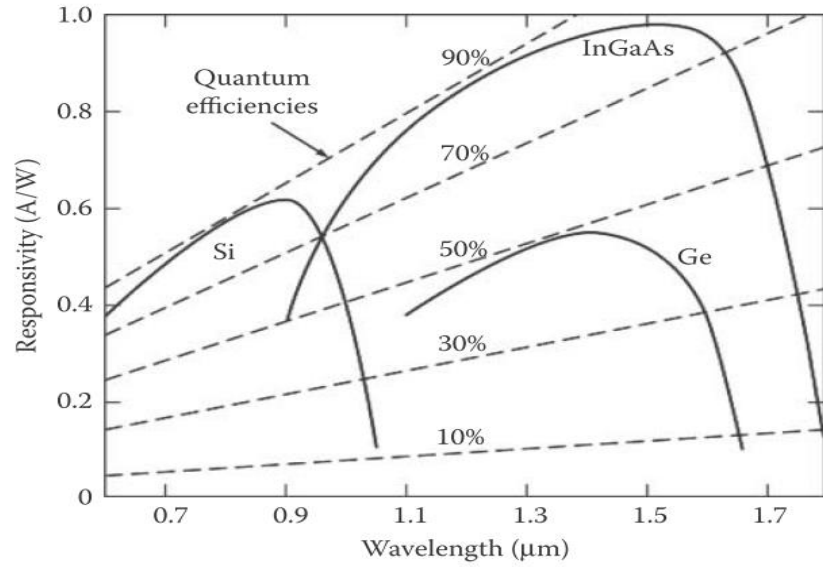
Figure 3.4. The semiconductor material responsivity [6]

There are four types of photodetectors that can be used for receiving the optical signals: (*i*) PIN photodiodes, (*ii*) avalanche PD (APD), (*iii*) photoconductors and, (*iv*) metal semiconductor PDs. First two, PIN PDs and APDs are mostly used in the receivers for VLC. However, APDs provides internal gain which is usually within the range 150-250 [6]. Thus, the responsivity of APD can be greater than unity in contrast to PIN responsivity, which is always below 1. Moreover, the APDs offer higher sensitivity than PIN detectors. On the other hand, the gain of APDs is associated with additional noise, which must be taken into account. The typical PIN PDs and APDs characteristics for different semiconductor materials are listed in Table 3.2.

Table 3.2 Typical characteristics of the PIN PDs and APDs [6]

Parameter	Silicon		Germanium		InGaAs	
	PIN	APD	PIN	APD	PIN	APD
Wavelength range (nm)	400-1100		800-1800		900-1700	
Peak (nm)	900	830	1550	1300	1300-1550	1300-1550
Responsivity (A/W)	0.6	77-130	0.65-0.7	3-28	0.63-0.8	0.75-0.97
Quantum efficiency (%)	65-90	77	50-55	55-75	60-70	60-70
Gain	1	150-250	1	5-40	1	10-30
Bias voltage (-V)	45-100	220	6-10	20-35	5	<30
Dark current (nA)	1-10	0.1-1	50-500	10-500	1-20	1-5
Capacitance (pF)	1.2-3	1.3-2	2-5	2-5	0.5-2	0.5
Rise time (ns)	0.5-1	0.1-2	0.1-0.5	0.5-0.8	0.06-0.5	0.1-0.5

3.2.5.1 Photodetector noise

The photodetector noise is crucial since it determines the device lower sensitivity limit. The primary noise sources are the shot noise σ_S^2 and thermal noise σ_T^2 (Johnson noise) caused by the photocurrent fluctuations and by the receiver electronics respectively. The shot noise is caused by the fact that the number of photons incident on the photodetector per second is not constant and follows Poisson distribution resulting in the photon fluctuations. The shot noise is given as [10]:

$$\sigma_S^2 = 2qI_dB_f,$$
(3.2)

where B_f is the bandwidth of the filter following the photodetector, q is a charge of an electron and I_d is the dark current. The dark current is presented even when no light incidents on the receiver resulting in the noise generation. The dark current is determined by the PD material and by the size of photoactive area. The thermal noise is caused by the thermal fluctuations of electrons in any receiver electronics and is given by [10]:

$$\sigma_T^2 = \frac{4kT_e}{R_e}B_s,$$
(3.3)

k is the Boltzmann constant, B_s is the system bandwidth and T_e and R_e are equivalent temperature and resistance, respectively.

3.2.6 Indoor VLC channel modelling

Besides the mentioned challenges developing complex VLC channel model is still an open issue for the research community worldwide. Algorithms developed for IR channel models are usually utilised such as (*i*) recursive method and its modifications; (*ii*) Monte Carlo ray tracing; and (*iii*) others like ceiling bounce model or curve fitting [110, 111]. Thus, there is a need to improve existing channel models to be suitable for the different VLC applications. The wavelength dependency of the indoor materials must be considered when developing the channel model in contrast to IR band where the reflectance coefficient is almost flat within the utilised wavelength range.

However, several channel models not including the spectral dependent reflectance have been already published [112-114]. The spectral coefficients of the different building materials were measured in [115] varying in the range of 0.1 – 0.8 as depicted in Figure 3.5 (a) resulting in the key step within the VLC channel model development. The calculated channel impulse response is illustrated in Figure 3.5 (b). The first peak comes directly from the LED and the other peaks are dispersed due to the multiple reflections. Differences in amplitude are caused by varying reflectance coefficients.
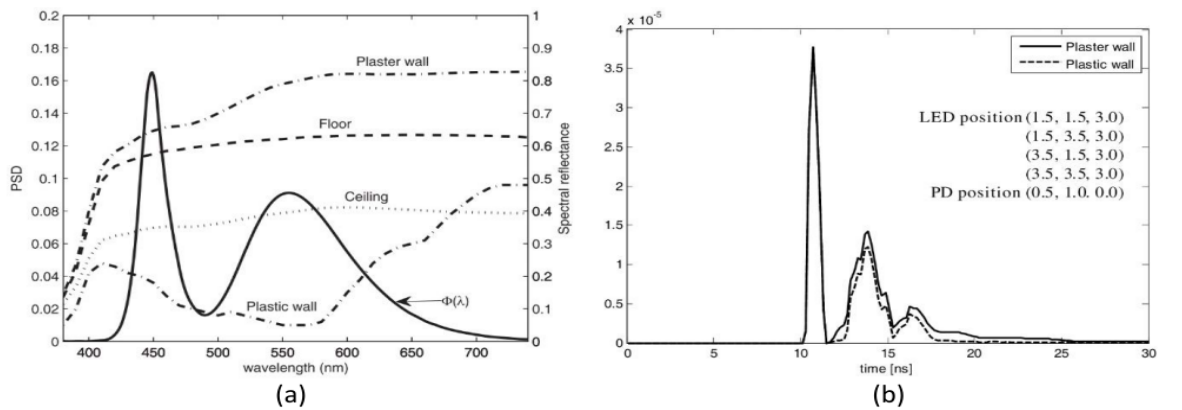
Figure 3.5: (a) Reflectance coefficients for different materials and (b) resulting channel impulse response [115]

In most of the cases, the received signal is often a superposition of the LOS path and several multipath signal that have undergone specular or diffuse reflection. The effect of the multipath reflections on the channel frequency response was investigated using a parameter called *K*-factor in [116]. The *K*-factor ensures the power ratio between the LOS and NLOS components of the received signal. Figure 3.6 illustrate how the frequency response of the optical channel depends on the value of *k*-factor where the high *K*-factor value i.e k=10 dB offers almost flat response.

However, the blockage of the LOS component results in the reduced channel bandwidth inducing the lower *K*-factor value [117]. Regarding NLOS VLC, multipath propagation introduces negative impact on the VLC positioning system decreasing the positioning accuracy [118]. Next, the effect of multipath reflections on the signal to interference plus noise ratio (SINR) has been shown demonstrating that higher order reflections have stronger negative impact on the SINR than first order reflections when a narrow FOV receiver is utilised [119].
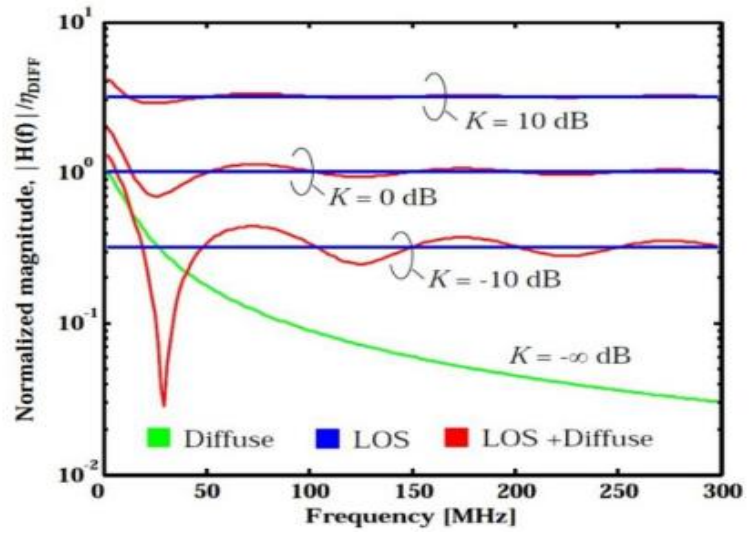
Figure 3.6. Channel frequency response for a range of K-factor where $|H(f)|$ is the magnitude of the total channel frequency response and, η_{DIFF} is the diffuse path gain [117]

The novel approach for VLC channel modelling in terms of the dynamic environment has been introduced in [120]. The effect of shadowing caused by people moving within the room has been investigated showing the inconsiderable impact on the optical received power.

Additionally, the data has been compared for different scenarios such as corridor, empty hall and furnished office room. Very complex VLC channel model based on the ray tracing algorithm has been presented in [121]. Several types of the reflections have been included such as purely diffuse, specular and mixed specular-diffuse. Moreover, the presence of an object within the room and wavelength dependent reflectance of the indoor surfaces has been included. The work has been focused on the parameters such as channel impulse response, DC gain, RMS delay spread, and coherence bandwidth and the results have been compared with the IR band.

The calculated RMS delay spread and coherence bandwidth versus the distance between Tx and Rx are illustrated in Figure 3.7 (a) and 3.7 (b), respectively. Clearly, the differences between visible and IR wavelengths are significant. The coherence bandwidth decreases when the distance between Tx and Rx increases in contrast to RMS delay spread that grows to its maximum value and then decreases. The channel coherence bandwidth is a critical parameter for multicarrier modulation formats such as OFDM. When the bandwidth of the modulated signal is less than the coherence bandwidth of the optical channel, each subcarrier can be considered as flat fading [122].

(a) (b)
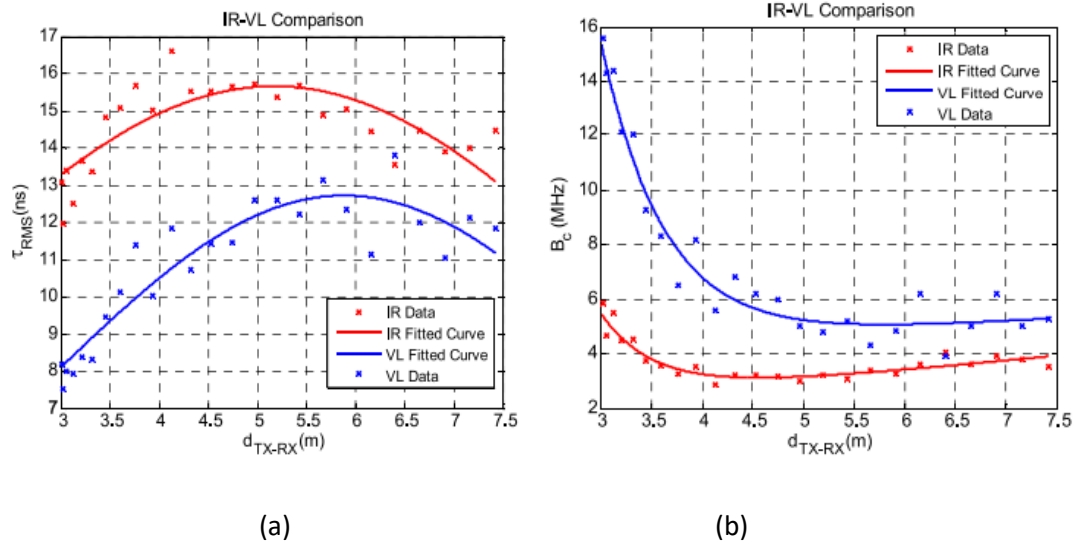
Figure 3.7. Calculated (a) RMS delay spread and (b) coherence bandwidth for IR and VLC channels against the distance between a Tx and a Rx [121].

3.2.7 VLC challenges

VLC has undergone a rapid development in recent year starting with the pioneering works in the beginning of the 2000s in Japan and demonstrating several Gbit/s transmission speed nowadays. However, to be fully implemented in the practical communication systems several challenges need to be addressed within the research community. As described, the LED modulation bandwidth is still the main drawback in achieving high data rates. The methods to combat the low bandwidth issue can results in the received power reduction, which is undesirable (blue filtering) or in the increasing the system complexity using the transmitter/receiver equalization and complex modulation schemes.

Thus, there is a need to further investigate these techniques to find optimal solutions for particular VLC applications. The link capacity increasing techniques where multiple LED sources and multiple PDs are utilised in the Tx and Rx, respectively, are still an open issue and requires further investigation. The diversity techniques and error detection mechanisms of the multiple input and multiple output (MIMO) system are still challenging. The nonlinear features of the off-the-shelf LEDs degrades the system performance thus there is a need for optimisation of the time domain signal within the linear region of the LED transfer function for maximizing the link throughput.

Another issue connected with VLC is the provision of uplink. The most suitable technique to provide bidirectional communication is wavelength division duplexing (WDD) utilising different wavelengths for uplink and downlink. IR based links are feasible option for transmitting data in the uplink direction [10]. The combination of RF (uplink) and VLC (downlink) systems was investigated [123]. The VLC channel modelling still needs more in-depth investigation although several extensive studies were already published. The future channel models should be more generalized including the effects of LED sources and room size, improvement in measuring channel reflection characteristics and the research on multipath effect in the VLC channel [124].

Moreover, VLC must be coordinated within several standards resulting from the wide range of applications. Thus, the VLC standard must encompass illumination regulations, automotive standards and others. Among others, the flicker mitigation and support of the lights dimming are VLC challenges connected with the illumination and energy efficiency. Finally, several challenges need to be met in the commercialisation process of VLC resulting from the fact that two different industries must cooperate together. The lighting original equipment manufacturers are required to include several modifications into their light sources and mobile device manufacturers need to equip their devices by high-speed PDs [125]. Figure 3.8 illustrates the most interest research activities including challenges and opportunities in VLCs.
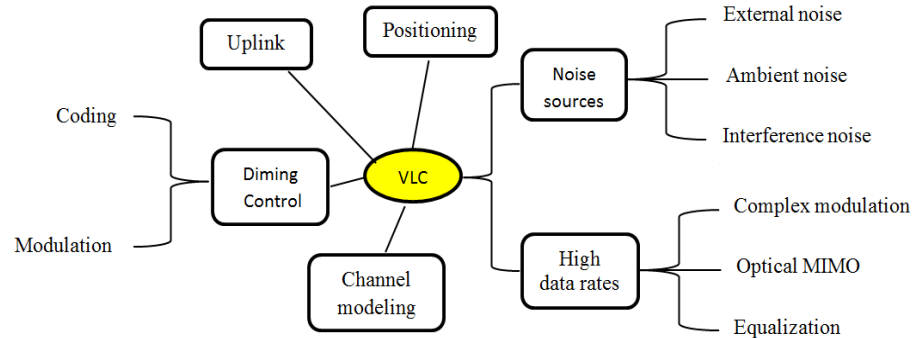
Figure 3.8. VLC research map

3.3 OFDM in VLC Systems

In VLC, selecting the modulation scheme is a key step in the design of the communication system. The selected modulation should offer the required performance based on the following criteria: (*i*) power efficiency; (*ii*) bandwidth efficiency; (*iii*) transmission reliability; and (*iv*) other considerations such as cost or robustness to ambient light.

Single-carrier modulation schemes such as *M*-PPM and *M*-PAM have been straight-forwardly implemented in IM/DD based VLC by encoding the information to the pulse duration. *M*-PPM utilises the position of the pulse [6], while *M*-PAM encodes the data into

the amplitude of the pulse [10]. Both modulation techniques are very popular since PAM and PPM are the most bandwidth efficient (apart from QAM) and the most power efficient modulation schemes, respectively [10].

However, M-PAM is more sensitive to channel nonlinearities and noise when compared to the binary schemes. OOK is a type of M-PAM modulation based on two levels ($M = 2$) and is still one of the most commonly used due to its implementation simplicity and bandwidth efficiency [126, 127]. As such, both return to zero (RZ) and non-return to zero (NRZ) techniques can be easily implemented. However, OOK-RZ bandwidth requirement is twice that of OOK-NRZ, which must be taken into account. Nonetheless, the limited bandwidth of LEDs and the indoor multipath propagation issues make all of these aforementioned modulation schemes impractical to support high data rates in VLC systems [10, 14]. Alternatively, in recent years, spectrally efficient modulation formats such as OFDM have been the focus of substantial research effort and attention.

The main advantage of OFDM is the fact that it offers an effective solution to reducing ISI in bandlimited systems. Since data transmission occurs in parallel, the symbol period takes a much longer time than in serial data communication with the same data rate. As such, ISI affects at most one symbol, which simplifies the equalisation process. Furthermore, the low frequency noise caused by a DC wandering and flickering interference of fluorescent light is mitigated as the first OFDM subcarrier is unmodulated [14]. Finally, OFDM can compensate the performance degradation at frequencies outside the 3dB modulation bandwidth by using its bit and power-loading feature [128]. As such, OFDM is a robust candidate modulation scheme that can support high data rates in VLC systems. For instance, a 3 Gb/s VLC system was reported in [16]. Other VLC systems offering Gbit/s data rates using OFDM were also demonstrated in [37, 129-131].

Although OFDM offers several advantages, its performance in VLC systems is adversely affected by two limitations: *i*) In IM/DD based VLCs, the complex and bipolar signal formats such as the traditional OFDM cannot be used since the light intensity cannot be complex or

negative (Chapter 3, subsection 3.2.3). Thus, DCO-OFDM, ACO-OFDM and, PAM-DMT have emerged as the most popular OFDM schemes adopted in IM/DD VLC systems [34, 132, 133]. However, all these adaptations have been implemented at a cost of spectral efficiency as in ACO-OFDM and PAM-DMT or at a cost of power consumption as in DCO-OFDM [10, 134]. All these aforementioned optical OFDM schemes will be described in detail in the next subsections.

ii) In VLC, LEDs only work linearly in a limited range (Chapter 3, subsection 3.2.3). Therefore, implementing a high PAPR signal such as an OFDM through this limited range can affect the BER performance as well as the illumination and diming control feature of the VLC system. Nevertheless, this OFDM drawback has been intensively studied in the RF domain as its amplifier is also a limited linear device. A number of techniques have been reported in the RF domain to address this OFDM disadvantage as explained in details in subsection 2.3.7. Most of these RF techniques have been implemented in VLC to improve its system performance. Recently, SC-FDMA was adopted for IM/DD based VLC systems to improve the PAPR. A LED array with SC-FDMA was implemented in [25] to reduce the OFDM PAPR in a VLC system at a cost of the transmission rate per LED transmitter due to the interleaving and localised mapping implementation. ACO-single carrier frequency domain equalization (ACO-SCFDE) and repetition and clipping optical SCFDE (RCO-SCFDE), were demonstrated in [23] and [135] respectively as two modified SC-FDMA schemes with the same data rates per single LED transmitter as in ACO-OFDM. The only difference between ACO-SCFDE and the traditional ACO-OFDM is the additional FFT and IFFT blocks at the Tx and the Rx, respectively. Unlike ACO-SCFDE where only the odd subcarriers are modulated, in RCO-SCFDE, the real OFDM signal is transmitted via two blocks. The first block is used to transmit the real positive samples, whereas the negative real samples are transmitted by the second block. Thus, achieving reduced IFFT length compared to ACO-SCFDE. The system model of ACO-SCFDE will be presented in subsection 3.2.4.

3.3.1 DCO-OFDM

Figure 3.9 shows a block diagram of a DCO-OFDM transmitter which is similar to the traditional OFDM one. The main difference is the inclusion of HS and DC-biased blocks. The HS block is placed before the IFFT block while the DC-biased block is inserted before the optical to electrical conversion (OEC) block which is used in this case as a transmitter instead of a traditional RF antenna.
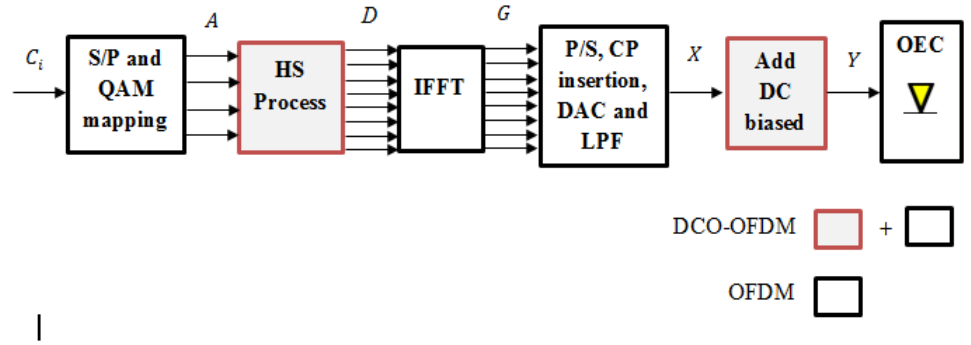
Figure 3.9. A DCO-OFDM transmitter

As illustrated in Figure 3.10, one can notice that HS is implemented by adding a complex conjugate to the IFFT input to make its output a real signal at a cost of half of the electrical bandwidth. In the meantime, the DC-biased block is added to the OFDM signal to make it positive at a cost of power consumption before being transmitted through the LED [136].
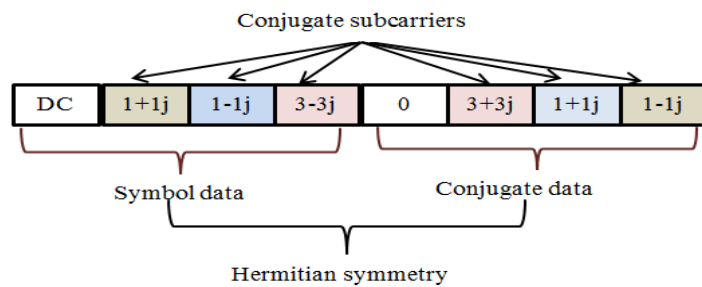
Figure 3.10. Implementation of HS

After the serial to parallel (S/P) and QAM mapping processes, the resulting symbols A will be imposed to the HS process before being passed through the IFFT block where, $A = [A_0, A_1, A_2, ... A_{B-1}]$ and, B denote the data symbols and the number of data symbols

respectively. Therefore, the IFFT output is a real signal. The HS processing is expressed as [136]:

$$D_i = \begin{cases} A_i & i \leq N/2 - 1 \\ 0 & i = \dfrac{N}{2} \\ A^*_{N-i} & i \geq N/2 + 1 \end{cases}, \tag{3.4}$$

$$D = [0, A_0, A_1, A_2, \ldots A_{B-2}, A_{B-1}, A_B, 0, A^*_B, A^*_{B-1}, A^*_{B-2}, \ldots A^*_2, A^*_1, A^*_0], \tag{3.5}$$

where the length of D is N and, $N=2B+2$. To mitigate the low frequency noise the following relation should be satisfied: $D_0 = D_{\frac{N}{2}} = 0$. Finally, after the IFFT operation the real OFDM signal is passed through the PS, CP insertion, DAC and LPF blocks before being added to the DC-bias and transmitted through the LED.

Because of a large OFDM PAPR, a high DC-bias that is equal to the highest negative OFDM amplitude should be added to the OFDM signal (see Figure 3.11) to meet the IM/DD obligation. However, this makes DCO-OFDM inefficient in term of power consumption as well as dimming control and can cause a clipping noise [10].
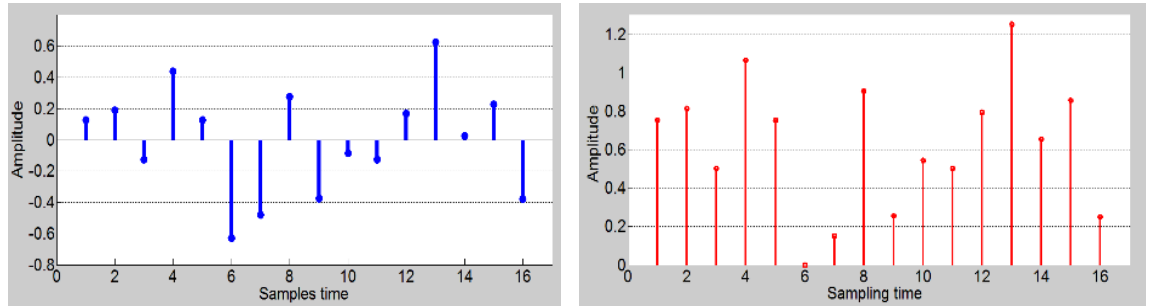
(a) Before adding dc-bias   (b) After adding dc-bias

Figure 3.11. DCO-OFDM time domain signal before and after adding the DC-bias where the number of sub-carriers is 16 and M=16 QAM

According to central limited theorem, the OFDM signal has a Gaussian distribution with a zero mean and σ standard deviation for 64 IFFT points or more [137]. Therefore, a probability of 97.5% that the OFDM signal is positive can occur by adding a DC-bias equal to $2\sigma^2$ as suggested in [138] while the remaining negative values are clipped.

In general, a DCO-OFDM signal is firstly scaled and clipped by fixed scaling and clipping factors according to the LED dynamic range and the DC-bias is set on the middle point of the LED dynamic range. As different OFDM symbols can have different distributions, adaptive scaling factors and adaptive DC-bias have been introduced by [139] to improve the system performance by exploiting the whole linearity range of the LED.

However, the illumination feature is the main advantage of the LED, and hence DCO-OFDM may not be recommended in some VLC applications where the power consumption is a crucial requirement [14]. Alternatively, less optical OFDM power consuming schemes have been proposed at a cost of spectral efficiency and amongst them are ACO-OFDM and PAM-DMT which are described in details in the next subsection.

3.3.2 ACO-OFDM

In order to provide a unipolar OFDM time domain signal, the advantages of IFFT properties have been exploited in ACO-OFDM at a cost of the spectral efficiency. This can be achieved by setting the input IFFT even subcarriers to zero and as a result the output IFFT samples will have an antisymmetric feature. Clipping the antisymmetric negative samples does not cause any information loss or any clipping noise as the clipping noise will only affect the even subcarriers (i.e. unmodulated subcarriers) as proved in [132]. As the ACO-OFDM signal is processed by odd modulation and HS operations (see Figure 3.12) before the IFFT implementation in order to provide a real antisymmetric time domain signal (see Figure 3.13), its spectral efficiency is reduced by half for the DCO-OFDM.
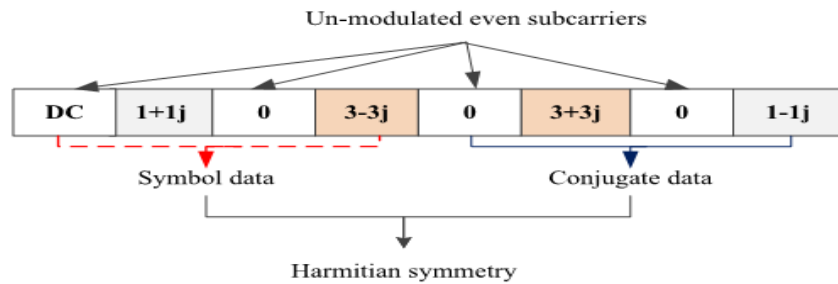
Figure 3.12. The implementation of odd modulation and HS in ACO-OFDM
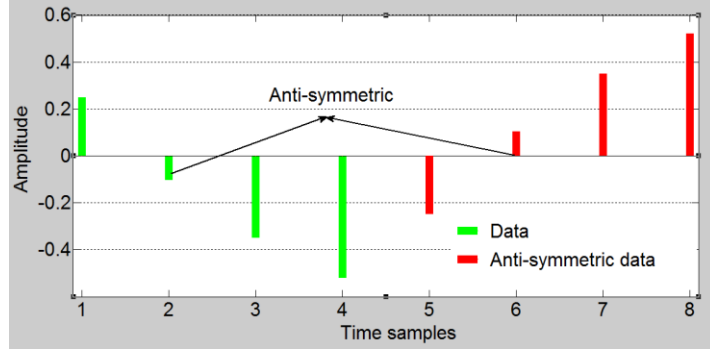
Figure 3.13. Antisymmetric ACO-OFDM time domain signal

Consequently, ACO-OFDM is more efficient in terms of the optical power requirement compared to OOK, and has a low clipping noise level compared to DCO-OFDM whereas DC-OFDM is more bandwidth efficient [140]. A comparison between ACO-OFDM and DCO-OFDM in AWGN channel done at the same data rates (M-QAM DCO-OFDM compared to M^2-QAM ACO-OFDM) in term of the SNR against the BER performance have been reported in [141] where the results show that ACO-OFDM is outperforms DCO-OFDM for lower constellation order. On the other hand for higher value of M i.e. ($M \leq 256$ for ACO-OFDM or $M \geq 64$ for DCO-OFDM) DCO-OFDM outperforms ACO-OFDM.

However, the un-modulated even ACO-OFDM subcarriers and their antisymmetric time domain characteristics have been investigated in [142], [143] and, [144] in order to enhance its system performance. A trade off solution between ACO-OFDM and DC-OFDM is presented in [142] as only the odd subcarriers are demodulated traditionally in ACO-OFDM while the even subcarriers are modulated in DCO-OFDM. In this work, both schemes are combined and transmitted simultaneously where the interference cancelation method is used at the Rx to separate them. Moreover, the combination of PAM-DMT and ACO-OFDM is proposed in [143] where the odd subcarriers are used by ACO-OFDM while the even subcarriers are used by PAM-DMT.

In this scheme, the PAM-DMT is inverted before being combined with ACO-OFDM in order to support dimming control where the linear LED dynamic range is utilised by the

56

asymmetrical combination resultant signal. Furthermore, a hybrid OOK and ACO-OFDM methodology is introduced in [144] to increase the spectral efficiency of ACO-OFDM. In this approach, the antisymmetric ACO-OFDM time domain signal is investigated where the negative ACO-OFDM signals are clipped as in traditional ACO-OFDM to modulate the 'off' case in OOK while the 'on' case of OOK is modulated by clipping the positive ACO-OFDM time domain signal and adding DC-biased current. However, all these aforementioned hybrid ACO-OFDM approaches are computationally involved and it difficult to support multiple services with different qualities of service (QoS) [14].

3.3.3 PAM-DMT

PAM-DMT is another unipolar optical OFDM method that been proposed in [133] in order to meet the IM/DD requirements without adding a DC-bias. However, unlike the ACO-OFDM scheme that uses a complex symbol (M-QAM) and only modulate the odd subcarriers; in PAM-DMT, only the imaginary part of M-QAM is modulated for both even and odd subcarriers (see Figure 3.14), before being processed by HS and IFFT operations in order to produce a real antisymmetric time domain signal.
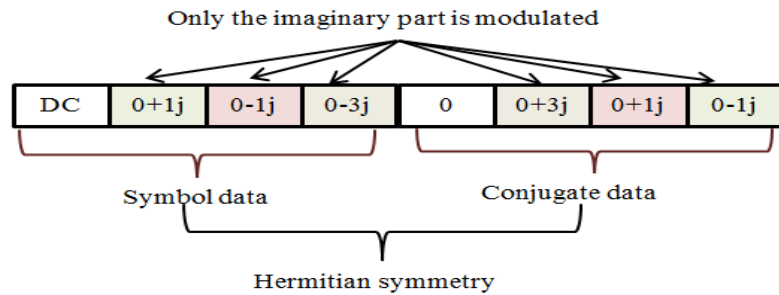
Figure 3.14. The implementation of real modulation and HS of PAM-DMT

However, in [145], it is proved that clipping the negative antisymmetric samples in PAM-DMT do not cause any distortion in the information since clipping noise only affects the unmodulated real part. Consequently, PAM-DMT and ACO-OFDM have the same spectral efficiency and optical power efficiency because only the odd subcarrier is used in ACO-OFDM while only the imaginary part is modulated in PAM-DMT. PAM-DMT outperforms

ACO-OFDM when bit and power loading method is considered since all the subcarriers of PAM-DMT are modulated. However, the un-modulated even subcarriers make the ACO-OFDM more attractive than PAM-DMT when these subcarriers are exploited to improve its performance [14].

3.3.4 ACO-SCFDE

ACO-SCFDE is an attractive modulation scheme that has been introduced in [23] to reduce the ACO-OFDM PAPR. The transceiver block diagram of this technique is illustrated in Figure 3.15. From this figure, one can see that the only difference between this scheme and the ACO-OFDM approach is the fact that the additional FFT and IFFT blocks are inserted before the odd modulation and parallel to serial (P/S) blocks at the Tx and the Rx respectively as denoted by the red rectangles in the figure. Inserting the FFT block before odd modulation and IFFT blocks results in achieved a SC-FDMA (i.e. IFDMA) scheme that has as low PAPR as SCM (chapter 2, subsection 2.6).

However, the requirement of HS implementation before IFFT block in ACO-SCFDE makes the PAPR of this scheme higher than that of IFDMA since only half the subcarriers enjoy the mapping feature, unlike IFDMA where the mapping feature is achieved for all subcarriers. Nevertheless, ACO-SCFDE has a lower PAPR than ACO-OFDM which make it an attractive candidate scheme for IM/DD based VLC system [23].
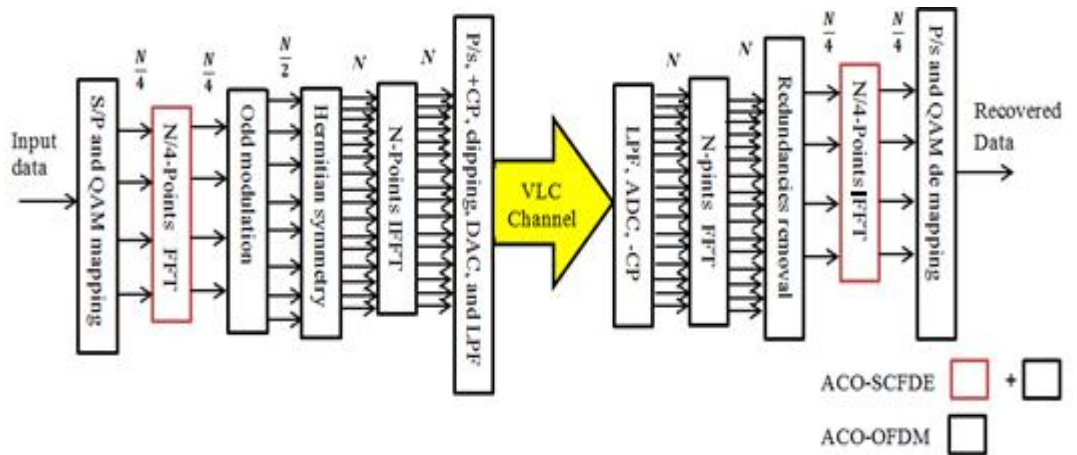
Figure 3.15. A block diagram of ACO-SCFDE transceiver

3.4 Summary

In this chapter, an overview of the VLC system including VLC applications, LEDs principles with an emphasis on modulation bandwidth, PDs suitable for VLC links, VLC indoor channel modelling and the VLC challenges was outlined.

The limited bandwidth of LEDs was highlighted in this Chapter as the major VLC bottleneck, and complex modulation schemes such as OFDM with blue filter and the equalization techniques were introduced as attractive solutions that can overcome the LED bandwidth issue. However, the blue filter and the equalization techniques were proposed at the cost of SNR. On the other hand, the complex and bipolar RF-OFDM signal was modified to be suitable for IM/DD based VLC systems at the cost of optical power efficiency (i.e. DCO-OFDM), or at the cost of half of the available bandwidth (i.e. ACO-OFDM and PAM-FDM).

Finally, due to the limited LED dynamic range and because of the OFDM's high PAPR, IFDMA was introduced as an attractive alternative complex modulation scheme after being modified to meet the IM/DD requirements.

CHAPTER 4

PILOT-AIDED ACO-OFDM

AND POSITION-ENCODED ACO-

OFDM SCHEMES

4.1 Introduction

As already discussed in Section 3.3 of Chapter 3, OFDM signals should be modified if they are going to be used for IM of LEDs. However, these adaptations in ACO-OFDM and DCO-OFDM are achieved by sacrificing 3/4 and 1/2 of the electrical spectral efficiency respectively. Furthermore, in the case of DCO-OFDM an additional cost of increased power consumption is also paid, which can make DCO-OFDM undesirable for some VLC-based applications where power consumption efficiency is a crucial requirement [10, 14]. Two new unipolar OFDM schemes known as pilot aided ACO-OFDM (PA-ACO-OFDM) and position-encoded ACO-OFDM (PE-ACO-OFDM) are proposed in this chapter.

These schemes offer increased R_b compared to ACO-OFDM through exploiting the anti-symmetric (i.e. asymmetric) ACO-OFDM time domain signal characteristics, where only the first half of the ACO-OFDM signal is used to transmit the ACO-OFDM data symbols, while the second half is removed. However, compared to DCO-OFDM, both of the proposed schemes offer less optical power consumption, as they do not require any additional DC-bias to make the time domain signal positive.

To meet the IM/DD requirements, the negative samples (NSs) of the first ACO-OFDM half are inverted to positive ones at the cost of inserting high amplitude pilots known as pilot chips (PCs) as in PA-ACO-OFDM or at a cost of additional encoded ACO-OFDM samples as in PE-ACO-OFDM. These PCs and the encoded ACO-OFDM samples are used at PA-ACO-OFDM and PE-ACO-OFDM Rxs respectively to detect and recover the inverted negative samples, thus allowing complete recovery of the OFDM symbols.

However, the insertion of high amplitude PCs in PA-ACO-OFDM may cause a reduction in transmit power as LEDs have limited dynamic range and a certain level of scaling between data samples and PCs might be needed. In PE-ACO-OFDM, in order to have R_b higher than ACO-OFDM, a reduction in the number of the encoded samples is needed and as a result a high encoded constellation order (i.e., > 16-QAM) is required. As such, PA-ACO-OFDM is proposed to increase the R_b of ACO-OFDM in some applications where low SNR is needed, while PE-ACO-OFDM is suggested to enhance the R_b of ACO-OFDM in the case of high SNR requirements. In addition, the insertion of PCs in PA-ACO-OFDM can be utilized for illumination and dimming control as well as channel estimation, equalization and modulation rate adjustment in VLCs.

The structure of the chapter is as follows; A discussion of the PA-ACO-OFDM scheme including PA-ACO-OFDM system description, the signal analysis of PA-ACO-OFDM, and PA-ACO-OFDM simulation results are presented in Section 4.2. Discussion on PE-ACO-OFDM including the PE-ACO-OFDM system module and its R_b, the orthogonality of PE-ACO-OFDM and its power consumption, and simulation results are presented in Section 4.3. Finally, the summary of this chapter is outlined in Section 4.4.

4.2 Pilot-Aided ACO-OFDM (PA-ACO-OFDM)

The PA-ACO-OFDM singling scheme for IM/DD-based VLCs is presented in this section where the anti-symmetry nature of the time-domain ACO-OFDM signal is utilized to increase the data rate by up to 33%.

4.2.1 System description

This section gives a brief description of the proposed PA-ACO-OFDM system, including the structures of both Tx and Rx.

a) PA-ACO-OFDM Tx

Figure 4.1 illustrates a block diagram of the Tx for PA-ACO-OFDM. The structure of the Tx is similar to the standard ACO-OFDM Tx, with the main differences being the inclusion of anti-symmetric signals removal, pilot insertion (PI) and the negative inversion blocks.
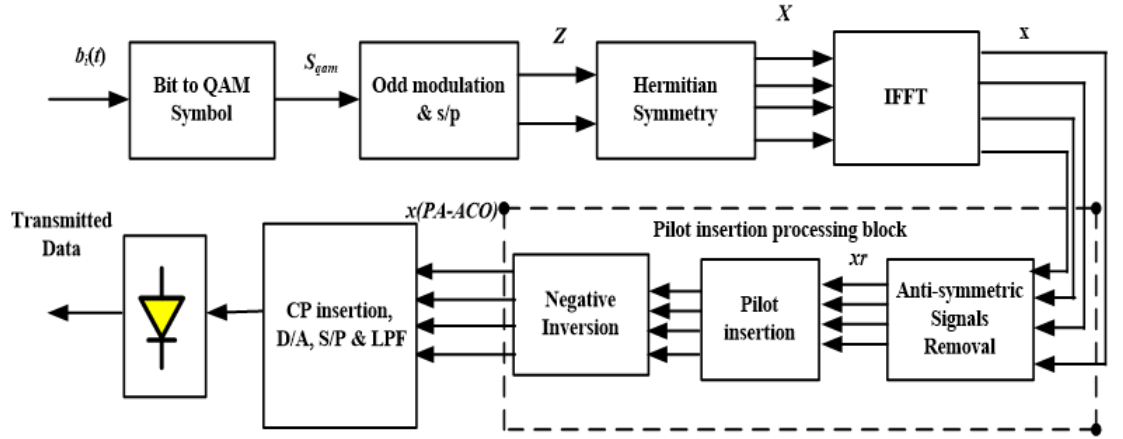
Figure 4.1. Block diagram of the pilot-aided ACO-OFDM Tx

The signal processing procedure can be described as follows: A sequence of input serial binary data stream $bi(t)$ ($bi \in \{1,0\}$) is mapped into a group of complex quadrature amplitude modulation symbols S_{QAM} according to the chosen modulation scheme (such as 4-, 8-, 16-, 32-…. and 1024-QAM). Similar to the standard ACO-OFDM in which only the odd subcarriers carry the data symbols to meet the requirement of non-negative time-domain signals, S_{QAM} are allocated to the odd subcarriers only and all symbols on the even subcarriers are set to zero.

The resulting signal Z is further processed to maintain HS as defined in [136]. As in all OFDM systems, the output of the HS process X is in the frequency-domain, which is converted back into the time domain by performing an IFFT operation. The OFDM symbol in the time domain x is indeed a sequence of samples. The odd modulation and HS process

are implemented prior to the IFFT to obtain an anti-symmetric and real time domain sequence of samples.

However, the anti-symmetry profile will result in redundant samples. This is because half of the samples in the time domain are repeated anti-symmetrically. It can be shown that only half of the available samples are indeed the information samples carrying *bi* (*t*), whereas the other half is 'repeated' in an anti-symmetric format. From the viewpoint of information, half of the available samples are redundant and 'wasted' in order to maintain the anti-symmetry profile for real non-negative IM. As a result, the efficiency of ACO-OFDM is considered to be quite low and its R_b is only half that of DCO-OFDM. Improving the bandwidth efficiency and throughput is the main motivation of this work. To achieve this, the PA-ACO-OFDM scheme is proposed by including a new pilot insertion processing (PIP) block between the IFFT and CP insertion blocks (see Figure 4.1).

The PIP block consists of three modules: (*i*) an anti-symmetric signal removal where the second part of *x* is removed with the resulting signal x_r having a shorter duration than the standard ACO-OFDM. Removing the second part of *x* does not lead to loss of information due to the anti-asymmetry and redundancy present in the ACO-OFDM symbol. In doing so, R_b can be increased since OFDM symbols are shorter and therefore more symbols can be transmitted over a given duration. (*ii*) PI-x_r is further processed to identify NSs. PCs are inserted to identify the location of NSs at the Rx. It worth noting that PCs are inserted before every negative sample provided that the number of NSs is less than the number of positive samples (PoSs), otherwise PCs are inserted before every positive sample.

Depending on the number of inverted samples, some PCs may be padded at the end of each sequence to ensure the same length as that of the symbol duration. One more sample is also inserted at the end of each OFDM sequence as an indicator to inform the Rx whether the PC is inserted before the positive or negative samples. (*iii*) Negative inversion - following the insertion of PCs, all NSs are inverted into PoSs with the same amplitude, which can be easily

identified at the Rx by checking the position of PCs. Therefore, at the Rx, the samples can be checked to see if they are inverted, which can then be inverted back to their actual format.

b)   PA-ACO-OFDM Rx

Figure 4.2 illustrates the block diagram of PA-ACO-OFDM Rx with the reverse functionality of the Tx, where the transmitted optical signal is convoluted with the impulse response of the VLC channel and converted to an electrical signal r (t) by the PD. The shot noise, modelled as AWGN (w_n) is added to r (t) and the resulting signal, $y(t) = r(t) + w_n(t)$ is passed through a LPF, an ADC and the CP removal module and yields a digital signal xd.

xd is applied to the pilot detector module to detect the presence of the inverted signal before converting them back to the negative format using the negative regenerator process.

Following the removal of PCs, the output of the pilot removal processing block xe is applied to the S/P converter, FFT process, zero forcing equalizer, de-mapping, and P/S converter module in order to regenerate the transmitted data.
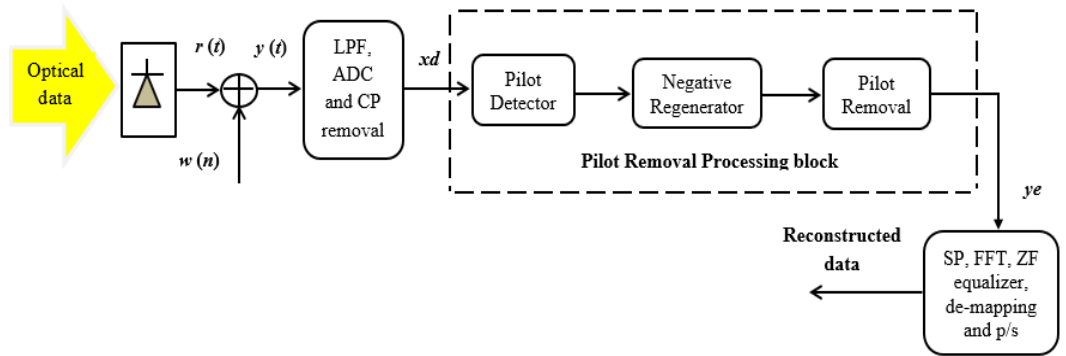
Figure 4.2. Block diagram of the pilot-aided ACO-OFDM Rx

4.2.2 Signal analysis of PA-ACO-OFDM

This section presents the details and procedure of the proposed pilot-aided algorithm to achieve an improved data rate performance compared to the existing ACO-OFDM system. The analysis of the anti-symmetric signals with PI shows that R_b can be increased by up to almost 33% compared to the traditional ACO-OFDM.

64

PA-ACO-OFDM system module

The proposed scheme is based on ACO-OFDM but with additional signal processing capabilities following the IFFT at the Tx, including anti-symmetric removal, PC insertion and negative inversion. The serial input bit stream $b_i(t)$ is converted into parallel data streams and mapped onto complex data symbols as given by [136, 140]:

$$S = [s_0, s_1, s_2, \dots s_{D-1}], \tag{4.1}$$

where D is the number of transmitted complex data symbols. Let N denote the number of points in the IFFT, which is equal to the total number of subcarriers. It is worth noting that, in contrast to OFDM in RF communications, ACO-OFDM requires four times more subcarriers than the number of data symbols [19]. Similar to ACO-OFDM, the relationship between D and N in the proposed PA-ACO-OFDM is given by:

$$D = \frac{N}{4}. \tag{4.2}$$

The complex symbols are mapped onto odd subcarriers by setting the even subcarriers to zero, which can be described by the complex vector as follows:

$$Z = [0, s_0, 0, s_1, 0, \dots, s_{D-1}], \tag{4.3}$$

where the size of $Z = N/2$. Z is processed by the HS block (see Figure. 4.1) so that the output of IFFT is a real signal suitable for optical transmission.

The HS processing is defined as [140] [134]:

$$X_i = \begin{cases} Z_i & i \leq N/2 - 1 \\ 0 & i = N/2, \\ Z^*_{N-i} & i \geq N/2 + 1 \end{cases}$$

$$X = [Z_0, Z_1, Z_2, Z_3, \dots, Z_{\left(\frac{N}{2} - 2\right)}, Z_{\left(\frac{N}{2} - 1\right)}, Z_{\left(\frac{N}{2}\right)}, Z_{\left(\frac{N}{2} + 1\right)}, Z_{\left(\frac{N}{2} + 2\right)} \dots Z_{(N-2)}, Z_{(N-1)}],$$

$$X = [0, Z_1, 0, Z_3, \dots 0, Z_{\left(\frac{N}{2} - 1\right)}, 0, Z_{\left(\frac{N}{2} - 1\right)}^*, 0, \dots, Z_3^*, 0, Z_1^*]. \tag{4.4}$$

X_i represents the symbol to be transmitted at the ith subcarrier ($i = 0, 1, \dots, N - 1$). The size of X is N, and $X \in \mathbb{C}^N$ (note that $\mathbb{C}^N$ denotes the set of N-dimensional complex numbers).

Since X is Hermitian symmetric and odd modulated, applying IFFT on X yields a real anti-symmetric time domain signal defined as [20] [140]:

$$x_k = \frac{1}{N} \sum_{i=0}^{N-1} X_i \ \exp(\frac{j2\pi ik}{N}), \qquad (5a)$$

$$x_k = \begin{cases} x_k & \text{for } 0 \le k \le \frac{N}{2} - 1 \\ -x_{k-\frac{N}{2}} & \text{for } \frac{N}{2} \le k < N - 1 \end{cases}, \qquad (5b)$$

where x_k, referred to as a sample with a constant duration of T_s, is the kth time domain sample of x $(k = 0,1,\dots,N-1)$. Furthermore, $x \in \mathbb{R}^N$ and $\mathbb{R}^N$ denotes a set of N-dimensional real numbers. Therefore, the total number of samples in ACO-OFDM is N. Figure 4.3 below depicts the anti-symmetric time domain signal for the existing ACO-OFDM as described in equation (5b). For example for N=32, the sample 0 is anti-symmetric with sample 16, sample 2 is anti-symmetric with sample 17 and so on.

From the viewpoint of information redundancy, these samples convey the same but inverted information (i.e., redundancy), which translates to a waste of bandwidth (equivalently, part of the time duration of OFDM symbol is also wasted). It can be understood as half of the ACO-OFDM samples are used to transmit the information data and the other half are the overhead samples for maintaining the anti-symmetric features.
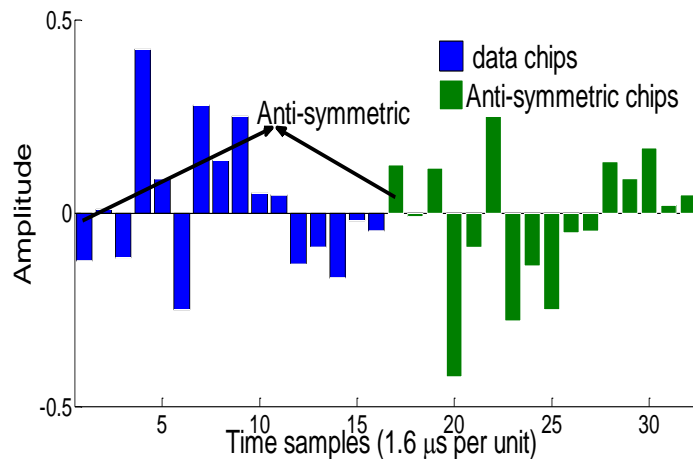
Figure 4.3. A plot of the anti-symmetric time domain signals for ACO-OFDM

Different to the traditional ACO-OFDM, the proposed scheme includes additional modules of anti-symmetric signal removal, PC insertion, negative inversion as shown in Figure 4.1, which are introduced to reduce the number of samples required for transmitting the same amount of data. It is shown that the redundant samples in the second half of the OFDM symbol can be removed without losing information content at the cost of inserting additional PCs to the sample sequence. The advantage of this is that the number of PCs in PA-ACO-OFDM is half the number of the redundant samples in ACO-OFDM.

In the proposed scheme, the IFFT output is passed through the anti-symmetric removal module (see Figure 4.4) and the output of the anti-symmetric removal module is given as:

$$xr = [xr_0, xr_1, xr_2, \ldots \ldots, xr_{(\frac{N}{2}-1)}]. \tag{4.6}$$
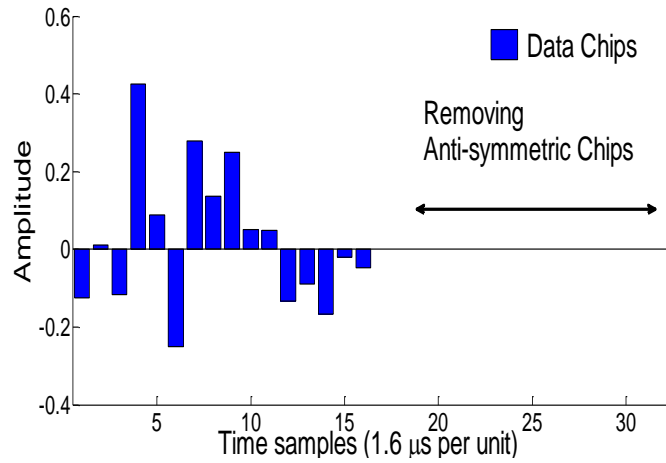
Figure 4.4. Signals in the time domain for ACO-OFDM after anti-symmetric removal process

Once all redundant samples in the second half of the IFFT output sequence are removed, PCs with higher amplitude are inserted into the sequence xr at some locations. Subsequently, the negative inversion process module inverts the negative samples to positive. This is to meet the non-negative signal transmission requirement in optical communications (see Figure 4.5).

The PCs are used by the Rx to identify if the received samples were inverted at the Tx. However, in order to reduce the number of inserted PCs, we first need to determine the

number of NSs. If the number of NSs is less than half of the total number of samples (i.e., there are less NSs than PoSs), then PCs are inserted before every negative sample. On the other hand, if the number of NSs is greater than the number of PoS, then PCs are inserted before every positive sample. As a result, the number of PCs are maintained to less than or equal to $N/4$. Since the number of PoSs and NSs are different for different OFDM symbols, in order to keep the length of every OFDM symbol fixed, a number of PCs are padded at the end of sample sequences. Furthermore, a special PC (SPC) is inserted at the end of the sequence to let the receiver know if the PCs are inserted before PoSs or before NSs (i.e.

$$SPC = \begin{cases} \text{pc} & if \quad \text{PoSs} \geq \text{NSs} \\ 0 & otherwise \end{cases}).$$

Note that, in ACO-OFDM, the number of total samples is N. Therefore, the total number of samples in the proposed PA-ACO-OFDM scheme is fixed and equal to $3/4N$.
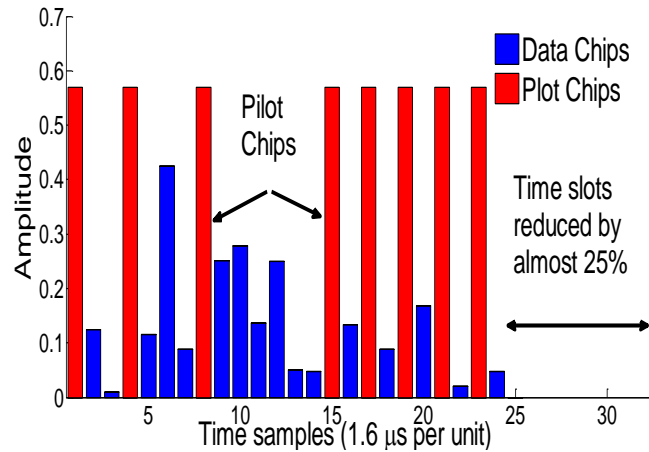
Figure 4.5. Pilot chips insertion

Selecting the pilot's amplitude

The normal distributions with mean μ and standard deviation σ of the probability density x for a range of QAM–ACO-OFDM schemes are shown in Figure 4.6.

Based on a confidence interval A_d of 99.8 %, the amplitude of data samples is below A_d which is given by:

$$A_d = \mu + 3\,\sigma. \tag{4.7}$$

At the Rx, in order to be able to detect the PC from the rest of the data samples and remove it prior to FFT, we have assigned PCs with amplitudes higher than A_d (i.e., 99.8 % of the amplitude of data samples). Considering AWGN noise, the amplitude of PC is expressed by:

$$A_p = \alpha A_d , \tag{4.8}$$

where the coefficients $\alpha > 1$. Of course, noise will affect amplitudes of data samples and PCs. At the Rx, to detect the PC from the rest of the data samples and remove it prior to FFT, we have adopted the threshold detection scheme with a threshold level defined as:

$$A_t = \beta A_d , \tag{4.9}$$

where ($\alpha > \beta > 1$). Both coefficients (α and β) are related to the noise power as will be later shown in subsection 4.2.3. Note that, at the Rx, all samples above A_t are considered as PCs.
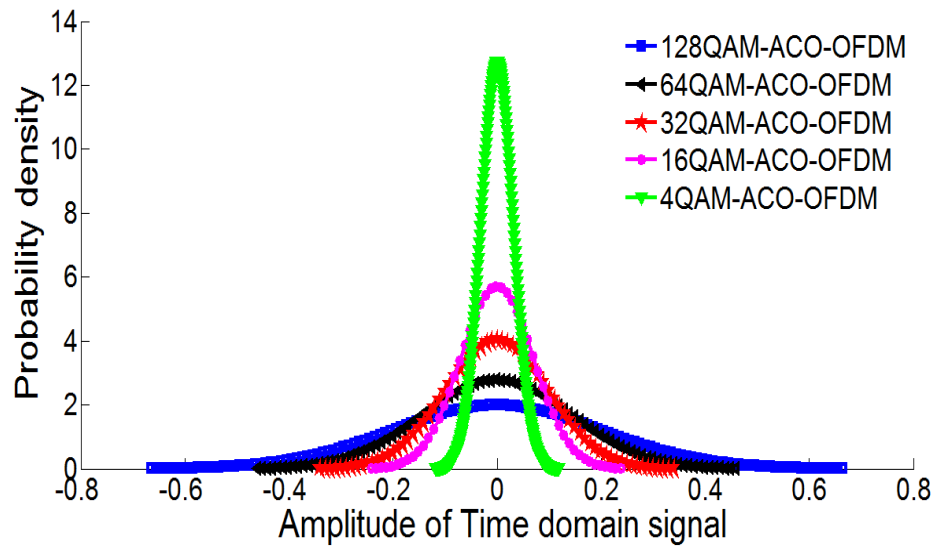
Figure 4.6. Normal distribution function for different QAM data symbols of x

The confidence intervals for 4-, 16-, 32-, 64-, and 128-QAM are presented in Table 4.1. Since the PAPR is proportional to the number of subcarriers [15], we have only shown A_d for $N = 1024$.

Table 4.1 The confidence interval values for a range of QAM orders.

QAM order	4	16	32	64	128
Confidence interval A_d	0.0935	0.2096	0.29	0.43	0.6

PA-ACO-OFDM data rates

Due to the anti-symmetric samples removal, the number of data samples in the proposed scheme is $N/2$, which is half of the data samples in the traditional ACO-OFDM (see Figure. 4.4). Therefore the total number of samples required to transmit D-data symbols in the proposed PA-ACO-OFDM is given by:

$$N_{PA} = \frac{1}{2}N + N_{PC\,1} + N_{PC2} + N_{PC3}, \tag{4.10}$$

where N_{PC1} is the number of PCs inserted prior to the inversion process and N_{PC2} is the number of padding PCs to ensure that the frame length is fixed to $3/4 \cdot (N.Ts)$. N_{PC3} represent the number of samples inserted at the end of the sequence which are used to let the receiver know if the PCs are inserted before the NSs or before the PoSs. Without loss of generality, we can use only one PC for N_{PC3}, that is $N_{PC3} = 1$. In general, the data rate of OFDM without CP is given by [134]:

$$R_{b(ofdm)} = \frac{1}{N} DBL, \tag{4.11}$$

where N is the number of samples per OFDM symbol, B is the available bandwidth, $L = \log_2 M$ where M is the data constellation order and D is the number of modulated subcarriers which is the same number of the transmitted data symbol (note that because of the odd modulation and HS requirements, the length of D in ACO-OFDM and PA-ACO-OFDM is $N/4$). Therefore, R_b of ACO-OFDM and PA-ACO-OFDM can be respectively given by:

$$R_{b(ACO)} = \frac{1}{N} \, D\,B\,L \tag{4.12}$$

$$R_{b(PA-ACO)} = \frac{4}{3N} \, D\,B\,L \tag{4.13}$$

Thus;

$$R_{b(PA-ACO)} \simeq 1.33 R_{ACO} \tag{4.14}$$

From equation (4.14), it can be clearly seen that R_b offered by the proposed PA-ACO-OFDM scheme is higher by 33% compared to the traditional ACO-OFDM. However, the achievable R_b for ACO-OFDM, PA-ACO-OFDM for 4-, 16-, 32-, 64- and 128-QAM are shown in Table 4.2 where B and D in Equations (4.12) and (4.13) are assumed to be 20 MHz and 256 subcarriers respectively.

Table 4.2 Data rates for ACO-OFDM and PA-ACO-OFDM for a range of QAM.

Data rates R_b (M bit/s)					
QAM	4	16	32	64	128
ACO-OFDM	10	20	25	30	35
PA-ACO-OFDM	13.33	26.66	33.33	39.99	46.66

4.2.3 PA-ACO-OFDM simulation results

In this subsection simulation results of the PA-ACO-OFDM scheme are presented.

A 20 MHz LED bandwidth, 1024-IFFT points, and the CP duration were assumed 50 ns (equal to the indoor duration of the VLC delay spread [146]). To analyse the effect of the channel, the impulse response of the indoor VLC channel for $0 \leq \psi \leq \Psi c$ was calculated and simulated as follows (4.15) [6] :

$$h(t) = \frac{(m+1)A}{2\pi d^2} \cos^m (\emptyset) \, T_s(\psi) \, g(\psi) \, cos(\Psi), \qquad (4.15)$$

where ψ and Ψc are the light ray reception angle and the maximum FOV respectively, A is the PD active area, m is the Lambertian emission, which is expressed as $m = \frac{-\ln(2)}{cos(\theta_{1/2})}, \theta_{1/2}$ is the LED semi-angle at half luminance, $\emptyset$ is the incidence angle, $T_s(\psi)$ is the optical filter gain, $g(\psi)$ is the gain of an optical concentrator, and Ψ is the irradiance angle.

Because the symbol duration of both schemes (i.e. ACO-OFDM and PA-ACO-OFDM) is greater than the duration of the delay spread of the indoor VLC channel (see Table 4.3), and the CP insertion, a flat fading channel was assumed in these simulation results (i.e. only a LOS path was considered).

Table 4.3 lists all the key parameters adopted in the simulation of the proposed PA-ACO-OFDM.

Table 4.3 PA-ACO-OFDM simulation parameter.

Parameter	Value
Room size	$5 \times 5 \times 3$ m^3
Source location (x, y, z)	$(2.5 \times 2.5 \times 3)$
LED bandwidth	20 MHz
LED half power angle $\emptyset_{1/2}$	70^0
Receiver location (x, y, z)	(2, 2, 0.5)
PD responsivity	1
Detector area A	16 mm^2
Receiver field of view (FOV) (full)	180^0
optical concentrator gain $g(\psi)$	0 dB
optical filter gain $T_s(\psi)$	0 dB
IFFT length	1024
Number of frames	100000
Modulation type and order	4, 16, 32, 64, 256, 1024 QAM
Subcarrier spacing	≈ 19.53 kHz
ACO-OFDM symbol duration	51.25 µs
PA- ACO-OFDM symbol duration	≈ 38.45 µs
Cyclic prefix duration	50 ns

To determine the best values for α and β we have simulated the BER performance of the proposed PA-ACO-OFDM scheme for a range of SNR values as shown in Figure 4.7. As can be seen from Figure 4.7, the BER performance improves with increasing values of α and β until reaching noise floor levels where there is no further improvement for $\alpha \gg \alpha_{op}$ and $\beta \gg \beta_{op}$ where α_{op} and β_{op} are the optimal values of α and β, respectively. The best and worst BER performance is achieved for SNR values of 16 dB and 4 dB, respectively. The optimum values of α and β are within the ranges of $2.5 < \alpha_{op} < 2.6$ and $1.75 < \beta_{op} < 1.95$, where the BER noise floors are observed.
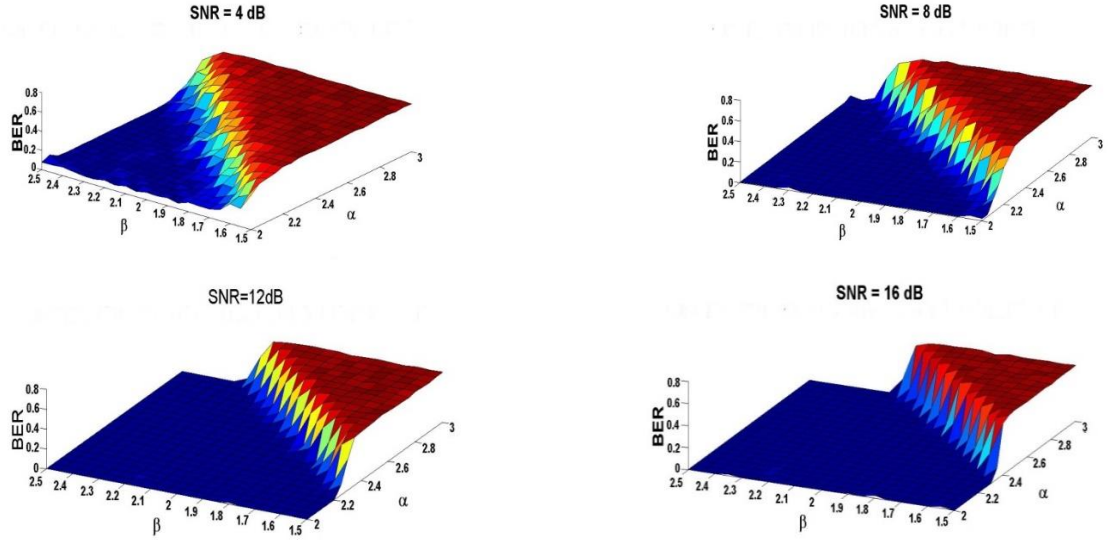
Figure 4.7. BER against α and β for a range of SNR for 4QAM-PA-ACO-OFDM

Next, we set $\beta = 1.85$ and investigate the BER performance against SNR for α_{op} of 2.7, 2.45 and 2.35 obtained from Figure 4.7 as shown in Figure. 4.8 also depicted for comparison is the BER performance for the standard 4-QAM ACO-OFDM with no PC. As can be seen, the proposed PA-ACO-OFDM with α_{op} of 2.7 displays a similar performance to ACO-OFDM. For $\alpha_{op} = 2.45$, the BER performance is the same as the traditional ACO-OFDM for SNR $\geq$ 8 dB. Finally, for $\alpha_{op} = 2.35$, the BER performance of the PA-ACO-OFDM is inferior to that of the ACO-OFDM for SNR < 12 dB. This is because of the increased probability of the false alarm associated with the detection of PC. The same values of α_{op} were also used in higher order QAM including 1024-IFFT points ACO-OFDM for $\beta = 1.85$ and the BER results obtained confirmed that an α_{op} value of 2.7 should be adopted for all values of SNR.
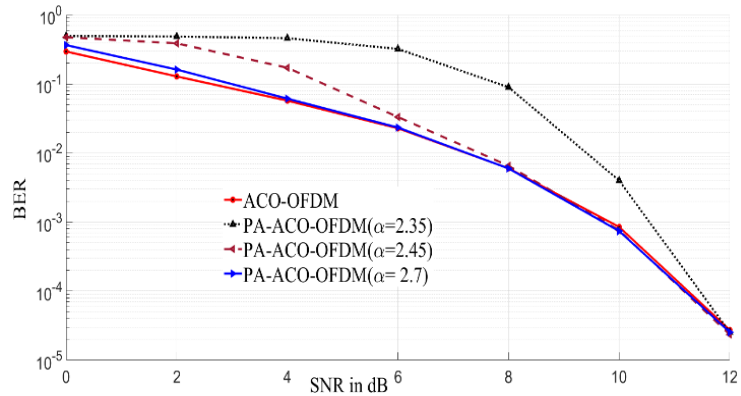
Figure. 4.8 BER vs. SNR for 4-QAM ACO-OFDM and PA-ACO-OFDM with different values of α

73

The simulation results for data throughput as a function of SNR for ACO-OFDM and PA-ACO-OFDM systems are illustrated in Figure 4.9 for a 4-QAM. To determine the link throughput, the received corrected bits are divided by the length of each OFDM symbol for a range of SNR values. For both ACO-OFDM and PA-ACO-OFDM, the throughput reaches saturation levels at a SNR of ~6 dB. This is because the PCs were not taken into account in the SNR analysis. From Figure 4.9, it can be clearly observed that the throughput of the proposed PA-ACO-OFDM is higher by approximately 32% compared to ACO-OFDM. This is because the time slots that are used to transmit the same data are decreased by almost 25% when pilot-aided ACO-OFDM is implemented.
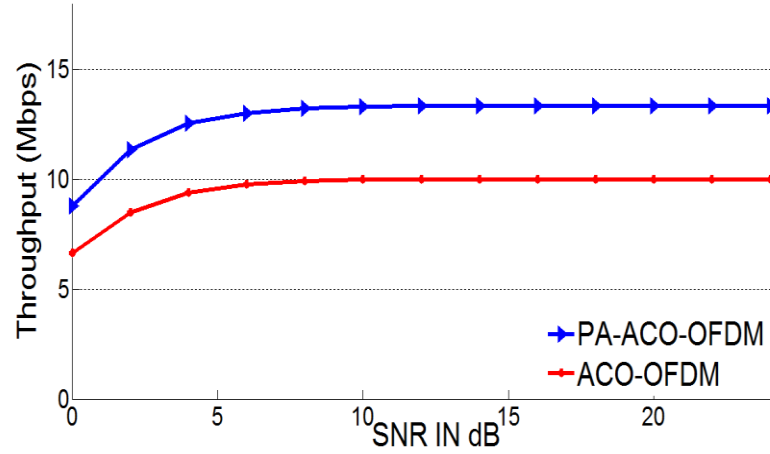
Figure. 4.9 Throughput VS SNR for 4-QAM ACO-OFDM and PA-ACO-OFDM

4.3 Position Encoded ACO-OFDM (PE-ACO-OFDM)

In this section, a new PE-ACO-OFDM signalling scheme is introduced for IM/DD-based VLCs to enhance the ACO-OFDM R_b by utilizing its anti-symmetric time domain characteristic. Theoretical and mathematical comparisons between ACO-OFDM and PE ACO-OFDM in terms of R_b are illustrated in this section and show that PE-ACO-OFDM outperforms ACO-OFDM only if a high encoded constellation order (i.e., > 16-QAM) is considered in PE-ACO-OFDM. Furthermore, a comparison between DCO-OFDM, ACO-OFDM and PE-ACO-OFDM schemes in terms of optical power requirements is also presented.

4.3.1 PE-ACO-OFDM system module

The system model of the proposed PE-ACO-OFDM is illustrated below where the structures of both the Tx and the Rx are depicted.

a) PE-ACO-OFDM Tx

Figure 4.10 depicts the block diagram of the PE-ACO-OFDM Tx. As in traditional ACO-OFDM, the serial binary bits bi ($bi \in \{0,1\}$) are passed through P/S, QAM mapping, odd modulation, HS and IFFT processes. As a result, the IFFT output signal (x) is an anti-symmetric real time domain signal (see Figure 4.11(a)) suitable for IM/DD, where $x = \{x_0, x_1, x_2, \dots\dots x_{N-1}\}$ and N is the number of samples in each ACO-OFDM symbol which is equal to the total number of subcarriers and the IFFT size. As already mentioned, the anti-symmetric characteristic of ACO-OFDM time domain signal enables it to outperform DCO-OFDM in terms of optical power consumption efficiency. On the other hand, the redundant anti-symmetric samples reduce the spectral efficiency of ACO-OFDM by half in comparison to DCO-OFDM.
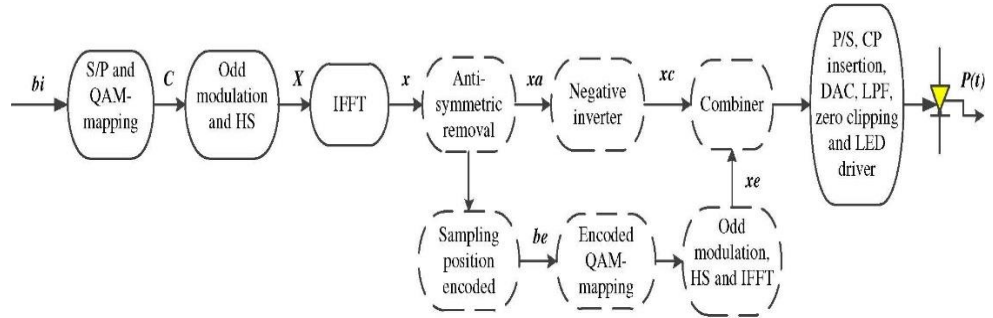
Figure 4.10. A block diagram of PE-ACO-OFDM Tx

To increase the spectral efficiency of ACO-OFDM, additional processes are added in this work (see dotted boxed in Figure 4.10) the function of which can be described as follows:

- The anti-symmetric samples of x are removed (see Figure 4.11(b)), hence, the number of samples in the resulting signal (xa) is $N/2$ ($xa = \{xa_0, xa_1, xa_2, \dots\dots xa_{N/2-1}\}$).

- *xa* is then fed to a sampling position-encoded process to encode the position of the negative and positive samples of *xa* such that; if $xa_m \leq 0$, 0 is inserted, otherwise 1 is inserted (see Figure 4.11(c)), where *m* is the mth ACO-OFDM sample of *xa*. As such, the resulting encoded binary bits ($be \in \{0,1\}$) has N/2 bits.

- *be* pass through encoded QAM-mapping, odd modulation, HS and IFFT processes. Thus, the resulting signal *xe* is a new ACO-OFDM signal (see Figure 4.11(e)) that has $2N/L_e$ number of samples where $L_e = \log_2 M_e$ and M_e is the encoded constellation order (i.e., 4, 8, 16, 32 … QAM). Finally, the negative samples of *x* are inverted (see Figure 4.11(d)) and combined with *xe* (see Figure 4.11(f)) before being passed through the P/S, CP insertion, DAC, LPF, zero clipping and electrical optical converter (EOC) processes.
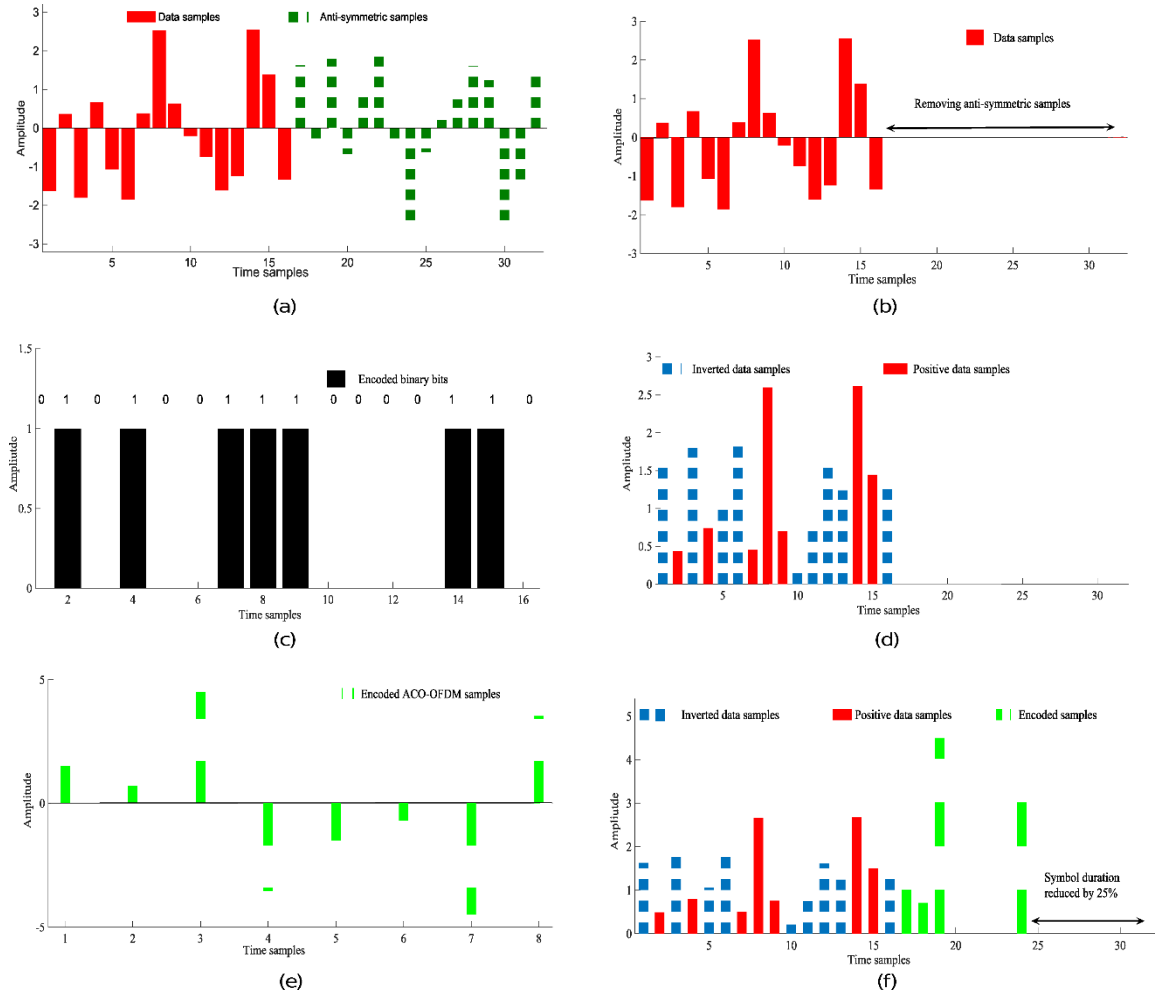
Figure 4.11 (a) the ACO-OFDM time domain signal *x*, (b) the ACO-OFDM time domain signal after anti-symmetric removal process *xa*, (c) the encoded negative and positive samples positions *be*, (d) *xa* after the negative samples inversion process *xc*, (e) the encoded ACO-OFDM signal *xe*, and (f) the combination of *xe* with *xc*. N=32, M=16-QAM and M_e =256-QAM

b) PE-ACO-OFDM Rx

Figure 4.12 depicts a block diagram of the PE-ACO-OFDM Rx, where the transmitted optical signal is convoluted with the impulse response of the VLC channel and added to the shot and terminal noises, which are modelled as an AWGN (w_n), after being converted to an electrical signal by the PD. Following ADC, LPF and CP removal, the resulting signal yc passes through a separator process block (see Figure 4.12). In this process, the received inverted data samples ya (i.e., xa added to the noise) is separated from the encoded data samples (ye) (i.e. xe added to the noise).

Subsequently, ye is fed to the ACO-OFDM demodulation block where the binary encoded bits ($br \in \{0,1\} = br_0, br_1, br_2 \dots \dots, br_{\frac{N}{2}-1}$) are reconstructed. Then, the inverted negative samples of ya are returned to their negative values depending on the binary value of br. As such, the resulting bipolar samples victor ($yaco$) can be defined as:

$$yaco_J = \begin{cases} ya_J & \text{if } br_J = 0 \\ -ya_J & \text{if } br_J = 1 \end{cases}, \tag{4.16}$$

where $J = \{0,1,2,3,\dots\dots,\frac{N}{2} - 1\}$ Finally, the transmitted data bits are reconstructed traditionally by passing y_{aco} to the ACO-OFDM demodulation block
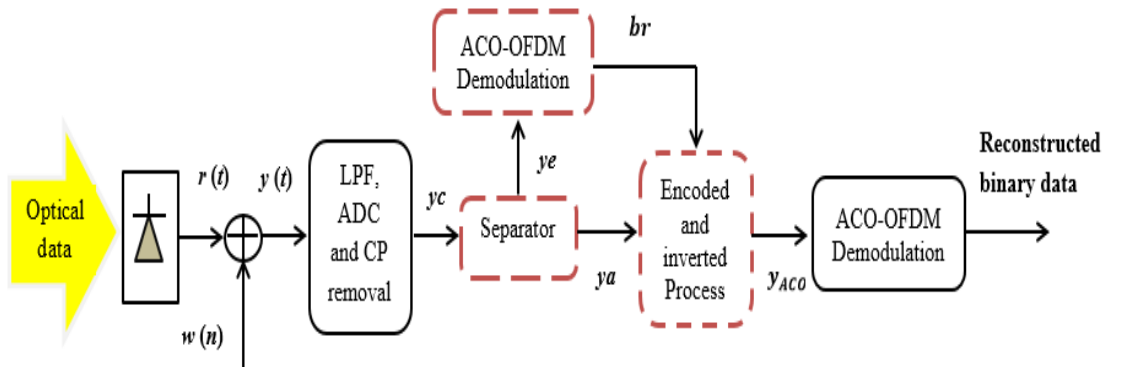
Figure 4.12. A block diagram of the PE-ACO-OFDM Rx

4.3.2 PE-ACO-OFDM data rates

After the anti-symmetric removal and the negative inversion processes, *xa* has $N/2$ samples (see Figure 4.11 (b)). However, because of the requirements of the additional encoding processes in this work (see Figure 4.10), *xa* is combined with *xe* (see Figure 4.11 (f)). Thus, the total number of samples in PE-ACO-OFDM (N_{PE}) that are required to transmit the same ACO-OFDM data symbol is given by:

$$N_{PE} = \frac{N}{2} + \frac{2N}{L_e}.$$

$$= \frac{(4 + L_e)N}{2L_e}.$$

(4.17)

Table 4.4 illustrates the required N_{PE} to transmit the same ACO-OFDM data symbol for different QAM encoding.

Table 4.4 Required N_{PE} for a range of L_e.

L_e	Required N_{PE}
2	1.5 N
4	N
5	0.9 N
6	0.83 N
7	0.78N
8	0.75N
9	0.723 N
10	0.7N

From equation (4.17) and Table 4.4, it can be clearly observed that:

$$N_{PE} = \begin{cases} \leq N \ for \ L_e \geq 4 \\ \geq N \ for \ L_e \leq 4 \end{cases}.$$

(4.18)

Regarding equation (4.11), the data rates of PE-ACO-OFDM can be expressed by:

$$R_{b(PE-ACO)} = \frac{1}{N_{PE}} \ DB \ L.$$

78

$$= \frac{2L_e}{(4 + L_e)N} \, D \, B \, L .$$ (4.19)

From equation (4.19), it can be seen that $R_{b(PE-ACO)}$ increases as L_e increases. In addition, $R_{b(PE-ACO)} \gg R_{b(ACO)}$ for $L_e \gg 4$ (see Equation (4.12)). The percentage increase in R_b ($R_d^{\{inc\}}$) as a function of Le for the PE-ACO-OFDM scheme when compared with the traditional ACO-OFDM is illustrated in Figure 4.13.
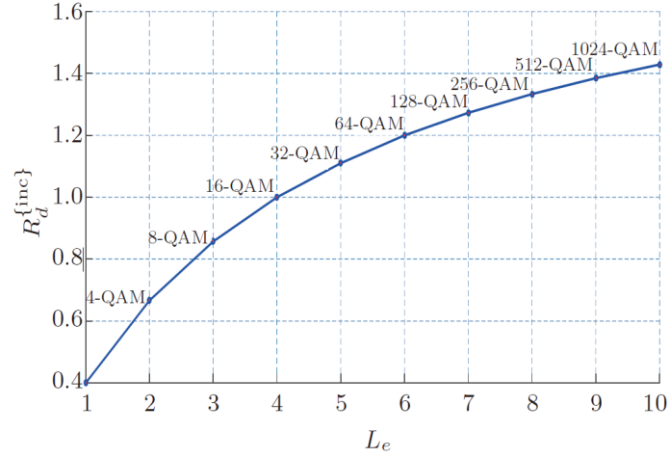
Figure 4.13. Percentage increase in the data rate vs. L_e., for PE-ACO-OFDM relative to ACO-OFDM.

4.3.3 The orthogonality of PE-ACO-OFDM

The orthogonality of the proposed PE-ACO-OFDM signal is mathematically established here by showing how the ACO-OFDM signal remains orthogonal after removing its second half. Referring to Figure 4.10, the output of the IFFT is an ACO-OFDM signal x described as:

$$x_k = \frac{1}{N} \sum_{i=0}^{N-1} X_i \, \exp\frac{j2\pi ik}{N}$$ (4.20)

where k is the kth ACO-OFDM sample in the time domain and i is the ith ACO-OFDM subcarrier in frequency domain which is given as $k = i = \{0,1,2,3 \dots \dots N-1\}$. After removing the second part of the ACO-OFDM, the resulting signal xa can be described by:

$xa = \{xa_0, xa_1, xa_2, \dots \dots xa_{Z-1}\}$ where $Z = \frac{N}{2}$. However, xa is an orthogonal signal if the

79

integration of the products of its frequency domain signal (XD) is zero [15], which can be proved through:

$$XD_n = \sum_{m=0}^{Z-1} X_m \exp \frac{-j2\pi nm}{Z}. \qquad (4.21)$$

where $n = \{0,1,2,3,4,\ldots .Z-1\}$. Then, the integration of the products of XD can be expressed as:

$$\sum_{n=0}^{Z-1} XD_n = \sum_{m=0}^{Z-1} X_m \sum_{n=0}^{Z-1} exp \frac{-j2\pi nm}{Z}.$$

$$= \sum_{m=0}^{Z-1} X_m \sum_{n=0}^{Z-1} exp \left(\frac{-j2\pi m}{Z}\right)^n$$

$$= \sum_{m=0}^{Z-1} X_m \frac{1 - \left(e^{\frac{-j2\pi m}{Z}}\right)^Z}{1 - e^{\frac{-j2\pi m}{Z}}} \qquad (4.22)$$

$$= \sum_{m=0}^{Z-1} X_m \frac{1 - e^{-j2\pi m}}{1 - e^{\frac{-j2\pi m}{Z}}}$$

$$= 0 \ \text{for } m = 0,1,2,3,4\ldots, Z\text{-}1$$

4.3.4 Power consumption

Since the main advantage of ACO-OFDM in comparison to DCO-OFDM is its power consumption efficiency, a comparison between DCO-OFDM, ACO-OFDM and PE-ACO-OFDM in terms of optical power consumption is made in this subsection. In LED-based VLCs, the average transmit optical power P_T for DCO-OFDM, ACO-OFDM [136] and PE-ACO-OFDM are respectively given by:

$$P_{T-DC} = \frac{\sigma_D}{2\pi} \exp\left(\frac{-B_{DC}^2}{2\sigma_D^2}\right) + B_{DC}(1 - Q(\frac{B_{DC}}{\sigma_D})), \qquad (4.23)$$

$$P_{T-ACO} = \frac{1}{\sqrt{2\pi}F_T} \sum_{d=1}^{F_T} \sigma_{ACO} \qquad (4.24)$$

$$P_{T-PE-ACO} = \frac{1}{\sqrt{2\pi}F_T} \sum_{d=1}^{F_T} \sigma_{PE-ACO}, \qquad (4.25)$$

where F_T is total number of transmitted OFDM symbols within the test period (i.e., $d = 1, 2,... F_T$ and $F_T = 10000$), σ_D and σ_{ACO} are the standard deviations of the time domain signal for DCO-OFDM, and ACO-OFDM [136], and σ_{PE-ACO} is the slandered deviation of the time domain signal for PE-ACO-OFDM given by $\sigma_{Pe-ACO} = E\{x_{PE-ACO}^2\}$ (see Figure 4,10). In (4.23), $B_{DC} = \xi\sqrt{E\{x(t)^2\}}$ is the required DC bias level to ensure a non-negative OFDM signal, where ξ is the proportionality constant.

Table 4.5 compares P_T for transmitting a frame of DCO-OFDM, ACO-OFDM and PE-ACO-OFDM for 4-, 16-, 32-, 64, 128- and 256-QAM, where $\xi = 2$ as in [140] and the encoded constellation order is 256 QAM for PE-ACO-OFDM. From Table 4.5, it can be clearly seen that ACO-OFDM requires less P_T compared to DCO-OFDM and PE-ACO-OFDM for constellations up to 256-QAM. Also it can be observed that the required P_T for PE-ACO-OFDM is less than one for DCO-OFDM, so that for 256-QAM, DCO-OFDM requires P_T of almost 20 times more than is required for PE-ACO-OFDM. Note that since only the odd subcarriers are modulated in ACO-OFDM, DCO-OFDM has twice spectral efficiency compared to ACO-OFDM.

Table 4.5 Normalized optical transmission power P_T for a range of QAM.

Normalized transmitted optical power						
QAM	4	16	32	64	128	256
DCO-OFDM	0.0957	0.2139	0.3027	0.4384	0.6126	0.8823
ACO-OFDM	0.000385	0.0019	0.0039	0.0082	0.016	0.0331
PE-ACO-OFDM	0.0223	0.0234	0.0247	0.0275	0.0327	0.0442

4.3.5 PE-ACO-OFDM simulation results

Here we present our simulation results where the IFFT points are 512. Because of the HS and the odd modulation requirements for PE-ACO-OFDM and ACO-OFDM, only quarter of the available subcarriers are modulated.

However, due to the same reason and since the bit loading is not implemented in this simulation study, we only consider 256-QAM as an encoded constellation order (i.e., $L_e = 8$) for PE-ACO-OFDM. The indoor VLC channel is modelled as in subsection 4.2.3, where the impulse response of the VLC channel is calculated and simulated as in (4.15). All the parameters that were used in the simulation study are given in Table 4.6.

Table 4.6 PE-ACO-OFDM simulation parameter.

Parameter	Value
Room size	$5 \times 5 \times 3$ m^3
Source location (x, y, z)	$(2.5 \times 2.5 \times 3)$
LED bandwidth	20 MHz
LED half power angle $\emptyset_{1/2}$	70^0
Receiver location (x, y, z)	$(2, 2, 0.5)$
PD responsivity	1
Detector area A	16 mm^2
Receiver field of view (FOV) (full)	180^0
optical concentrator gain $g(\psi)$	0 dB
optical filter gain $T_s(\psi)$	0 dB
IFFT length	512
Number of frames	100000
Modulation type and order	256, 512 and, 1024 QAM for ACO-OFDM and only 256-QAM for PE-ACO-OFDM
Encoded modulation order	256 QAM
Cyclic prefix duration	50 ns [146]

Figure 4.14 depicts the results obtained for the BER as a function of the SNR for PE-ACO-OFDM and the traditional ACO-OFDM. Only 256-QAM is considered as data and encoded

constellation order for PE-ACO-OFDM while 256-, 512- and 1024-QAM are considered as data constellation orders for ACO-OFDM. From the figure, one can see that in order to achieve acceptable BER values (i.e. BER $= 10^{-3}$), the proposed PE-ACO-OFDM requires almost 30 dB SNR, while the requirements of SNR in the traditional ACO-OFDM to achieve the same BER value are found to be 29, 31.7 and 34.7 dB for 256-, 512- and 1024-QAM, respectively. The proposed PE-ACO-OFDM requires 1 dB SNR more than ACO-OFDM for the same constellation orders (i.e., 256-QAM) as any error in the negative inversion process at the PE-ACO-OFDM Rx can affects all PE-ACO-OFDM subcarriers at the frequency domain.
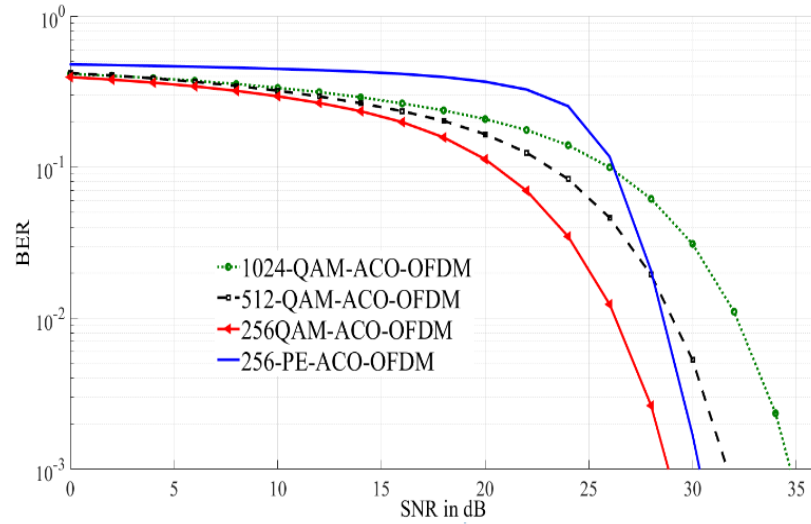
Figure 4.14. BER against SNR for PE-ACO-OFDM and ACO-OFDM for a range of QAM orders

Next, the data throughput against SNR for 256-QAM PE-ACO-OFDM and 256-, 512- and 1024-QAM ACO-OFDM were studied and are illustrated in Figure 4.15. In order to simulate the throughput link, only the received corrected bits are divided by every an OFDM symbol duration for a range of SNR values. From the figure, it can be observed that the throughput reaches saturation values at a SNR of approximately 29, 31, 34 and 30 dB for 256-, 512- and 1024-QAM ACO-OFDM and 256-QAM-PE-ACO-OFDM respectively. This is because higher constellation orders require higher SNR values for ACO-OFDM. However, as already mentioned, in order to provide accurate negative position detection, PE-ACO-OFDM

83

requires higher SNR in comparison to ACO-OFDM for the same constellation order. Furthermore, the figure also shows how the data throughput of 256-QAM PE-ACO-OFDM is higher by about 13.2, 8.2, and 3.2 Mbps compared to 256-, 512- and 1024-QAM ACO-OFDM respectively. This is due to the time symbol duration of PE-ACO-OFDM being reduced by 25% when 256-QAM is considered as an encoding constellation order.
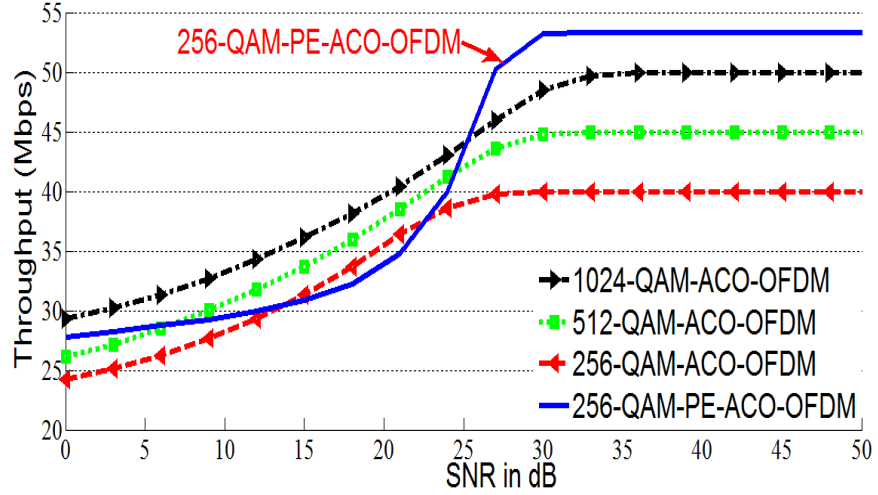
Figure 4.15. Throughput against SNR for 256-, 512- and 1024-QAM ACOO-OFDM and 256-QAM PE-ACO-OFDM

4.4 Summary

Two new unipolar OFDM schemes named as PA-ACO-OFDM and PE-ACO-OFDM were introduced and simulated in this chapter as means to increase R_b of ACO-OFDM by investigating its anti-symmetric time domain characteristics. This was achieved by transmitting the data samples using only the first half of the ACO-OFDM symbol while the second one was discarded. Because of the IM/DD requirements, the negative samples of the first half of ACO-OFDM were inverted and either PCs or encoded ACO-OFDM samples were inserted at the PA-ACO-OFDM Tx or at the PE-ACO-OFDM Tx respectively in order to allow the receiver to identify the positions of the inverted samples.

The simulation results of PA-ACO-OFDM were presented in subsection 4.2.3 and showed that the data rate of the PA-ACO-OFDM is increased by almost 33% compared to the

conventional ACO-OFDM. They also showed that the power efficiency and the BER performance of the PA-ACO-OFDM can be improved by varying the amplitude of the pilot chips.

In the PE-ACO-OFDM section, we showed how R_b of the PE-ACO-OFDM were enhanced in comparison to ACO-OFDM when a high encoded constellation order was considered. Furthermore, a comparison between PE-ACO-OFDM and DCO-OFDM in terms of the optical power consumption was given in this section and concluded that PE-ACO-OFDM requires much lower power in comparison to DCO-OFDM. However, DCO-OFDM offers twice R_b of ACO-OFDM since both odd and even subcarriers are utilized in this scheme. The simulation results of PE-ACO-OFDM were presented in subsection 4.3.5 and showed that R_b of PE-ACO-OFDM are improved by 33% in comparison to ACO-OFDM when 256-QAM is considered as an encoded constellation order. The simulation results in this subsection also demonstrated that the SNR of PE-ACO-OFDM is increased by nearly 1dB in comparison to ACO-OFDM. Finally, since LEDs work linearly only in a limited range, PA-ACO-OFDM was proposed only when a low SNR is required. On the other hand, since PE-ACO-OFDM requires high encoded constellation order to provide R_b higher than ACO-OFDM, PE-ACO-OFDM was recommended only when high SNR is achievable.

CHAPTER 5

THE UNIPOLAR-PAM-FDM

SCHEME

5.1 Introduction

As already discussed in subsections 3.2.3 and 3.3 of Chapter 3, LEDs used in VLC systems have a limited optical power-current linear range, which can affect the BER performance of the VLC system, as well as the dimming control feature when a high PAPR signal, such as an OFDM signal, is used in the VLC system. Implementing FFT and interleaving mapping before the implementation of IFFT at the OFDM Tx results in a new signal known as IFDMA. Such a signal has almost the same OFDM features as a low PAPR signal, such as an SCM signal (Chapter 2, subsection 2.3.4.2).

However, IFDMA is mainly proposed as a means to improve the OFDM PAPR signal in the RF domain, and has recently been modified to be suitable for IM/DD based VLC systems [23, 25, 135]. Due to the IM/DD requirements, all the modified IFDMA schemes have to implement HS between FFT and the interleaving mapping processes at the IFDMA Tx, which increases the PAPR values of these schemes in comparison to IFDMA in RF (Chapter 3, subsection 3.3.4).

In this chapter, the unipolar-pulse amplitude modulation frequency division multiplexing (U-PAM-FDM) singling scheme for IM/DD-based VLC systems is introduced as a means to improve the optical OFDM PAPR figures. This improvement is achieved by making IFDMA suitable for IM/DD without the implementation of HS by utilising PAM as a

modulation scheme, which results in the output FFT subcarriers at the IFDMA Tx being real and symmetrically conjugated, except the first and the middle subcarriers. However, to make all subcarriers symmetrically conjugated, two more new subcarriers are added at the middle and the end of the FFT output, where this process is known in this work as the symmetric conjugate (SCG) process. Implementing odd modulation and IFFT on these modified subcarriers results in a real and asymmetric signal suitable for IM/DD based VLC systems. This chapter presents simulation results showing how the PAPR value of the proposed scheme is improved in comparison with the traditional ACO-OFDM and ACO-SCFDE schemes. The impact of this improvement on the performance of VLC systems is illustrated by showing how the proposed scheme can offer more average transmitted power in comparison with the aforementioned schemes. Furthermore, an experimental study comparing the proposed scheme and the traditional ACO-OFDM scheme in terms of BER performance is presented in this chapter.

Note that, due to the limited time of this research, in the practical study, only 128 bits were randomly generated and used to implement the ACO-OFDM and U-PAM-FDM schemes. However, to improve the accuracy of these experimental results, higher number of bits (i.e., > 100,000) could be used in future works.

The chapter is structured as follows; a description of the U-PAM-FDM system is presented in Section 5.2, while the simulation and experimental results and their discussion are presented in Section 5.3. Finally, a summary of this chapter is provided in Section 5.4.

5.2 U-PAM-FDM System Description

In this section, the structures of the U-PAM-FDM Tx and U-PAM-FDM Rx are described in detail.

a) U-PAM-FDM Tx

Figure 5.1 depicts the block diagram of the U-PAM-FDM Tx, where an input random serial binary bit stream bi is firstly converted to parallel bits and mapped to the PAM.

The output of the aforementioned process is a real vector that can be expressed by: $C = \{C_0, C_1, C_2, C_3 \ldots \ldots C_{D-1}\}$, where D is the number of transmitted data symbols. C is then fed to the FFT block, where the output frequency domain signal, which is defined as:

$$S_m = \sum_{d=0}^{M-1} c_d\, e^{\frac{-j2\pi dm}{M}}, \tag{5.1}$$
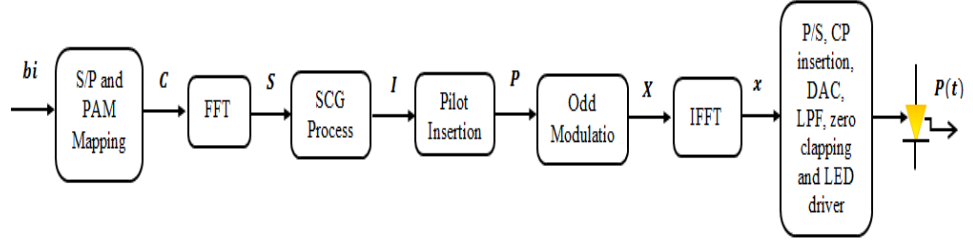
Figure 5.1. Block diagram of the U-PAM-FDM Tx

where $S = (S_0, S_1, S_2, \ldots \ldots S_{M-1})$, M is the FFT size which is equal to D, and m and d, are the mth subcarrier and d^{th} data symbol respectively. However, as the FFT inputs are real values (i.e., PAM), all FFT output subcarriers will be symmetrically conjugated around the $S_{\left(\frac{M}{2}+1\right)}$ subcarrier except the first one (S_0), as proved and illustrated below by Equation (5.2) and Figure (5.2), respectively.

$$S_m = \sum_{d=0}^{M-1} C_d\, e^{\frac{-j2\pi dm}{M}}$$

$$S_{M-m} = \sum_{d=0}^{M-1} C_d\, e^{-j\left(\frac{2\pi d}{M}\right)(M-m)}$$

$$= \sum_{d=0}^{M-1} C_d\, e^{-j\left(2\pi m - \frac{2\pi dm}{M}\right)}$$

$$= \sum_{d=0}^{M-1} C_d\, e^{\frac{j2\pi dm}{M}} \tag{5.2}$$

S_0	S_1	S_2	S_3	S_4	$S_3{}^*$	$S_2{}^*$	$S_1{}^*$

Figure 5.2 FFT output subcarriers for eight real input samples

From Equation (5.2) and Figure (5.2), it can be clearly observed that the mth subcarrier is conjugated with the $M - m^{th}$ subcarrier (i.e., $S_m = S^*{}_{M-m}$), since C consists of real values. However, in order to obtain an asymmetric real time domain signal suitable for IM/DD, all these subcarriers must be symmetrically conjugated (i.e., $S_m = S^*{}_{M-m+1}$) before being passed through the odd modulation and IFFT blocks. To do so, S is applied to the SCG block, where two additional subcarriers are added at this stage. The output vector (I) is given by Equation (5.3) and illustrated in Figure (5.3).

$$I = \{I_0, I_1, I_2, I_3, \ldots \ldots I_{Z-1}\}$$

$$I = \left\{ S_0, S_1, S_2, \ldots S_{\left(\frac{M}{2}-1\right)}, S_{\frac{M}{2}}, S_{\frac{M}{2}}, S_{\left(\frac{M}{2}+1\right)}, \ldots S_{M-1}, S_0 \right\} \tag{5.3}$$

Note that, $Z = M + 2$.

Two additional subcarriers

S_0	S_1	S_2	S_3	S_4	$S^*{}_4$	$S^*{}_3$	$S^*{}_2$	$S^*{}_1$	$S^*{}_0$
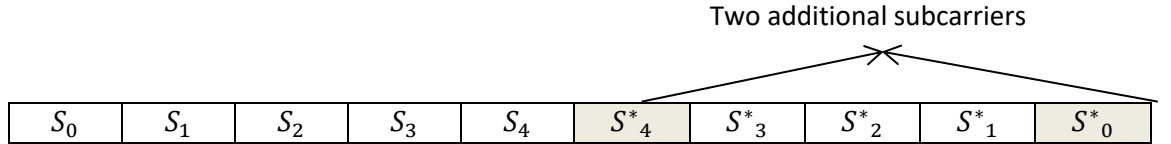
Figure 5.3 The frequency domain subcarriers after the SCG process, where $M = 8$ and $Z = 10$

For the purpose of channel estimation, I is fed to the pilot insertion block, where a number of symmetrically conjugate pilots are inserted as defined by Equation (5.4) and illustrated in Figure (5.4).

$$P = \{P_0, P_1, P_2, P_3, \ldots \ldots P_{V-1}\}, \tag{5.4}$$

P_0	I_0	I_1	I_2	P_1	I_3	I_4	I_5	I_6	P^*_1	I_7	I_8	I_9	P^*_0

Figure 5.4 The frequency domain subcarriers after the pilot insertion process, where Z=10, and A (the number of pilots)=4.

where $V = Z + A$ and, A is the number of pilots. Note that, the number of pilots depends on the channel characterization. P is subsequently passed through the odd modulation and IFFT processes, as described by Equations (5.5) and (5.6), respectively.

$$X = \{X_0, X_1, X_2 \ldots \ldots, X_{T-1}\},$$

$$= \{0, P_0, 0, P_1, 0, P_2 \ldots \ldots, 0, P_{Z-1}\} \tag{5.5}$$

$$x_n = \frac{1}{N} \sum_{k=0}^{N-1} X_k \, e^{\frac{2\pi nk}{N}} \tag{5.6}$$

where $T = 2V$, N is the number of IFFT points, and n and k are the nth time domain sample of x and the kth frequency domain subcarrier of X respectively. Note that, because of SCG and the odd modulation block, the IFFT signal is a real asymmetric signal (Chapter 3, subsection 3.3.2). Finally as in the traditional ACO-OFDM scheme, x passes through the P/S, CP insertion, DAC, LPF, zero clipping, and LED driver processes, before being converted to a light signal by the LED.

c) U-PAM-FDM Rx

Figure 5.5 shows the block diagram of the U-PAM-FDM Rx. Following optical detection, the received signal $y(t) = r(t) + w(t)$, where $r(t) = Rp(t) * h(t)$, R is the responsivity of the PD, $p(t)$ is the transmitted optical signal, $*$ denotes the linear convolution, $h(t)$ is the impulse response of the system, and $w(n)$ is the shot and terminal noises, which are modelled as AWGN. For the sake of simplicity and without loss of generality, the PD responsivity is assumed to be ideal (i.e., $R = 1$). $y(t)$ is then passed through the LPF, ADC, and CP removal processes, before being converted to a frequency domain signal (Y), by implementing an FFT.

Subsequently, the redundant subcarriers (i.e., even subcarriers) are removed from Y, and the resulting signal (YC) is fed to the pilots extraction block, where the received known pilot

symbols (YP) are separated from the received random data symbols (YD) and fed to the channel estimation block to estimate the system transfer function (H) (Chapter 2, subsection 2.3.4). Next, YD is applied to the equalizer block, where the effect of the system impulse response is abolished by implementing a one tap ZFE algorithm as given by:

$$YE = \frac{YD}{\widehat{H}} \tag{5.7}$$

Finally, the transmitted bits are reconstructed by passing YE through the IFFT and PAM de-mapping blocks.
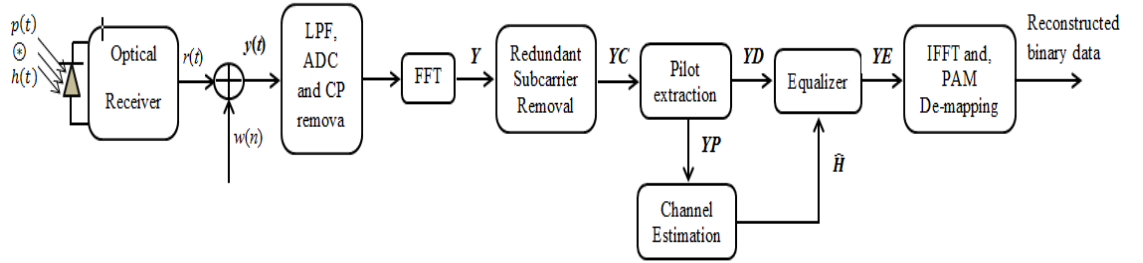
Figure 5.5. Block diagram of the U-PAM-FDM Rx

5.3 Results and analysis

In this section, the simulation and the practical results of the study investigating the performance of the U-PAM-FDM scheme are presented. In the simulations, the PAPR value of the proposed scheme was compared with those of the ACO-OFDM and ACO-SCFDE schemes, where the results show that the PAPR value of the proposed scheme is around 3.7 dB and 1.8 dB lower than the PAPR values of the ACO-OFDM and ACO-SCFDE schemes respectively. In the experimental study, due to the limited time available, only the U-PAM-FDM and ACO-OFDM schemes were practically implemented in real time using the universal software defined radio (USRP) N210 transceiver. The impact of the reduced PAPR value of the proposed scheme was experimentally investigated, where the results demonstrate that implementing the U-PAM-FDM scheme provides 2 dBm more average power in comparison to the traditional ACO-OFDM scheme.

Note that, the average transmitted electrical power in practice was always 3dB higher in comparison to simulations. The reason behind this is not yet known to us. To match the experimental and simulation results, the PD gain in the simulations was set to 3 dB. All parameters used in the simulation and experimental studies are also used for the B-PAM-FDM study in Chapter 6.

Simulation results

We consider 256 IFFT points and a CP duration of 50 ns, which is the maximum time delay for the indoor VLC multipath channel [146]. A 1 W white LED with PCB (HPB8-49KxWDx) [147] was simulated, where its minimum allowed forward voltage V_{min} and its maximum allowed forward voltage V_{max} are 2.7 V and 3.7 V, respectively (i.e., biasing the LED at 75 mA provides 1 V quasi linear range (see Figure 5.18 in subsection 5.3.2)). Therefore, to avoid the clipping noise, the peak-to-peak amplitude of the electrically modulated transmitted signal A_S must swing between this value (i.e., $A_S \geq 1$ V). The indoor VLC channel is modelled as in subsection 4.2.3 (Equation (4.15)), where only a LOS path is considered.

For the DAC, a raised cosine pulse shaping filter (RCPSF) was considered, as defined in Equation (5.8), where its roll off factor (β) was varied from 0 to 1 [68, 148, 149]. The PAPR values of the discrete and continuous OFDM signal (i.e., before and after being passed through RCPSF) are defined by Equations (5.9) and (5.10), respectively [68, 148, 149]:

$$r(t) = sinc\left[\pi\,\frac{t}{T}\right] \frac{\cos\left[\frac{\pi\beta t}{T}\right]}{1 - \frac{4\,\beta^2 t^2}{T}} \tag{5.8}$$

$$PAPR_d = \frac{\max\,|x_n|^2;\quad n = 0,\dots N-1}{E\{|x_n|^2\}} \tag{5.9}$$

$$PAPR_c = \frac{\max\,|x(t)|^2\,;\ 0 \leq t \leq T}{E\{|x(t)|^2\}} \tag{5.10}$$

where T is the OFDM symbol duration, x_n is the discrete OFDM signal (see Equation 5.6), $x(t)$ is the continuous OFDM signal defined by $x(t) = \frac{1}{N}\sum_{k=0}^{N-1} X_k \, r_k(t)e^{2\pi kt/T}$, $r_k(t)$ is the waveform of RCPSF at the kth subcarrier, max $|x_n|^2$ and $E\{|x_n|^2\}$ are the peak and the average power of x_n respectively, and max $|x(t)|^2$ and $E\{|x(t)|^2\}$ are the peak and the average power of $x(t)$, respectively.

Note that, the LED bandwidth, LED dynamic range, PD bandwidth and PD gain of this simulation study are chosen to match the experimental setup. Furthermore, the distance between Tx and Rx in this simulation is chosen to be only 25 cm as the experimental setup shows optimal results at this distance. However, all the parameters used in this simulation are listed in Table 5.1.

Table 5.1 Simulation parameters

Parameter	Value
Number of iterations	1000000
optical concentrator gain $g(\psi)$	0 dB
optical filter gain $T_s(\psi)$	0 dB
Transmitter parameters	
LED Type	1W white LED with PCB (HPB849KxWDx)
LED bandwidth	2Mhz
LED linearity	≈ 1 Volt
The distance between LED and PD	25 cm
LED half power angle $\emptyset_{1/2}$	70^0
Receiver parameters	
Photodetector (PD) type	Thorlab (PDA36A-EC) [150]
PD bandwidth	10 MHz
PD gain	3Db
PD responsivity	1
PD active area	16 mm^2
Receiver field of view (FOV) (full)	180^0

The probability of the PAPR being higher than a certain PAPR threshold ($PAPR_0$) for the ACO-OFDM, ACO-SCFDE and U-PAM-FDM schemes are illustrated in Figures 5.6, 5.7 and 5.8 using the CCDF function, under various operating conditions. The *Y*-axis of these figures represents the CCDF function, which varies from 0 to 1, while the *X*-axis represents the PAPR in [dB] of the aforementioned schemes. All comparisons in these figures were done at $CCDF = 10^{-4}$ (i.e. $Pr\{PAPR > PAPR_0\} = 0.0001$).

Firstly, a PAPR comparison between the aforementioned schemes without considering the RCPSF and the pilot insertion processes is illustrated in Figure 5.6. From these simulation results, it can be clearly seen that the PAPR of ACO-OFDM is higher by almost 3.7 dB and 1.8 dB than the PAPRs of the U-PAM-FDM and ACO-SCFDE schemes respectively. This is due to the insertion of the FFT and the interleaving mapping (odd modulation) blocks before the IFFT block at the OFDM Tx, which makes the OFDM PAPR as low as the SCM one (Chapter 2, subsection 2.3.4.2). However, due to the IM/DD requirements, the HS and SCG blocks need to be implemented after the FFT block at the Tx of the ACO-SCFDE and U-PAM-FDM schemes, respectively, which increases their PAPR in varying percentages in comparison to the PAPR of the SCM scheme, as not all subcarriers enjoy the mapping feature.
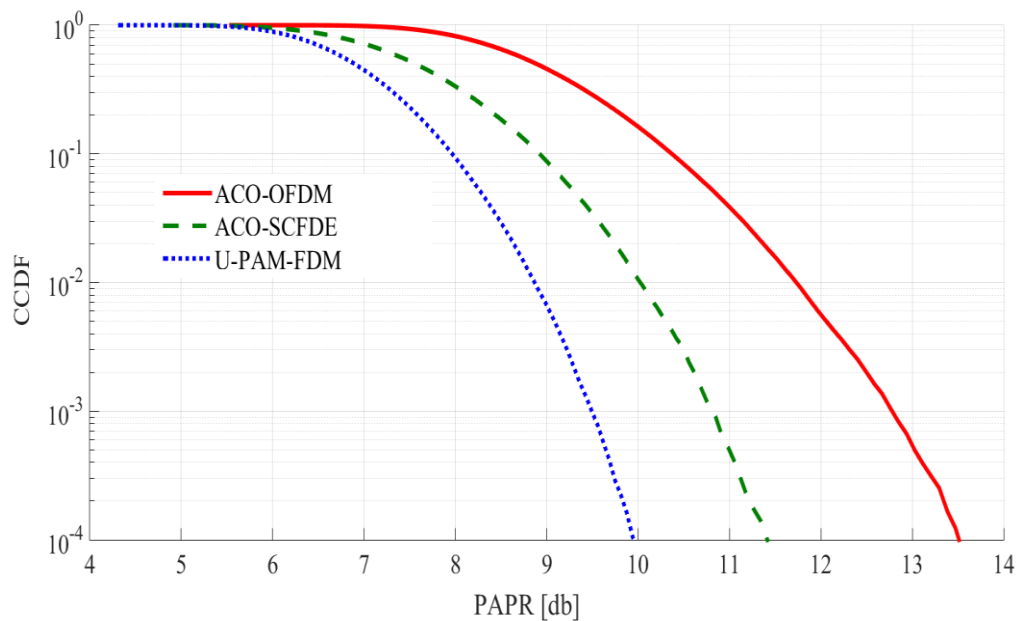
Figure 5.6 CCDF vs. PAPR for ACO-OFDM, ACO-SCFDE and U-PAM-FDM

Next, the effect of pilot insertion on the PAPR of the ACO-OFDM, ACO-SCFDE and U-PAM-FDM schemes was simulated and compared, as illustrated in Figure 5.7. The simulations clearly demonstrate that the PAPRs of ACO-SCFDE and U-PAM-FDM increase by 0.4 dB and 0.55 dB when 8 pilots are inserted, and 0.88 dB and 1.25 dB when 16 pilots are used at the Tx of ACO-SCFDE and U-PAM-FDM respectively, whereas, the insertion of the pilots has no impact on the PAPR of ACO-OFDM.

This is because the insertion of pilots for the ACO-SCFDE and U-PAM-FDM schemes change their subcarriers' order, which reduces the number of subcarriers that enjoy the mapping feature. However, the insertion of pilots might not be needed in VLC systems, as the VLC channel is quite stable and can be estimated once and then adopted for the incoming symbols.
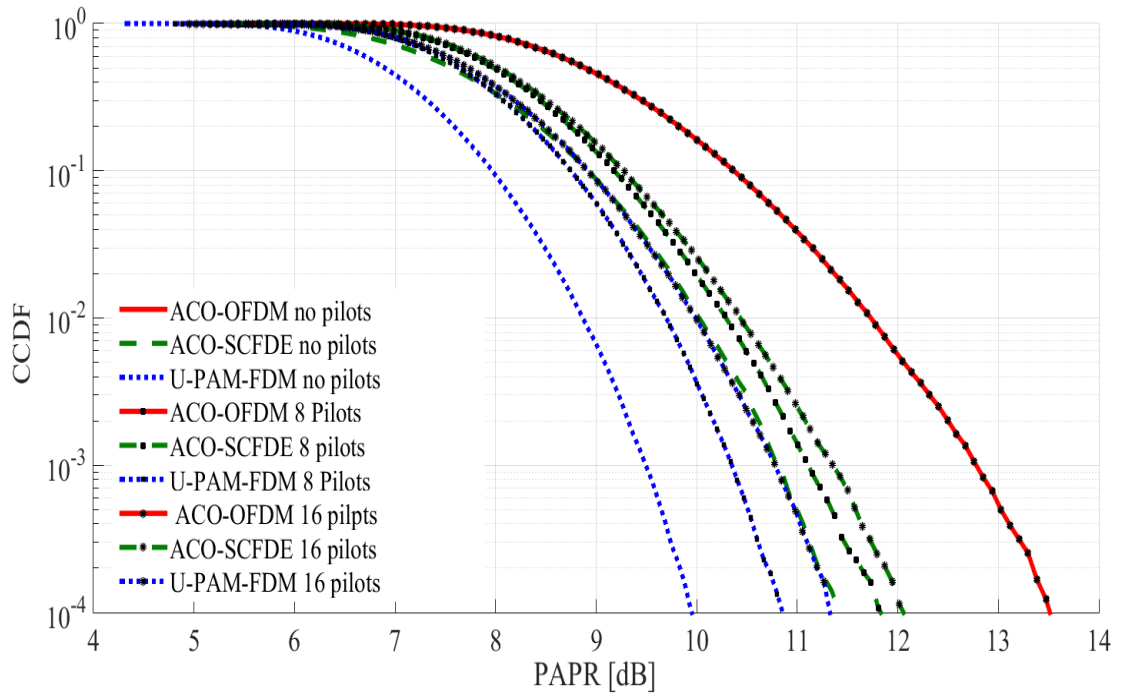
Figure 5.7 The effect of pilots insertion on the CCDF vs. PAPR curves of the ACO-OFDM, ACO-SCFDE and U-PAM-FDM schemes

In wireless communication systems, to convert OFDM time domain samples to an analogue signal, RCPSFs are widely used, which can affect the OFDM PAPR [68, 148, 149]. Figure

5.8 illustrates how the PAPR of the ACO-OFDM, ACO-SCFDE and U-PAM-FDM schemes increase when RCPSF is used. The figure shows that PAPR increases with β.

However, on the other hand, the out of-band radiation increases as β decreases. As such, a trade-off between the out of band radiation and the PAPR value should be considered to improve the system performance.
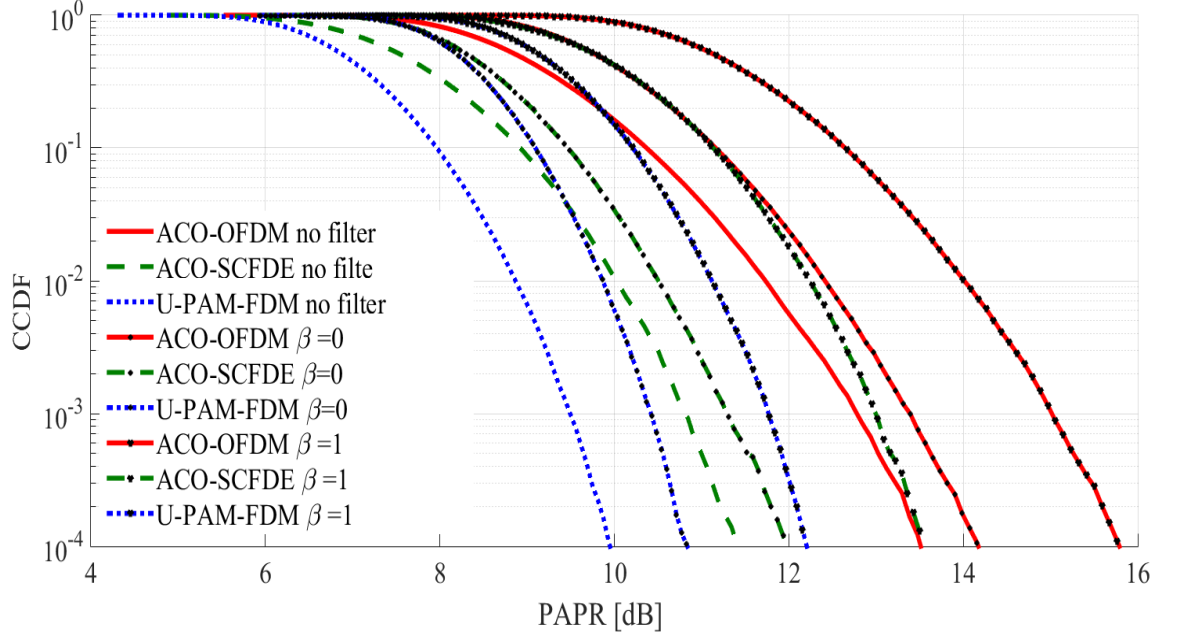
Figure 5.8 Impact of the RCPSF on the CCDF vs. PAPR curves of the ACO-OFDM, ACO-SCFDE and U-PAM-FDM schemes

Finally, the impact of the PAPR value of the aforementioned schemes on the VLC system performance was numerically studied and investigated, as illustrated in Figures 5.10, 5.11 and 5.12, where the impact of the limited LED dynamic range discussed earlier is considered. As the three OFDM schemes have different PAPR values, their transmit average electrical power P_{avg} reaches the LED dynamic range at different dBm values. These dBm values can be identified by simulating the error vector magnitude (EVM) as a function of P_{avg}, and setting the average power of AWGN (σ_n^2) to a fixed value (i.e., σ_n^2 = -10 dBm).

Note that, the EVM measures by how much the received equalized constellation points deviate from the ideal ones, as illustrated in Figure 5.9 and given by [151]:

$$\text{EVM} = \sqrt{(p_{error}/p_{ref})} \times 100 \ \% \tag{5.11}$$

where p_{error} and p_{ref} are the average error vector power and the average ideal reference vector power, respectively. According to [152, 153] for 16-, 64-, and 256-QAM the EVM threshold values should be $\leq 12.5\%$, 8%, 3.5% respectively.
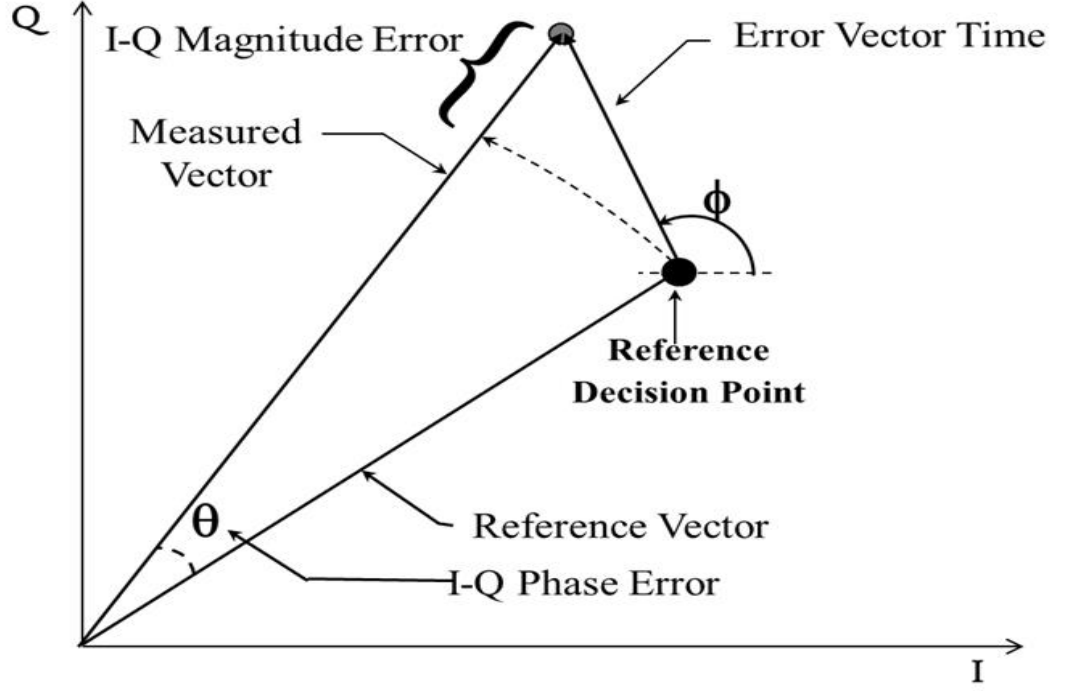
Figure 5.9. Graphical representation of EVM [151]

In Figure 5.10, P_{avg} of the three OFDM schemes is varied from 0 dBm to 25 dBm. From this figure, one can notice that increasing P_{avg} reduces the EVM, and therefore enhances the system performance as SNR increases. However, when P_{avg} reaches a specific value (P_{day}) (i.e., reaches the dynamic range of the LED), the EVM increases (i.e., the system performance downgrading).

Since the three schemes have different PAPR values, their P_{day} values are also different, where P_{day} of ACO-OFDM, ACO-SCFDE and U-PAM-FDM are 19, 20.4 and 21 dBm

respectively. Furthermore, it is clear from the figure that increasing the order of QAM constellation does not have any effect on P_{day}.
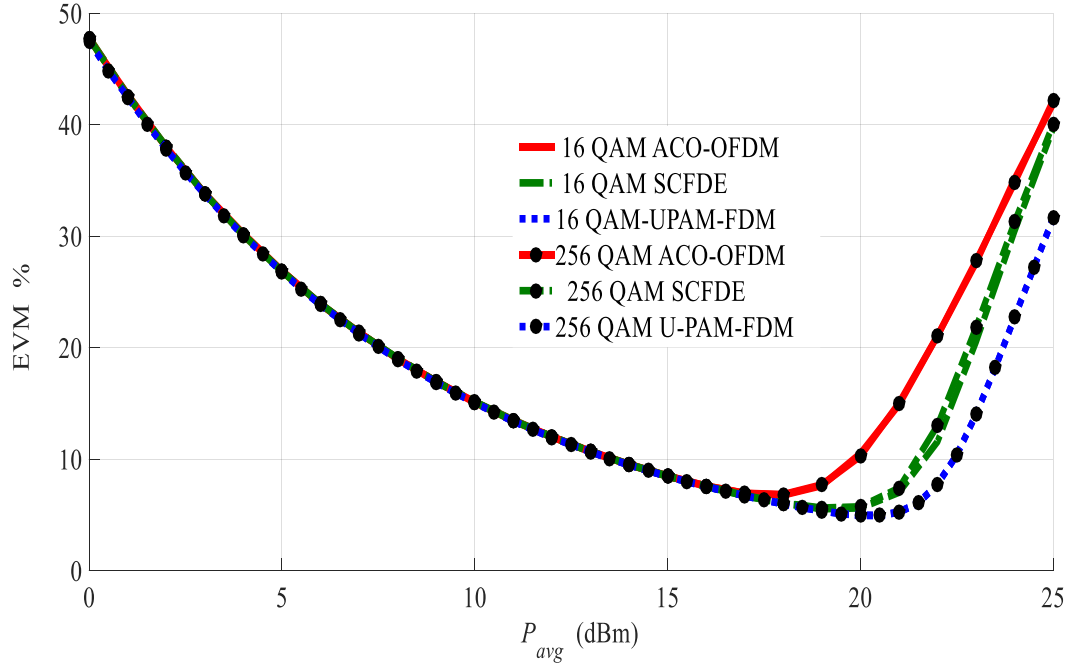
Figure 5.10. EVM % vs P_{avg} for 16- and 256-QAM of ACO-OFDM, ACO-SCFDE and U-PAM-FDM, where $\sigma_n{}^2 = -10$ dBm

To investigate the effect of the clipping noise on the BER performance, Figures 5.11 and 5.12 plot the BER as a function of P_{avg} for ACO-OFDM, ACO-SCFDE and U-PAM-FDM and for a number of constellation orders (i.e., 16-, 64-, 128-, and 256-QAM), as well as $\sigma_n{}^2$ of -10 dBm, while P_{avg} is varied from 0 dBm to 25 dBm (i.e., SNR is varied from 10 dB to 35 dB). These figures illustrate that, the proposed scheme outperforms ACO-OFDM and ACO-SCFDE for all QAM constellation orders, which is due to its the lowest PAPR value. The figures also show that, although P_{avg} of ACO-OFDM reaches the LED dynamic range before P_{avg} of ACO-SCFDE, see Figure 5.10, ACO-OFDM outperforms ACO-SCFDE for the low QAM constellation orders (i.e., $\leq$ 16-QAM).

This is because, ACO-OFDM has lower clipping noise, which can be treated at the Rx when soft and hard decision methods are adopted. However for a low SNR value (i.e., higher QAM

constellation order), even the low clipping noise will not be treated at the Rx (Figure 5.13 shows the histogram plots of the ACO-OFDM, ACO-SCFDE and U-PAM-FDM schemes).
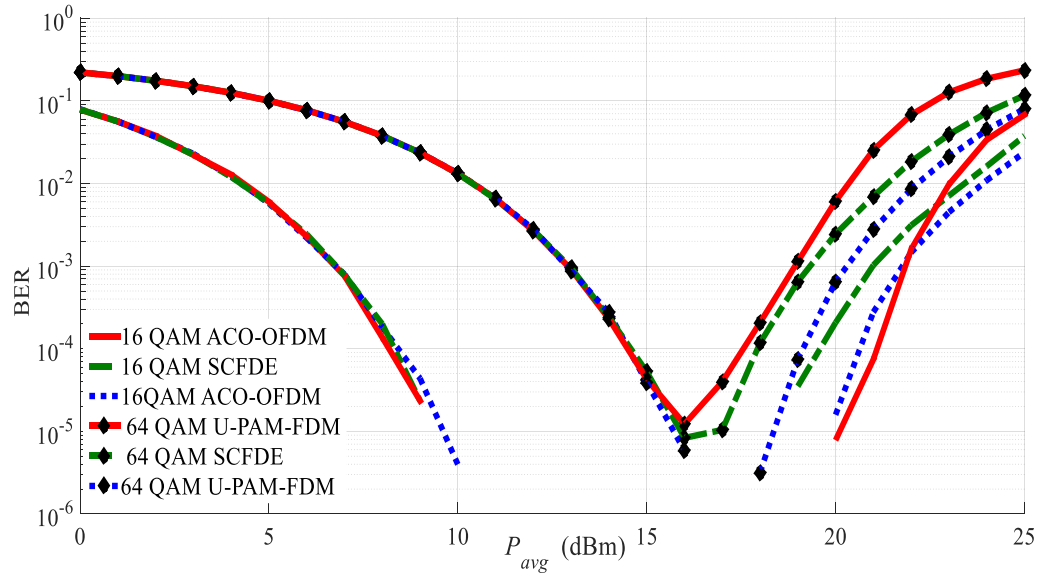
Figure 5.11. BER performance of the ACO-OFDM, SCFDE, UPAM-FDM schemes as a function of P_{avg} for 16- and 64-QAM modulation orders
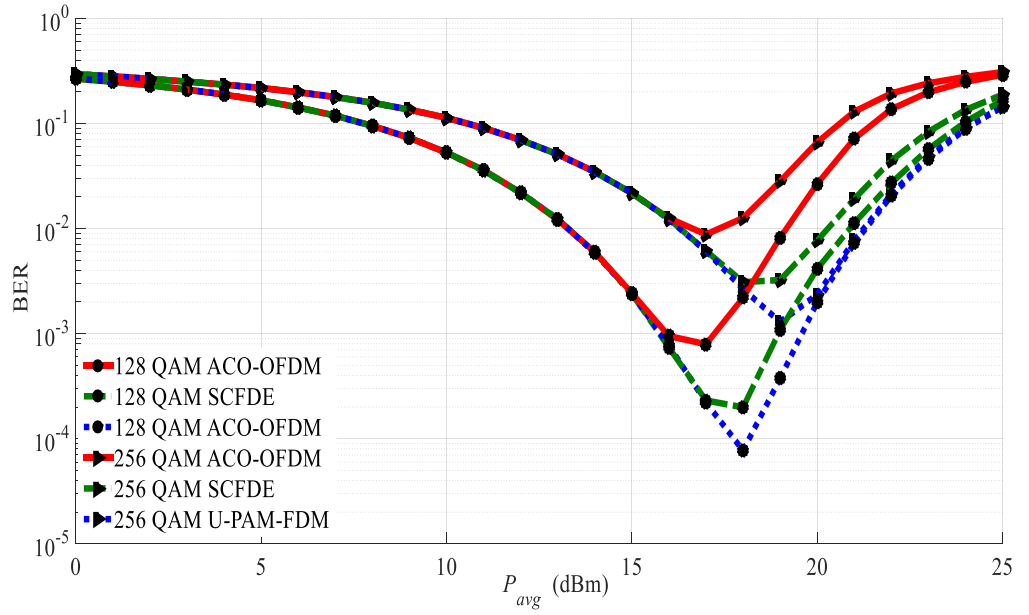
Figure 5.12 BER performance of the ACO-OFDM, SCFDE, UPAM-FDM schemes as a function of P_{avg} for 128- and 256-QAM modulation orders
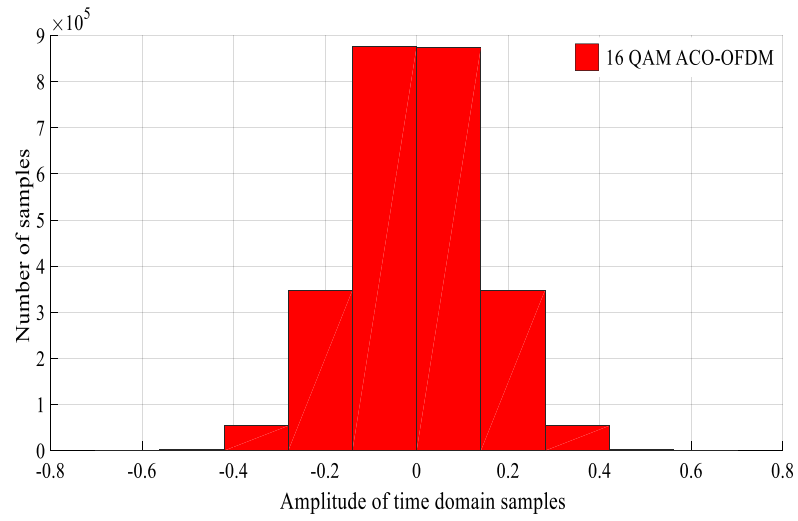
(a)
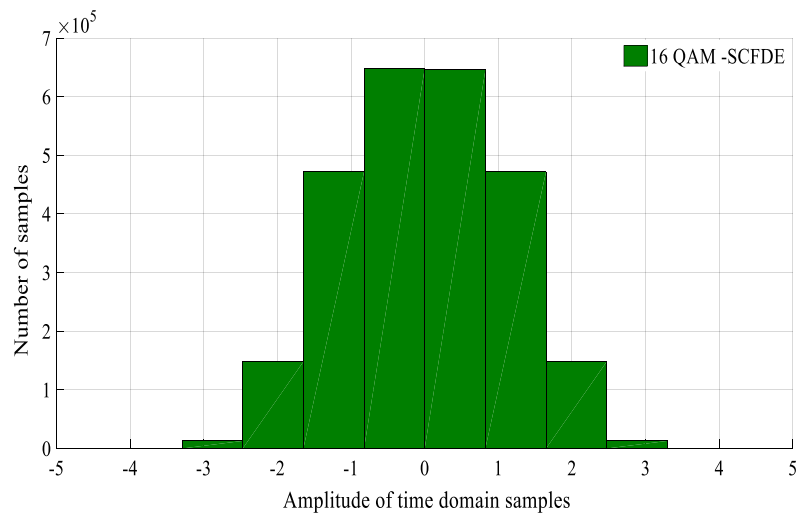
(b)
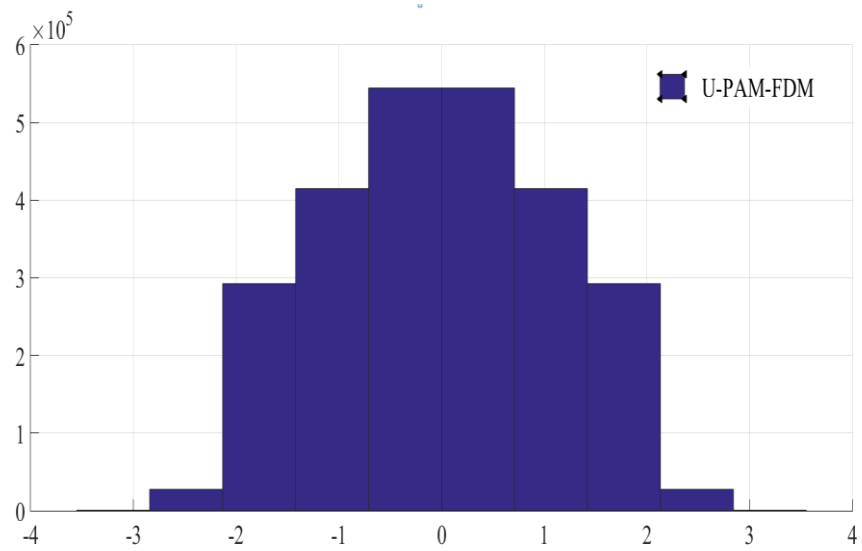
(c)

Figure 5.13 Histogram plots of: (a) ACO-OFDM, (b) ACO-SCFDE, and (c) U-PAM-FDM

Experimental results

This subsection describes the implementation of the U-PAM-FDM scheme in real time using the USRP-N210 transceiver, in order to practically demonstrate how the scheme's lower PAPR offers improved performance in terms of the BER and EVM in comparison to the traditional ACO-OFDM scheme. At Tx side, P_{avg} of the aforementioned two schemes was varied from 0 dBm to 25 dBm, where the effect of this variations on the system performance was verified at the Rx. Figures 5.14 and 5.15 illustrate the experimental setup configuration and the setup hardware respectively.
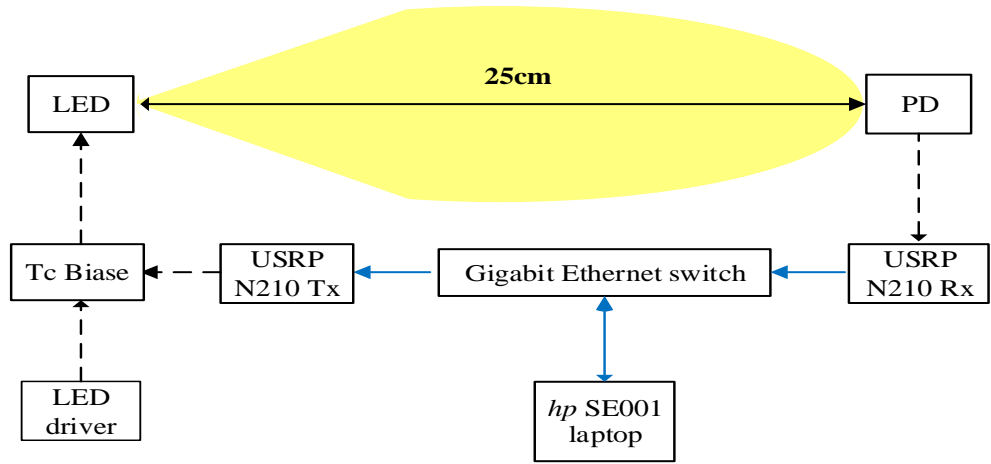
Figure. 5.14. The experimental setup of U-PAM-FDM

Figure. 5.15. Photo of the setup hardware used in the implementation of U-PAM-FDM
(Northumbria university research Lab)

The full experimental process of this work can be summarised as follows:

1) 128 random bits was generated, saved and mapped to 16-QAM constellation points (i.e., 32 complex data symbols). These complex symbols were used to implement the ACO-OFDM and U-PAM-FDM signals. However, in order to filter the spectrum of the aforementioned schemes (i.e., remove ICI), they were zero padded prior to being applied to the IFFT (i.e., the IFFT size of 256) [154, 155]. For synchronization and phase offset purposes, 64 samples were used as CP (Chapter 2, subsection 2.3.6), and following CP insertion, the signal was scaled by a scaling factor (SF), where SF is related to the required P_{avg} (i.e.,0 dBm $\leq P_{avg} \geq$ 25 dBm). Finally, the scaled In-phase/Quadrature (I/Q) baseband signal was applied to the USRP-N210 Tx through a standard gigabit Ethernet cable and a gigabit switch at a specified user sample rate (i.e., 2 Mega samples per second (MSPS) (see Figure 5.16(a))).
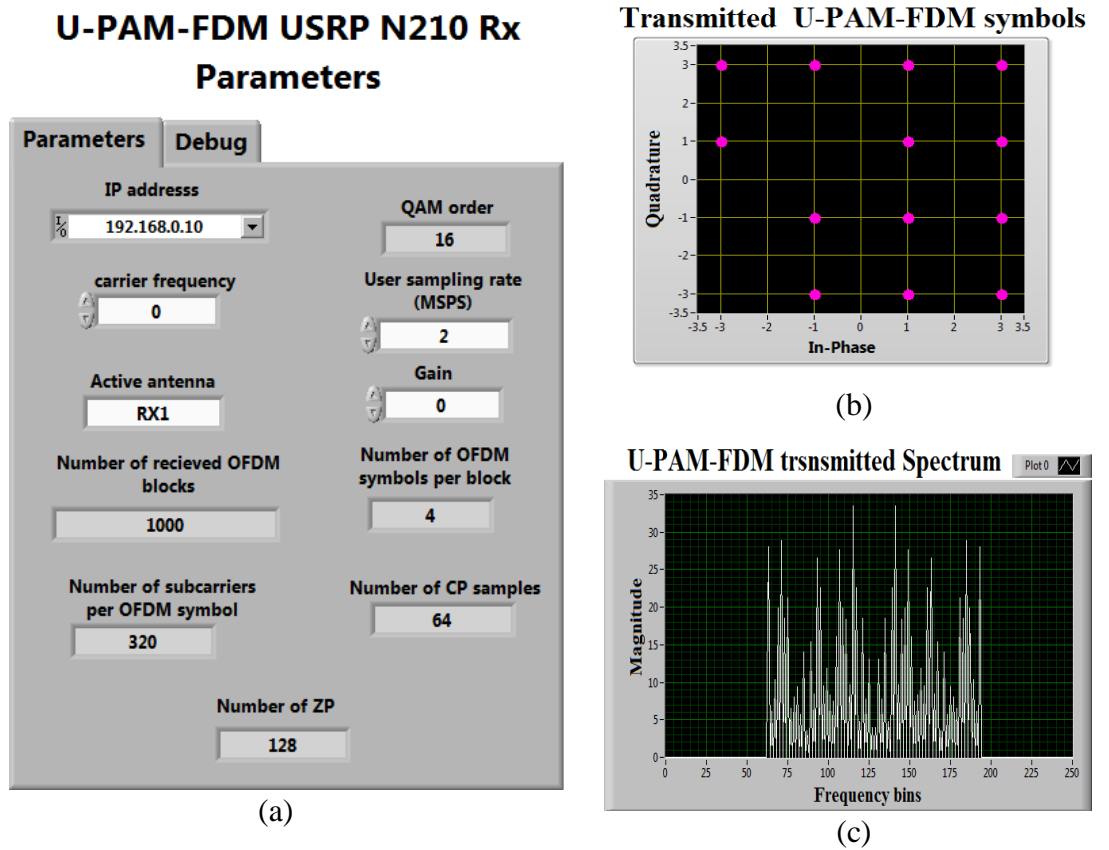
Figure 5.16. LabVIEW control panel of the USRP Tx of U-PAM-FDM, where plots(a), (b) and, (c) depict the U-PAM-FDM Tx parameters, the U-PAM-FDM transmitted symbols, and the U-PAM-FDM transmitted spectrum, respectively

2) As illustrated in Figure 5.17 [156-158] at the USRP-N210 Tx, the received I/Q baseband signal was digitally up-converted (DUC) (i.e., mixed, filtered and interpolated to 400 MSPS), converted to an analogue signal by passing through the DAC module, which had 16 bits resolution and a 1 V peak-to-peak amplitude, and fed to a LPF to reduce the noise and filter out the high frequency components (i.e., > 40 MHz). Subsequently, the signal was mixed with a user-specified carrier using a low frequency Tx daughterboard (LFTx) with a transmission capability from a DC-to-30 MHz, in compatibility with the VLC system bandwidth (in this experimental work, the carrier frequency was set to 0, see Figure 5.17(a)). Finally, the signal was amplified prior to intensity modulation of the LED through the LED driver circuit. Note that, the USRP was interfaced and controlled using the LabVIEW software, see Figure 5.16 (a) for the main Tx parameters adopted.
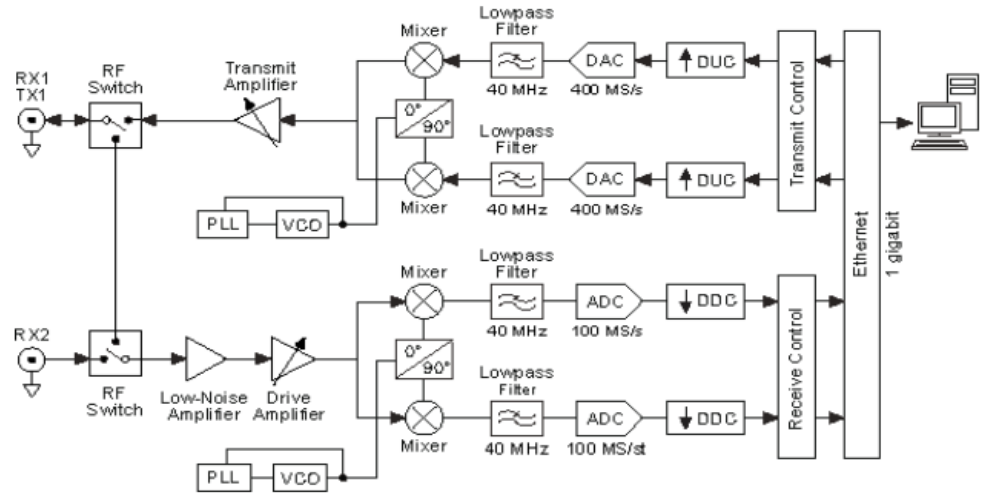
Figure. 5.17.   General USRP architecture [158]

3) A 1 W white LED (HPB8-49KxWDx) introduced in the simulation section was used in this experiment with a drive current of 65 mA (i.e., 2.73 V), thus providing a dynamic range of 1 V. The LED's measured L-I-V curve is shown in Figure 5.18. Note that, the amplitude of the electrical transmitted signal was limited by the dynamic range of the LED and the USRP N210 Tx (i.e. $A_S \geq 1$ V). At the Rx a photodetector (PDA36A-EC) was used to regenerated the electrical signal. The transmission distance (de) between the Tx and Rx was 25 cm.
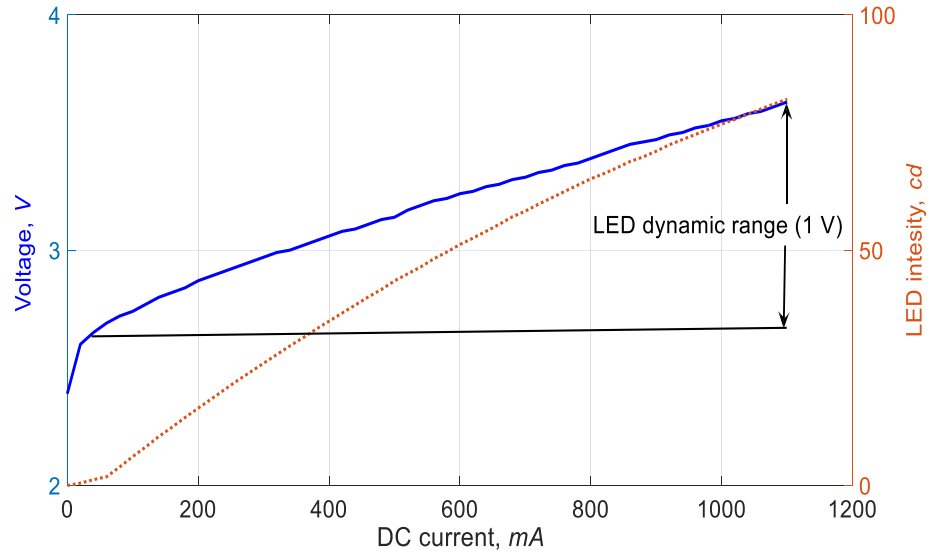
Figure. 5.18 Measured L-I-V curves of the 1 W white LED (HPB8-49KxWDx) used in this work

1000 OFDM blocks received were then processed online, where each OFDM block consisted of 4 OFDM symbols with every symbol composed of 320 samples (i.e., 320 subcarriers). For synchronization and frequency offset correction purposes, a ML algorithm was implemented at each OFDM block by investigating the length of the CP samples, as illustrated in Figures 5.19 (c) and (d) (Chapter 2, subsection 2.3.6). The symbols were then processed online symbol-by-symbol. However, since 128 bits were randomly generated, saved and repeatedly transmitted, 8 subcarriers from each OFDM symbol were used as the data, and the pilots were used to estimate system transfer function (Chapter 2, Subsection 2.3.4). Subsequently, a ZF equalizer was implemented to equalize the received symbols (Chapter 2, subsection 2.3.5). Figures 5.19 (e) and (f) show the received constellation points of U-PAM-FDM before and after the equalization process respectively, where these plots were captured at the EVM of 10%. Finally, the equalized data symbols were passed through a soft decision algorithm, converted to bits, and saved in the host laptop to be compared with the transmitted bits offline in terms of BER and EVM, using a MATLAB program. Note that, the USRP Rx was interfaced to and controlled by the host laptop using the aforementioned LabVIEW software, where Figure 5.19(a) illustrates the Rx parameters

used. USRP utilization process as well as interfacing steps with the LabVIEW software are showed in [159, 160]

(a)

(b)

(c)

(d)

(e)
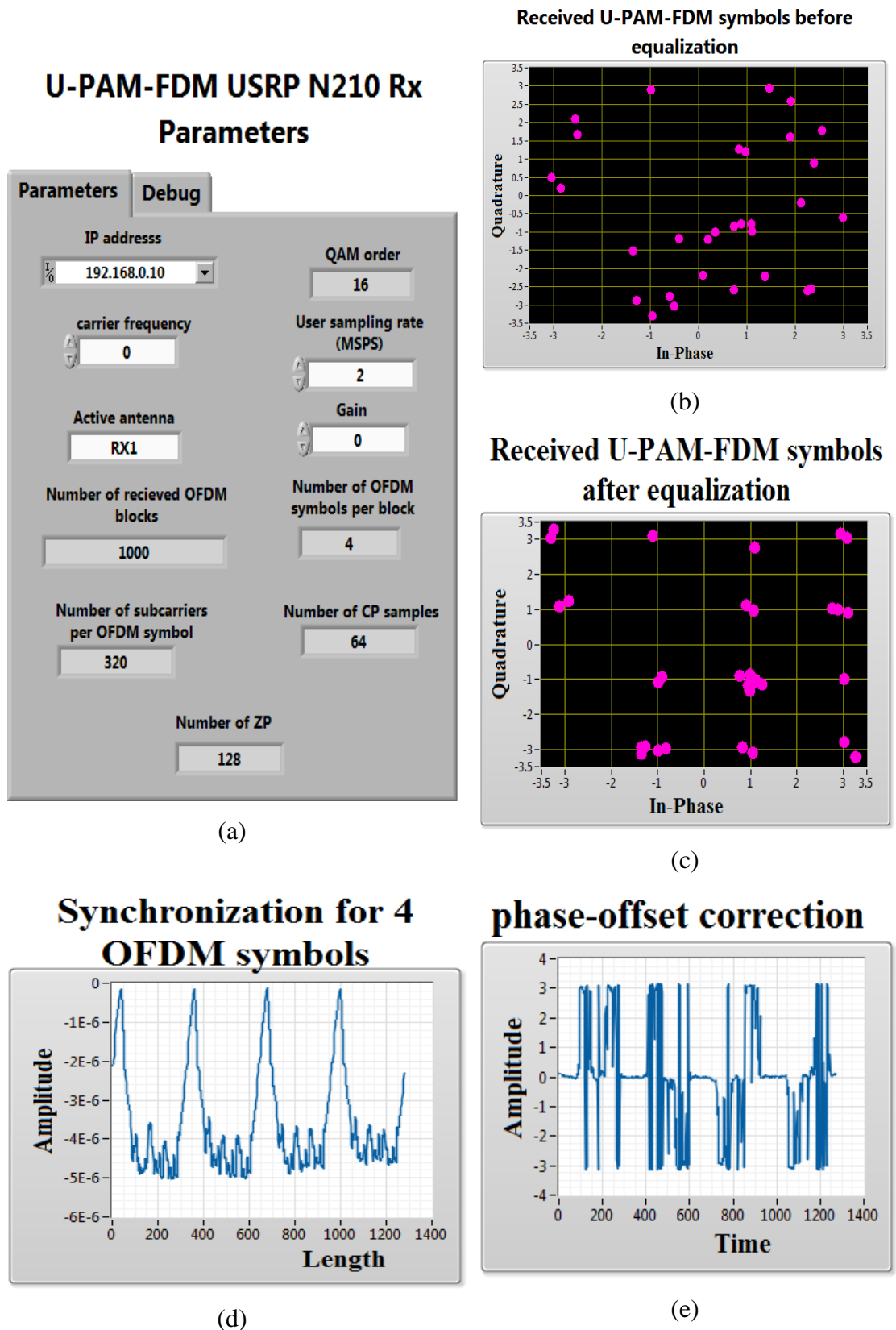
Figure 5.19. LabVIEW control panel of the USRP Rx of U-PAM-FDM. Note that, the 16-QAM constellation points in: (a), and (b) were captured at a EVM of 9.88%)

5.3.2.1 U-PAM-FDM practical results

Figure 5.20 illustrates the BER performance of the 16-QAM ACO-OFDM and 16-QAM U-PAM-FDM schemes for 0 dBm $\leq P_{avg} \leq$ 24 dBm, and *de* of 25 cm. The figure shows that, for $P_{avg} <$ 21 dBm, we observe nearly identical BER performance for both schemes. However, for $P_{avg} \geq$ 21 dBm, the ACO-OFDM system performance is affected by the limited system linear range (i.e., the dynamic range of the LED and USRP), while the U-PAM-FDM system performance is impacted for $P_{avg} \geq$ 23 dBm. As such, U-PAM-FDM offers 2 dBm more P_{avg} in comparison with ACO-OFDM, due to its lower PAPR value. Note that, the plots of this Figure are not continuous, because of the fact of limited number of bits were only being used in the experimental setup.
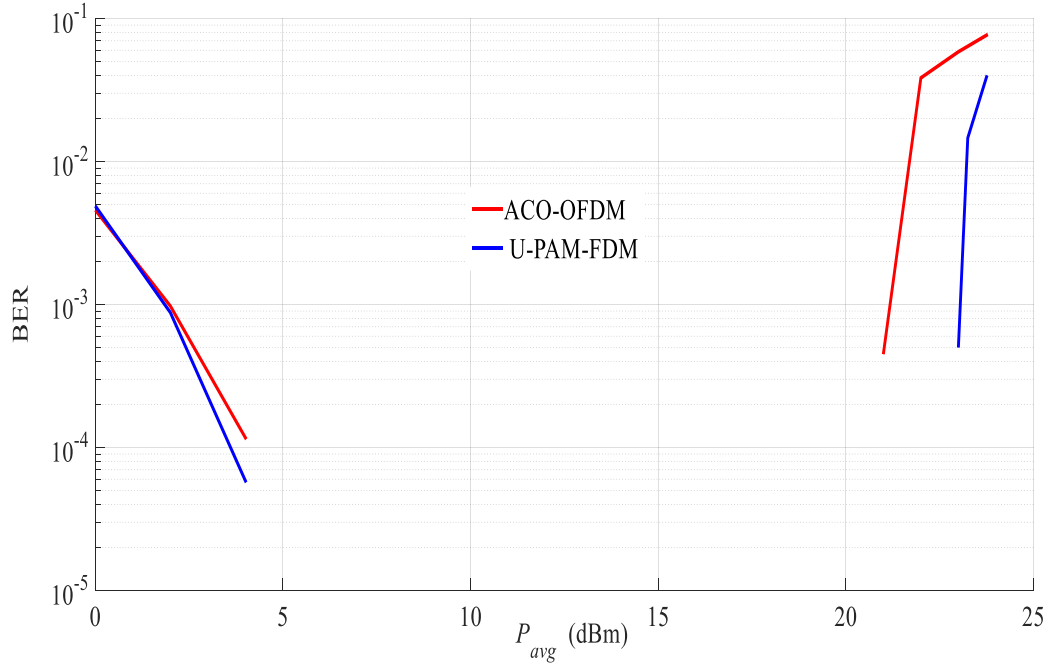
Figure 5.20. BER vs. P_{avg} for ACO-OFDM and U-PAM-FDM

To conduct further investigations, the EVM of the 16-QAM based ACO-OFDM and U-PAM-FDM schemes were measured as a function of P_{avg} for *de* of 25 cm, see Figure 5.21. The results of Figure 5.21 demonstrate that increasing P_{avg} results in reduced EVM for both schemes, and therefore enhancing the system performance. The minimum EVM values of 2.6 % and 1.8 % for the ACO-OFDM and U-PAM FDM schemes were observed at P_{avg} of 20.75 dBm and 22.75 dBm, respectively.

However, beyond the minimum EVM vlaue the system performance deteriorates because of the limited system dynamic range. One interesting fact that can be observed from this figure, is that the EVM values for both schemes abruptly increased significantly after reaching the dynamic range. For example, the EVM of ACO-OFDM increased from 2.6 % to 19 % for P_{avg} increased from 22.75 dBm to 23dBm. This rapid growth in the EVM value is due to the fact that the clipping method was not considered in this study (i.e., any signal outside the system dynamic range will be distorted.).
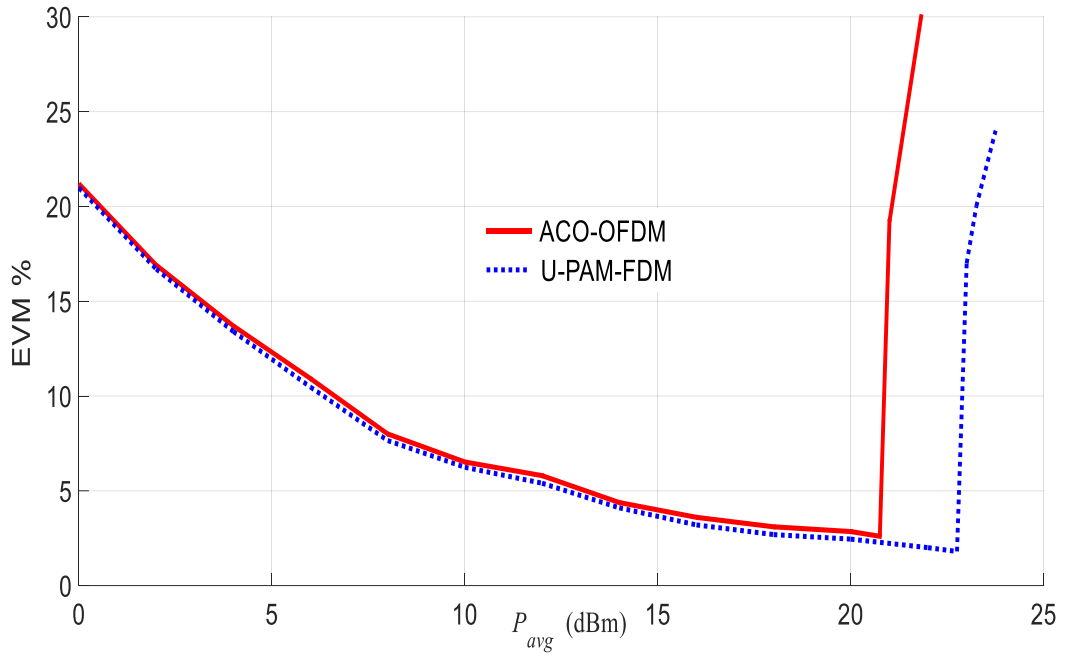
Figure 5.21 EVM vs. P_{avg} for ACO-OFDM and U-PAM-FDM

Therefore, based on the previous discussions, to decrease the effect of this distortion on the system performance, amplitudes of ACO-OFDM and U-PAM-FDM schemes were clipped at 0.98 V (i.e., below the system dynamic range) prior to being applied to the USRP. Figure 5.22 shows how the EVM values of both schemes were enhanced by introducing the clipping method. For example, for ACO-OFDM the EVM values increased from 2.6 % to only 12 % for P_{avg} increased from 20.75 dBm to 21.75 dBm. Furthermore, this improvement in EVM improves the BER performance, see Figure 5.25.
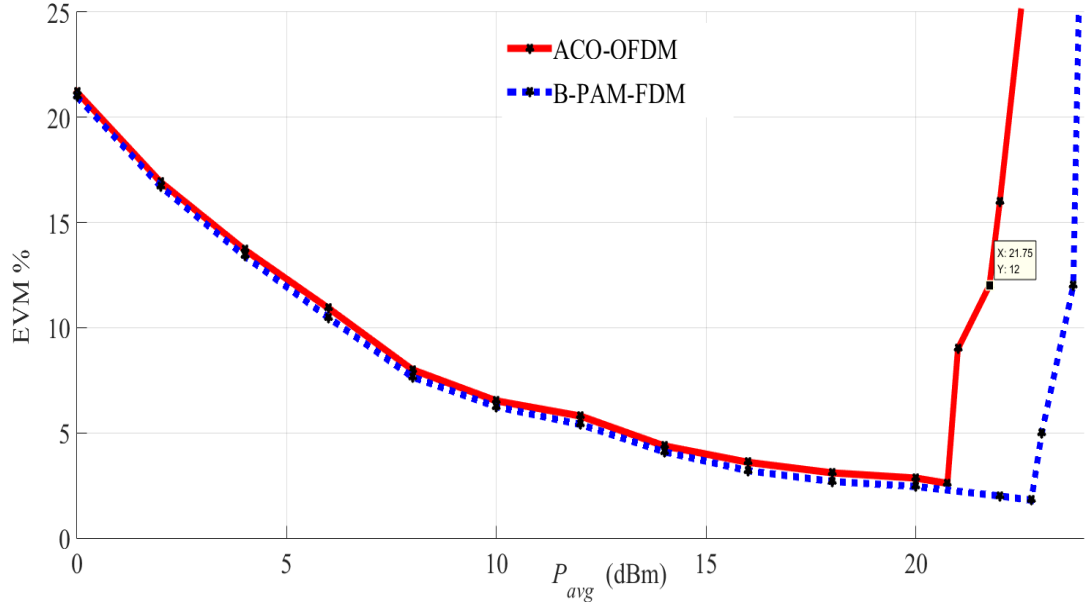
Figure. 5.22. EVM vs. P_{avg} for ACO-OFDM and U-PAM-FDM with the clipping method

Finally, one can clearly see from Figures 5.10, 5.11, 5.20 and 5.22, that there is a disparity between the simulation and experimental results, which is mainly due to the following two reasons:

a) In experimental study, the ZP method was used as a filter to enhance the spectrum shape of both schemes, which affected the PAPR values. The effect of ZP on the PAPR value for both schemes was simulated, and the results are shown in Figure 5.23. The figure demonstrates how zero padding decreases the ACO-OFDM PAPR value by only 0.15 dB, while the U-PAM-FDM PAPR value is reduced by 0.4 dB. Furthermore, the distribution of samples of both schemes can be affected by ZP, which will consequently affect the clipping sample noise value as well as the number of clipped samples. Figures 24(a) and 24(b) depict the histogram plots of ACO-OFDM and U-PAM-FDM respectively when ZP is considered. Note that, the histogram plots of both schemes without ZP were illustrated in subsection 5.3.1 by Figure 5.13.
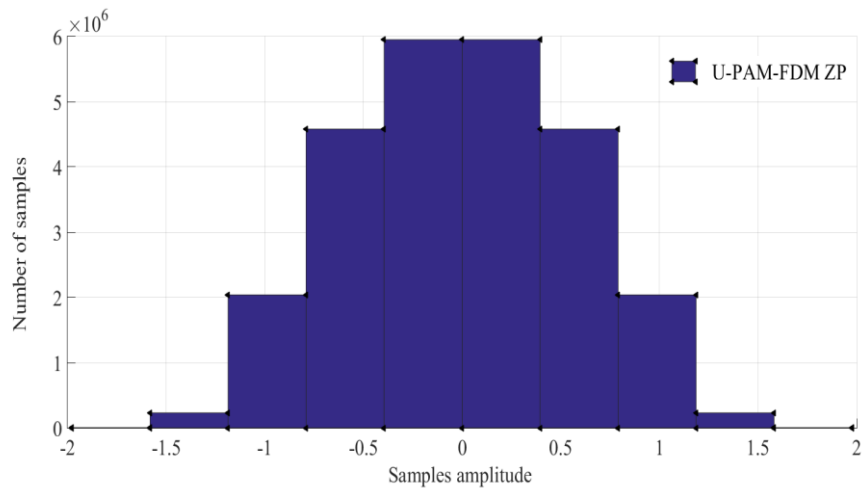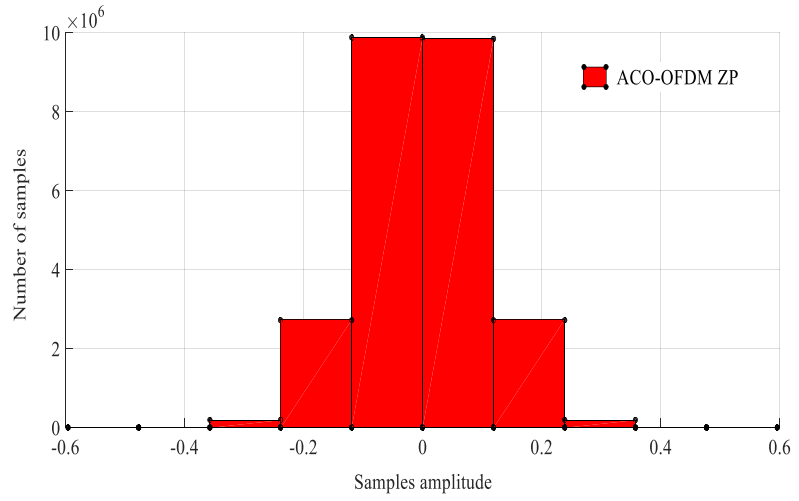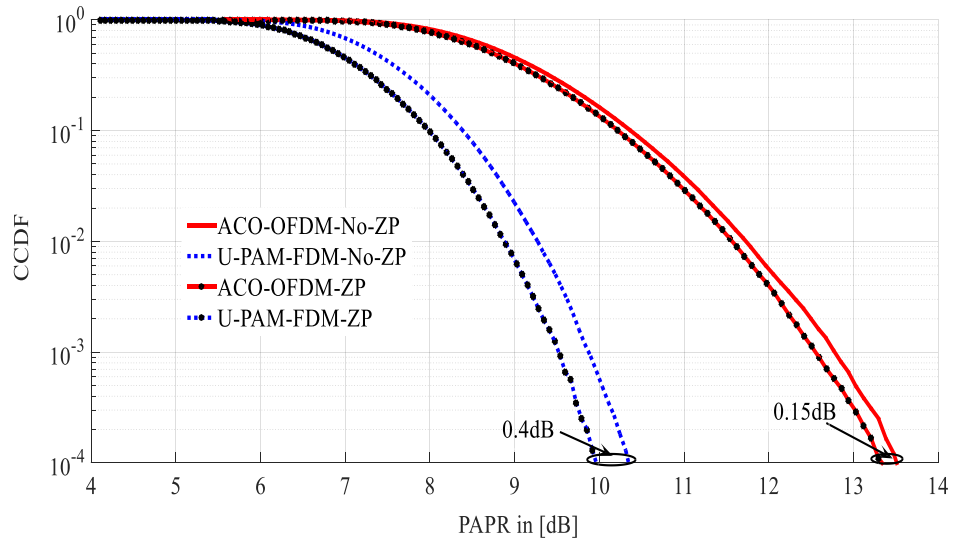
Figure 5.24. The histogram plots of: (a) ACO-OFDM and (b) U-PAM-FDM with

b) Only 128 bits were randomly generated and used in both schemes. As such, bearing in mind that, the PAPR value varies from symbol to symbol, and the experimental investigation was only based on randomly generated 128 bits, whereas in the simulations 100,000 bits (i.e., 1555 OFDM symbols) were used to implement the aforementioned schemes (i.e., each PAPR value in the simulation plot is the average of the PAPR values of these 1555 OFDM symbols).

Figure 5.25 compares the experimental and simulation results for the BER performance of both schemes for 128 bits (note that, both schemes were clipped at 0.98 V, and β was set to 0.4 in the simulations). The figure clearly shows a close match between simulation and experimental results when using the ZP method and the same bits. It is worth mentioning that the plots in Figure 5.25 are not continuous because of the limited number of bits used in both experimental and simulation studies.
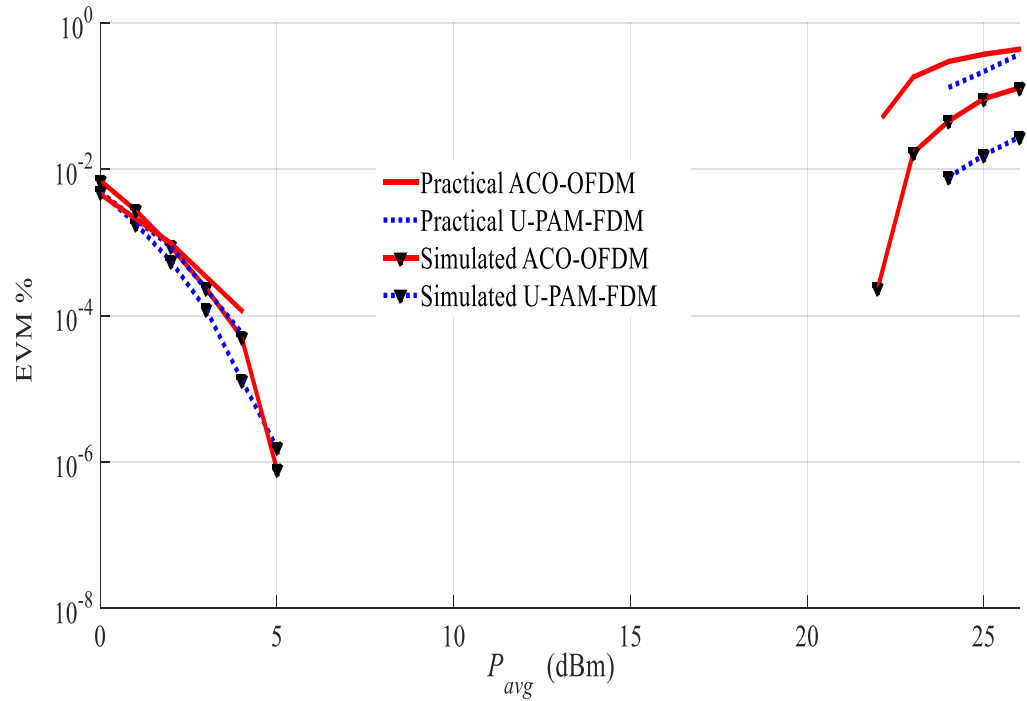
Figure 5.25. A comparison between the experimental and simulation results of the BER performance of ACO-OFDM and U-PAM-FDM with ZP and 128 bits

5.4 Summary

A new unipolar pulse amplitude modulation frequency division multiplexing scheme was introduced in this chapter as a means to reduce the PAPR value of the unipolar optical OFDM scheme by modifying IFDMA in order to be used in for IM/DD based VLC. This was achieved by making the input FFT symbols at the IFDMA Tx to be real symbols (i.e., PAM) and subsequently conjugating the output FFT subcarriers, except the first and middle subcarriers. However, to make all IFFT input subcarriers conjugate, two subcarriers were added before the interleaving mapping process, resulting in real asymmetric time domain samples suitable for IM/DD.

The simulation results of U-PAM-FDM were presented demonstrating that for U-PAM-FDM the PAPR values of is 3.7 dB and 1.8 dB were lower than that of ACO-OFDM and ACO-SCFDE respectively. The impact of reduced PAPR in U-PAM-FDM on the BER performance was experimentally investigated, where the results showed that U-PAM-FDM offered higher P_{avg} by 2 dBm compared to the traditional ACO-OFDM scheme. Note that, only 128 bits were used to implement the ACO-OFDM and U-PAM-FDM schemes. However, there are no reasons why higher number bit should not be investigated as part of the future works.

CHAPTER 6

B-PAM-FDM AND O-IFDMA

SCHEMES

6.1 Introduction

As already discussed in the previous chapters, DC-bias is needed in VLC systems to turn on the LEDs, provide an illumination service and remove the effect of the pulse shaping filter, which can convert unipolar signals to bipolar ones [6, 10, 149]. However, the unipolar OFDM schemes can outperform bipolar OFDM when a lower DC-bias level is required, as a high dc-bias is needed in the bipolar OFDM schemes to convert the high negative peak samples into positive ones. Nevertheless, this benefits of the unipolar OFDM schemes comes at the cost of spectral efficiency [10].

In Chapter 5, a unipolar PAM-FDM scheme was introduced to reduce the PAPR of OFDM in IM/DD based VLC systems, by making the IFDMA scheme suitable for IM/DD. However, the insertion of a SCG block between the odd modulation and IFFT blocks is part of the IM/DD requirements for this scheme, making its PAPR higher than the PAPR of the IFDMA and SCM schemes. In this chapter, the IFDMA scheme is implemented in two different ways that are compatible with IM/DD, thus resulting in two new novel bipolar OFDM schemes known as the bipolar PAM-FDM (B-PAM-FDM) scheme and the optical IFDM (OIFDM) scheme, both of which possess a PAPR value as low as that of the RF IFDMA scheme.

The only difference between B-PAM-FDM and IFDMA is that in the B-PAM-FDM scheme the repeating mapping (RM) block is inserted after the FFT block, whereas in the latter the interleaving mapping block is used in IFDMA instead. In the RM block, the output FFT vector is repeated twice before going through the IFFT block, which makes the even IFFT output samples the same as the input data symbols, and the odd output samples zeros. Therefore, making the data symbols real (i.e., PAM symbols), results in real IFFT output samples suitable for IM/DD, at the cost of halving the spectral efficiency, as the imaginary parts are not utilised. However, since the odd samples do not carry any data in B-PAM-FDM, another OFDM signal can be transmitted in theses odd samples using the time division multiplexing technique (TDM). In addition, theses B-PAM-FDMA unused samples can be utilised for illumination, time domain equalization, positioning and localization. Furthermore, due to the presence of the RM block, any affected subcarrier in B-PAM-FDM can be easily compensated.

In the OIFDM scheme, IFDMA is made suitable for IM/DD by investigating its interleaving mapping characteristics. However, due to the interleaving mapping of the IFDMA frequency domain signal, the output time domain samples of the IFFT block will be asymmetrically repeated Q-times over the IFDMA symbol period, where Q is the interleaving mapping factor (see Chapter 2, subsection 2.3.4.2). This symmetrical characteristic of IFDMA is exploited by setting $Q = 2$, which results in each time-domain OFDM symbol being divided into two sub-symbols, where the first sub-symbol (R) carries the real OFDM samples, while the imaginary OFDM samples are carried by the second sub-symbol (I). In this work, this process is referred to as the intensity modulation process (IMP). However, since the first OIFDM subcarrier is a modulated subcarrier, all OIFDM time domain samples will be affected by the DC-bias and the ambient light noise. This effect is reduced in this scheme by estimating the first OIFDM subcarrier at the cost of increasing the required SNR.

This chapter is structured as follows. The B-PAM-FDM scheme is presented in Section 6.2, along the B-PAM-FDM system model the B-PAM-FDM results and discussion. Section 6.3

introduces the OIFDM scheme and describes its system model. The section also discusses DC-bias noise reduction techniques, and presents simulation results of the OIFDM system. Finally, a summary of this chapter is presented in Section 6.4.

6.2 Bipolar-PAM-FDM (B-PAM-FDM)

This section introduces the B-PAM-FDM singling scheme as a means of making PAPR of DCO-OFDM low. This is achieved by replacing the HS block with an FFT block, and duplicating the output FFT vector, before the implementation of the IFFT operation at the DCO-OFDM Tx, and making the data symbols real symbols (i.e., PAM).

6.2.1 B-PAM-FDM system model

In this section, the signal processing of the proposed scheme is illustrated and explained in detail.

  a) **B-PAM-FDM Tx**

Figure 6.1 shows an example of the B-PAM-FDM Tx signal processing procedure. First, a number of random serial binary input bits $bi(t)$ are serial to parallel converted and PAM mapped, where the real output symbol vector is given as: $p = \{p_0, p_1, p_2, \dots \dots \dots p_{M-1}\}$, and M is the number of transmitted data symbols. The real vector p is then converted to a frequency domain vector by implementing the FFT operation, where the resulting FFT output sub-carriers (P) are conjugated symbols (see Figure 2.1) as established below:

$$P_k = \sum_{m=0}^{M-1} p_m \, e^{\frac{-j2\pi mk}{M}} \tag{6.1}$$

$$P_{M-k} = \sum_{m=0}^{M-1} p_m \, e^{-j(\frac{2\pi m}{M})(M-k)}$$

$$= \sum_{m=0}^{M-1} p_m \, e^{-j(2\pi m - \frac{2\pi mk}{M})}$$

$$= \sum_{m=0}^{M-1} p_m \, e^{\frac{j2\pi mk}{M}}$$

(6.2)

From Equations (6.1) and (6.2), it can be clearly seen that each kth subcarrier is conjugated with the $M - k^{th}$ subcarrier (i.e., $P_k = P^*{}_{M-k}$), for p is a real vector. Subsequently, P is repeated twice by being passed through the RM process, where the new frequency domain output symbols vector (X) has a length of N, and $N=2M$, which is defined as (6.3):

$$X = \{p_0, p_1, p_2, \ldots p_{M-1}, p_0, p_1, p_2, \ldots p_{M-1}\}$$

(6.3)

$$X = \{X_0, X_1, X_2, X_3, X_4, , , , , , , , , , , , \ldots X_{N-1}\}$$

X is then converted back to a time domain samples vector (x) by going through the IFFT block. However, because the IFFT operation is implemented before the RM and FFT blocks, x has as low a PAPR value as that of a single carrier modulation scheme, as shown below:

$$x_n = \frac{1}{N} \sum_{l=0}^{N-1} X_l \, e^{\frac{j2\pi ln}{N}}$$

(6.4)

$$x_n = \frac{1}{N} \left| \sum_{l=0}^{\frac{N}{2}-1} X_l \, e^{\frac{j2\pi ln}{N}} + \sum_{l=\frac{N}{2}}^{N-1} X_l \, e^{\frac{j2\pi ln}{N}} \right|$$

From Equation (6.4), the following equation can be deduced:

$$x_n = \frac{1}{N} \left[\sum_{k=0}^{M-1} P_l \, e^{\frac{j2\pi nk}{N}} + \sum_{k=0}^{M-1} P_k \, e^{\frac{j2\pi n(M+k)}{N}} \right]$$

(6.5)

$$x_n = \frac{1}{N} \left[\sum_{k=0}^{M-1} P_l \, e^{\frac{j2\pi nk}{N}} + \sum_{k=0}^{M-1} P_k \, e^{j(\pi n + \frac{2\pi nk}{N})} \right]$$

Therefore, the odd and even samples of x can be respectively defined as:

$$x_{n\_Odd} = \frac{1}{N} \left[\sum_{k=0}^{M-1} P_l \, e^{\frac{j2\pi nk}{N}} - \sum_{k=0}^{M-1} P_l \, e^{\frac{j2\pi nk}{N}} \right] = 0$$

(6.6)

$$x_{n\_Even} = \frac{1}{2M}\left[\sum_{k=0}^{M-1} P_l\, e^{\frac{j2\pi nk}{M}} + \sum_{k=0}^{M-1} P_l\, e^{\frac{j2\pi nk}{M}}\right]$$

$$x_{n\_Even} = \frac{1}{M}\sum_{k=0}^{M-1} P_l\, e^{\frac{j2\pi nk}{M}} \tag{6.7}$$

From Equations (6.6) and (6.7), one can see that x_{n_Even} is a repeated signal of p_m, while no samples are carried on x_{n_Odd} (i.e. $x_{n\_Odd} = 0$) (see Figure 6.1). Note that, as B-PAM-FDM uses PAM as a modulation technique, its spectral efficiency is half of that of the DCO-OFDM scheme (i.e., has the same spectral efficiency as ACO-OFDM). However, since no samples are carried by x_{n_Odd}, other B-PAM-FDM samples can be transmitted using the TDM method. In addition, x_{n_Odd} can be utilised in illumination, localization, and time domain synchronization, as will be demonstrated in our future work. Furthermore, because of the RM process, any damaged subcarrier in this scheme can be easily compensated (i.e. because of the DC-bias, the first subcarrier will be compensated by the middle one at the Rx (see Figure 6.1)). Finally, x is passed through the p/s converter, CP insertion, DAC, LPF, DC-bias, clipping, and EOC blocks.
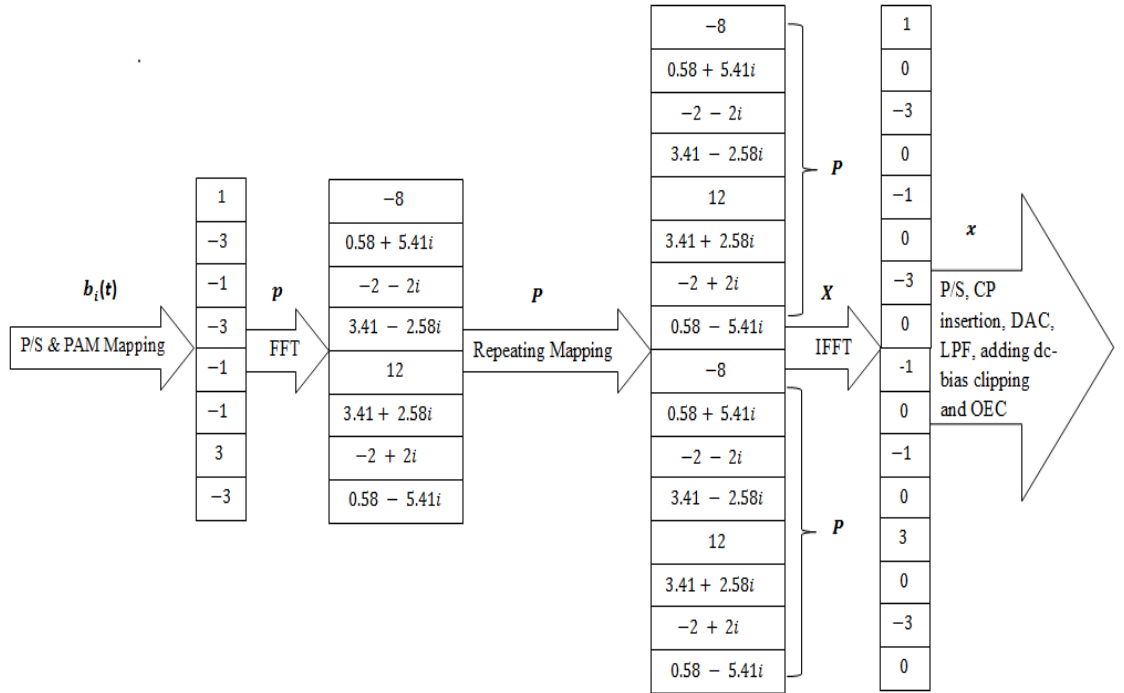
Figure 6.1 An example of the B-PAM-FDM Tx signal processing procedure

b) B-PAM-FDM Rx

Figure 6.2 depicts the block diagram of the B-PAM-FDM Rx, where its signal processing can be described as follows. Firstly, the transmitted optical signal is convoluted with the impulse response of the system, before being detected and converted back to an electrical signal by the PD. However, because of the photocurrent fluctuations as well as the receiver electronics, the shot noise and terminal noise, which are modelled as AWGN, will be added to the electrical signal. As such, the resulting analogue electrical signal $r\,(t)$ is defined as: $r(t) = s(t) * h(t) +\ n(t)$, where $s\,(t)$ is the transmitted electrical signal, $h(t)$ is the time domain system impulse response, $n(t)$ is the AWGN, and the symbol * denotes the linear convolution operation (note that the PD is considered to be ideal (i.e., PD responsivity = 1)). $r(t)$ is then passed through the LPF, ADC, CP removal, and S/P blocks, where the resulting digital signal $d(t)$ of the aforementioned processes is converted to the frequency domain $Y(F)$ by being fed to the FFT block. Note that, since CP converts the linear convolution induced by the system to circular convolution (i.e., multiplication in the frequency domain (Chapter 2 subsection 2.3.2)), $Y(F)$ is given by:

$$Y(F) = X(F).H(F) + N(F) \qquad (6.8)$$

where, $H(F)$ is the transfer function of the system. The transmitted subcarriers, including the redundant ones, are subsequently easily estimated by implementing the ZF equalizer (Chapter 2, subsection 2.3.5), as in (6.9):

$$\check{X}(F) = \frac{Y(F)}{\widehat{H}(F)} \qquad (6.9)$$

$\widehat{H}(F) \approx H(F)$ is The estimated transfer function of the system, which is already known using the training pilots method (Chapter 2, subsection 2.3.4). Therefore, we can express the following:

$$\check{X}(F) = X(F) + N(F) \qquad (6.10)$$

After that, the redundant subcarriers, including the DC-bias subcarrier and repeated subcarriers, are removed by passing $\check{X}$ through the redundancy removal process. However, because of the RM process at Tx (i.e., $\check{X} = \left[\frac{\check{X}}{2} \; \frac{\check{X}}{2}\right]$ (see Figure 6.1)), removing these redundant subcarriers does not cause any loss of information after compensating the first subcarrier by the middle one. Finally, the resulting signal from the redundancy removal process is converted back to the time domain by implementing an IFFT and subsequently passing through the PAM de-mapping and hard decision processes, in order to reconstruct the transmitted data bits.
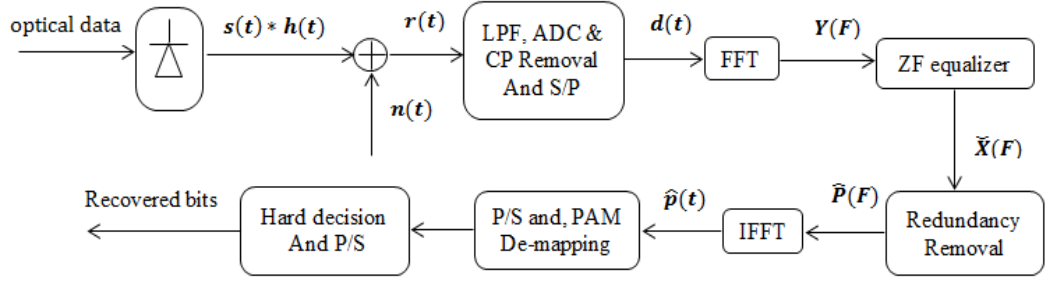
Figure 6.2 Block diagram of the B-PAM-FDM Rx

6.2.2 B-PAM-FDM results and discussion

The reduction of the PAPR value of OFDM in IM/DD systems was mathematically established in the previous section by implementing the FFT and RM processes before the implementation of the IFFT method. In this section, simulation and experimental results are presented to further identify how the PAPR of DCO-OFDM and its negative impacts on the VLC system performance are reduced when the B-PAM-FDM scheme is considered. The simulation results show that the PAPR of the proposed scheme is 7 dB lower than that of the traditional DCO-OFDM scheme. Furthermore, this PAPR reduction was exploit experimentally by increasing the maximum distance between the Tx and the Rx by 44% in the proposed schemed, in comparison to the traditional DCO-OFDM. The PAM symbols are generated at the Tx by separating the real and the imaginary parts of the QAM symbols (i.e. a + bj QAM symbol is separated into 'a' and 'b' PAM symbols) to obtain an optimum

comparison between B-PAM-FDM and DCO-OFDM in term of SNR, BER and EVM, where these symbols are combined together at the Rx to reconstruct the QAM.

a) Simulation results

256 IFFT points, 16 QAM constellation points and 50 ns CP duration were considered in this simulation study. The rest of the parameters, such as the LED Type, LED dynamic range, LED bandwidth, PD responsivity, PD bandwidth, PD gain, VLC channel model parameters, and RCPSF parameters are all identical to those used in Chapter 5, subsection 5.3.1.

Figure 6.3 depicts the BER performance vs. the SNR for the DCO-OFDM and B-PAM-FDM schemes for 16-QAM. The figure shows that DCO-OFDM requires almost 3dB more SNR in comparison to B-PAM-FDM to achieve the same BER value. This is because in B-PAM-FDM, only the even time domain samples carry data, while in DCO-OFDM, all the samples are used to carry data, making the DCO-OFDM scheme have double the spectral efficiency of B-PAM-FDM. However, as previously mentioned, using the TDM method resulted in the B-PAM-FDM scheme having the same spectral efficiency as DCO-OFDM. Furthermore, as VLC systems can be used in a variety of applications in addition to data communications, these unused samples can be utilised for illumination, synchronization, time domain equalization, and localization applications.
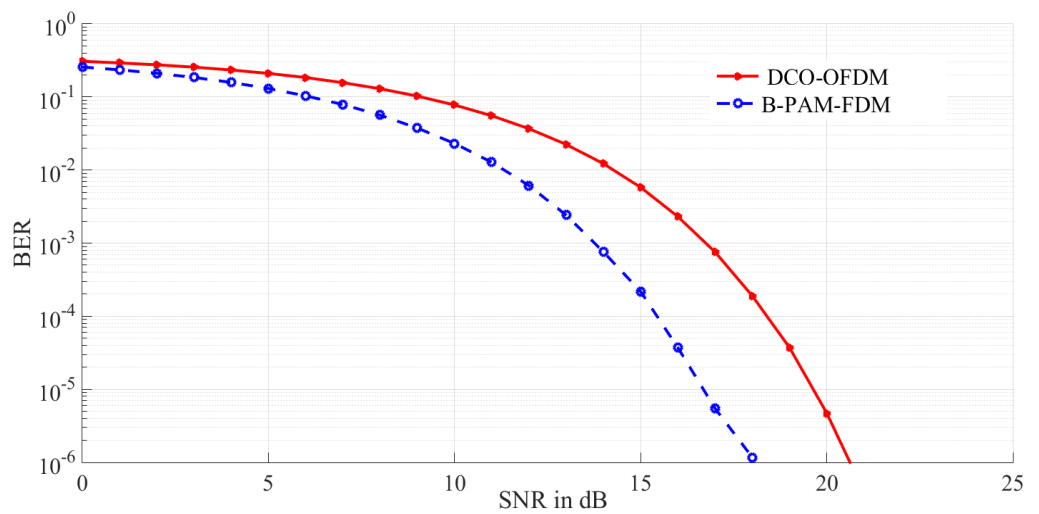
Figure 6.3 SNR vs BER for 16 QAM DCO-OFDM and 16 QAM B-PAM-FDM

To compare the PAPR value of the proposed scheme with that of the DCO-OFDM scheme, the CCDF of both schemes were simulated as shown in Figures 6.4 and 6.5. Note that, the PAPR value in [dB] of DCO-OFDM and B-PAM-FDM is represented in these figures by X-axis, while the CCDF is illustrated by Y-axis. All PAPR comparisons were carried out at CCDF$= 10^{-4}$ (i.e. Pr{PAPR > PAPR$_0$} = 0.0001). Figure 6.4 plots the probability of the PAPRs of the B-PAM-FDM and DCO-OFDM schemes being higher than a certain threshold (PAPR$_0$). The figure demonstrates that the PAPR of the proposed scheme is about 7 dB lower than the DCO-OFDM scheme. This is due to the implementation of the FFT and RM blocks before the IFFT block, which makes the B-PAM-FDM PAPR value as low as the SCM scheme (see Figure 6.1 and Equation 6.6).
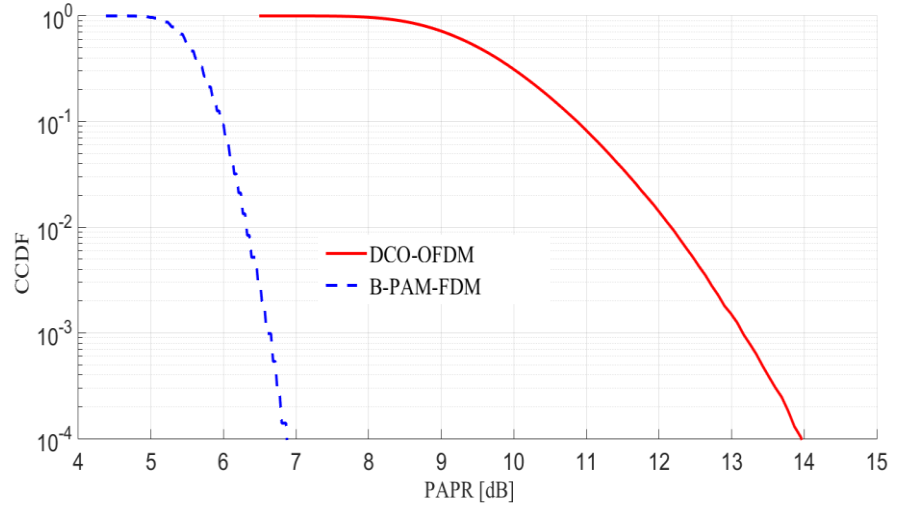
Figure 6.4 CCDF vs. PAPR of the DCO-OFDM and B-PAM-FDM schemes, where the number of IFFT points = 256

As already mentioned in Chapter 5, subsection 5.3.1, RCPSFs are widely used in wireless communication for DAC and ADC purposes. The impact of the RCPSF on the PAPR values of both schemes was also simulated, and the results are presented in Figure 6.5 for β of 0 and 1. The results show that the PAPR of both schemes increases as β increases (note that, the out-of-band radiation increases by decreasing β). In addition, it can be seen that for $\beta =$ 1, the PAPR of both schemes is increased by around 2.2 dB.
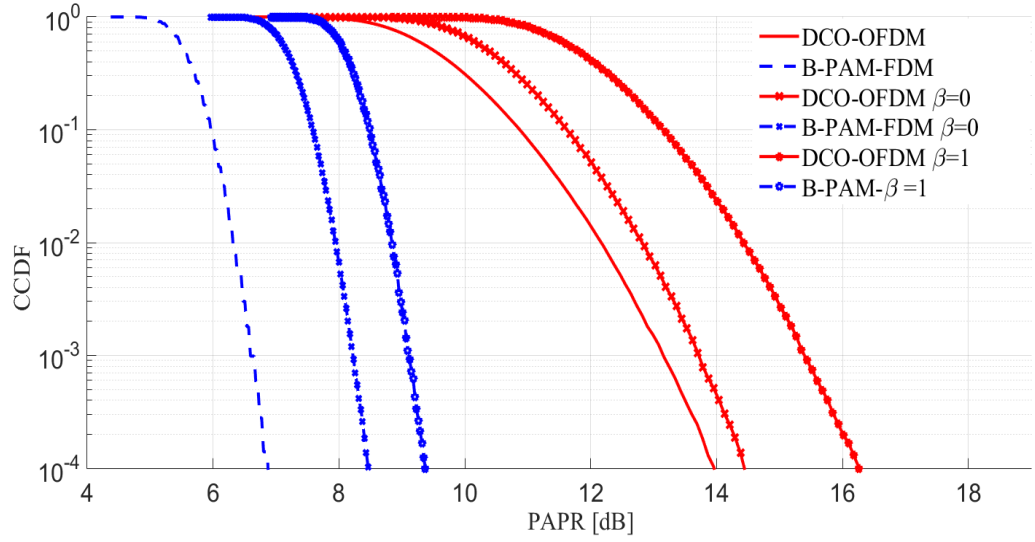
Figure 6.5 CCDF vs. PAPR of DCO-OFDM and B-PAM-FDM, for β=0 and β=1, where the number of IFFT points = 256

As previously discussed, in VLC systems, P_{avg} of the OFDM scheme is limited by the dynamic range of the LED, which can affect the VLC system performance, since a lower P_{avg} leads to a lower SNR (i.e., leads to a shorter distance between the Tx and the Rx and/or lower constellation mapping order). Figures 6.6, 6.7 and 6.8 depicts the maximum transmitted average power (P_{max}) that can be achieved by the two aforementioned schemes. Note that, P_{avg} of both schemes was varied from 0 dBm to 25 dBm in the simulations, and the EVM was simulated at each P_{avg} value, where P_{max} is predicted to occur for EVM=12.5%, as the system performance begins to deteriorate after this EVM% value [152]. Figures 6.6 and 6.7 illustrate the 16 QAM constellation points of the DCO-OFDM and B-PAM-FDM schemes, respectively for EVM = 12.5%, where only the clipping noise was considered (i.e., no AWGN) in the simulations, and the DC-bias of both schemes was set to be at the centre point of the LED dynamic range (note that, the dynamic range of the LED in these simulations was 1 V). In these figures, P_{avg} of the DCO-OFDM and B-PAM-FDM schemes are 20.42 dBm and 22.32 dBm respectively (i.e., B-PAM-FDM provides approximately 2 dBm more P_{avg} in comparison to DCO-OFDM, when only the clipping noise is considered). Furthermore, Figure 6.7 shows that the clipping noise in B-PAM-FDM is a linear noise, which might be easy to estimate, as it can be investigated in our future work.

121
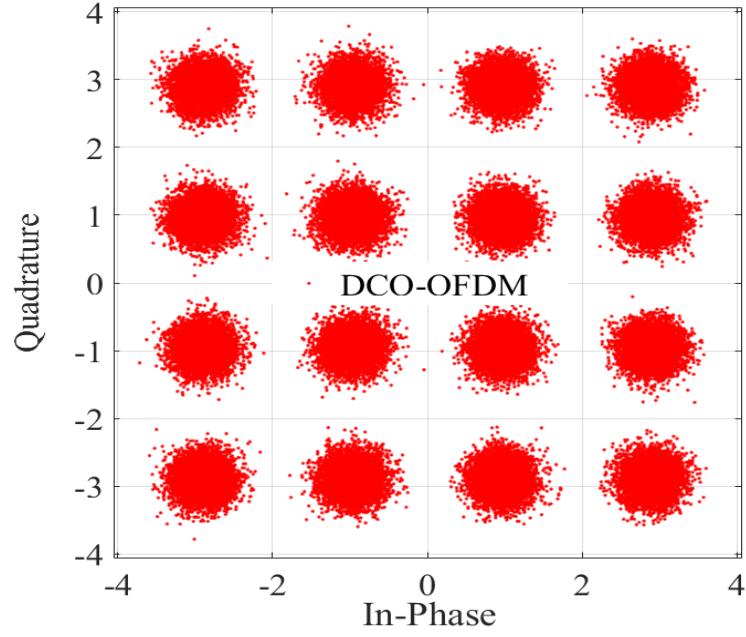
Figure 6.6 The 16 QAM constellation points of the DCO-OFDM scheme, where $P_{avg} = 20.42$, EVM%=12.5%, LED dynamic range = 1V, and only the clipping noise is considered (i.e. no AWGN
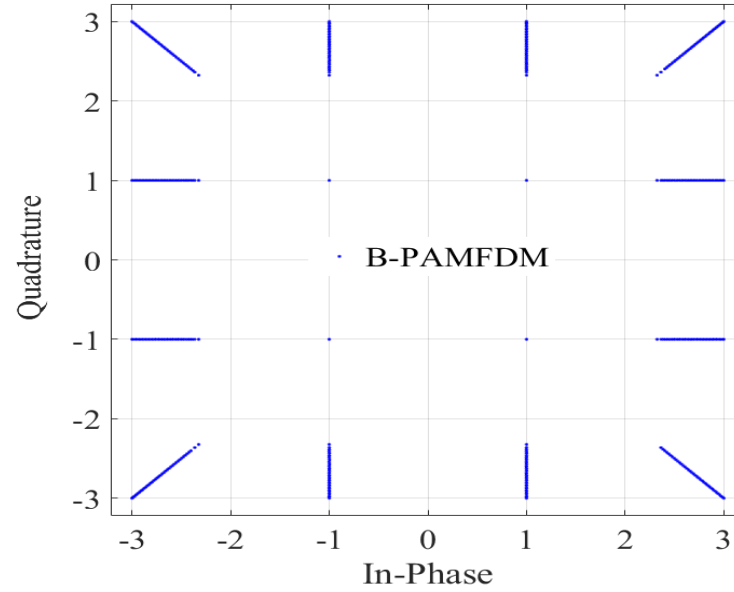
Figure 6.7 The 16 QAM constellation points of B-PAM-FDM, where $P_{avg} = 22.32$, EVM%=12.5%, LED dynamic range = 1V, and only the clipping noise is considered (i.e. no AWGN)

Since AWGN increases the EVM, P_{max} will be affected by the amount of AWGN present in the system. In [23], the AWGN value was set to -10 dBm. However, the AWGN in VLC systems varies within a range, as it depends on numerous parameters (Chapter 3, subsection 3.2.5.1). In Figure 6.8, the AWGN is varied from -15 dBm to 0 dBm, and P_{avg}

of both schemes is evaluated at each AWGN value to identify P_{max}, which as previously mentioned, is achieved when EVM = 12.5%. From this figure, one can observe that increasing AWGN decreases the P_{max} value of both schemes, as the EVM becomes more sensitive to the clipping noise by increasing the AWGN level.

An additional observation is that made from figure is that, for a 1 V LED dynamic range, the 16-QAM DCO-OFDM signalling scheme can only be implemented when AWGN < -6 dBm, as greater AWGN values result in increasing the EVM beyond the 12.5% level. However, 16-QAM-B-PAM-FDM can tolerate higher AWGN levels, as it can be implemented using the same given parameters for AWGN < -2.5 dBm. Furthermore, the figure also demonstrates that the 16-QAM B-PAM-FDM scheme outperforms the 16-QAM-DCO-OFDM scheme for all AWGN levels in term of transmit power efficiency.
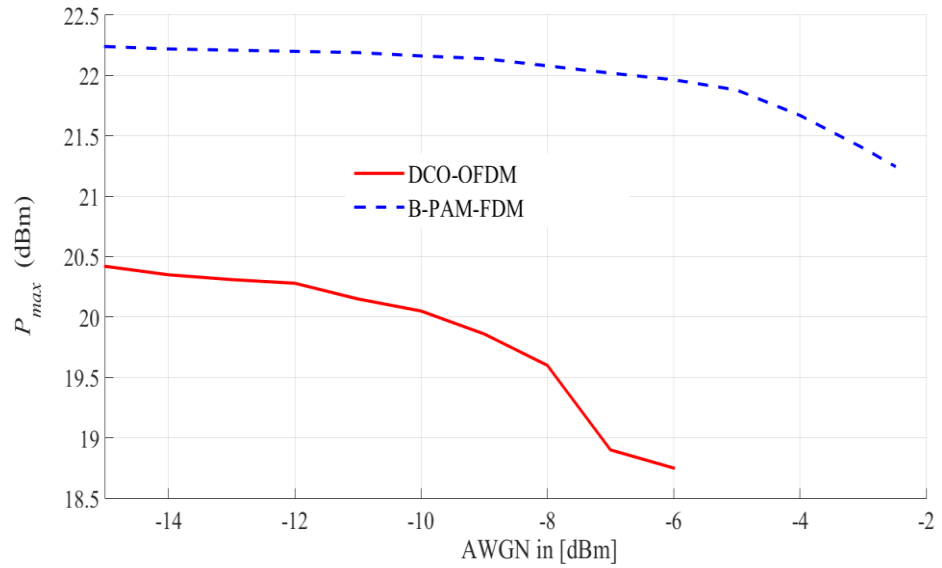
Figure 6.8 P_{max} vs. AWGN of the DCO-OFDM and B-PAM-FDM schemes, when the DC-bias is set in the middle of the LED dynamic range

Finally, since LEDs are mainly used for illumination purpose, controlling the brightness of LEDs should be taken in a consideration in VLC systems. One straightforward method used to control the brightness of LEDs is to adjust the DC-bias level [10, 161]. However, increasing or decreasing the DC-bias level results in increasing the upper or lower clipping noise of the bipolar OFDM schemes respectively. Note that, in Figure 6.8 above, the DC-

bias was set to be at the middle point of the LED linear range, thus providing a fixed illumination level. In order to study the effect of the brightness control on the system performance of 16-QAM B-PAM-FDM and 16-QAM DCO-OFDM, the DC-bias level was set at the first and third quarter points of the LED linear range, thus providing three dimming control levels in contrast with Figure 6.8.

The effect of setting the DC-bias at the first and third quarter points of the LED dynamic range on the system performance of the two schemes is illustrated in Figures 6.9 and 6.10 respectively. However, as both schemes are bipolar OFDM schemes, in Figure 6.9, the system performance of both schemes is mostly affected by the lower clipping noise, while in Figure 6.10, the upper clipping noise is the dominant clipping noise for both schemes. Furthermore, setting the DC-bias at the first quarter point of the LED linear range provides the same performance as setting it at the third quarter point. This is due to the fact that both schemes have a normal Gaussian distribution shape (i.e., the lower clipping noise in Figure 6.9 is the same as the upper clipping noise in Figure 6.10). In addition, from these figures, it can be observed that setting the DC-bias at these two points of the LED linear range makes the DCO-OFDM and B-PAM-FDM schemes only valid (i.e., EVM > 12.5%) for AWGN of < -13 dBm and < -10 dBm, respectively.

Furthermore, increasing of the AWGN level results in decreasing P_{max} from 16.4 dBm to 15.8 dBm, and from 15 dBm to 14.3 dBm, for 16-QAM B-PAM-FDM and 16-QAM DCO-OFDM respectively. Note that, dimming control can also be achieved in VLC systems by controlling the pulse samples duration [6, 162]. However, since the odd samples in B-PAM-FDM do not carry any data, the duration of the even samples of this scheme have more flexibility to be adjusted according to the required illumination level, as will be demonstrated in our future work.
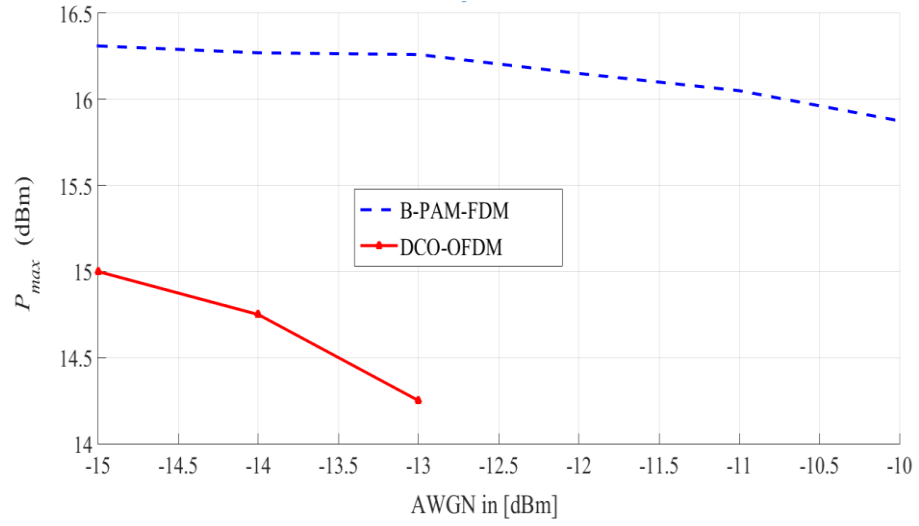
Figure 6.9 P_{max} vs. AWGN of the DCO-OFDM and B-PAM-FDM schemes, when the DC-bias is set at the first quarter of the LED dynamic range
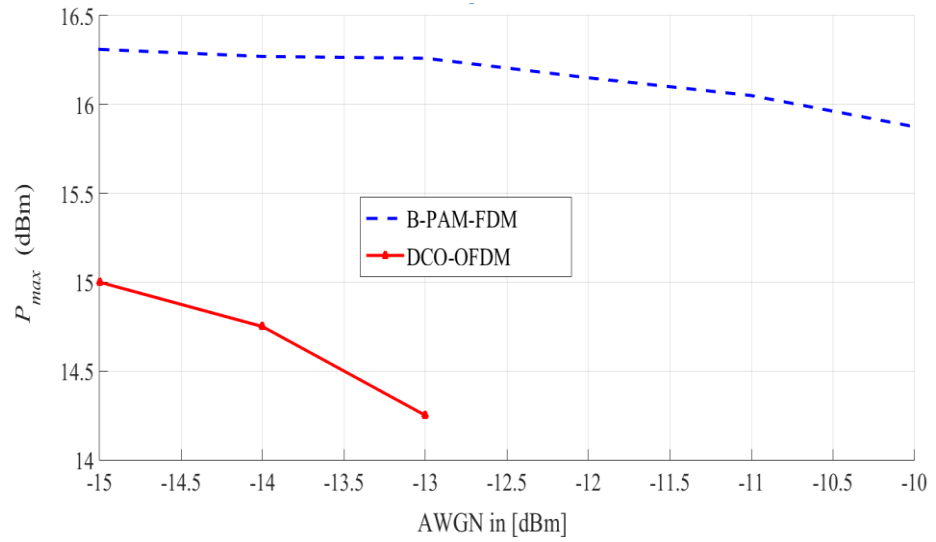
Figure 6.10 The P_{max} vs. AWGN of the DCO-OFDM and B-PAM-FDM schemes, when DC-bias is set at the third quarter of the LED dynamic range

b) **Experimental investigation**

The main aim of this experimental study was to implement the B-PAM-FDM signalling scheme in real time using the USRP N210 transceiver, and practically prove how its low PAPR makes it outperforms DCO-OFDM in terms of providing more P_{max}, and thus increasing the distance between the Tx and Rx. The experimental setup diagram and the hardware are shown in Figures 6.11 and 6.12, respectively where the same LED, PD, USRP, TC-bias circuit, LED driver, Gigabit switch, Gigabit Ethernet cables used in Chapter 5,

subsection 5.3.2, were used in this experiment. As mentioned in the earlier Chapter, limited number of bits were used in this experimental setup to practically support the illustrated theory of the proposed B-PAM-FDM scheme due to the time limitation. However, more bits will considered in our future work.
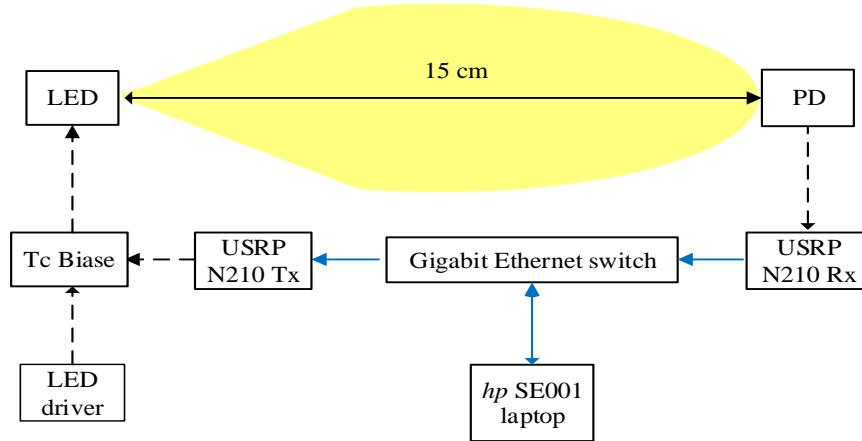
Figure 6.11 Experimental setup diagram.

Figure 6.12 A photograph of the experimental hardware (Northumbria university research Lab)

As the two aforementioned schemes are bipolar schemes, to ensure operation in the linear region, the LED was biased at the middle point of its dynamic range (i.e., at 500 mA), providing 1 V peak to peak voltage (see Figure 6.13 for the measured L-I-V curves).
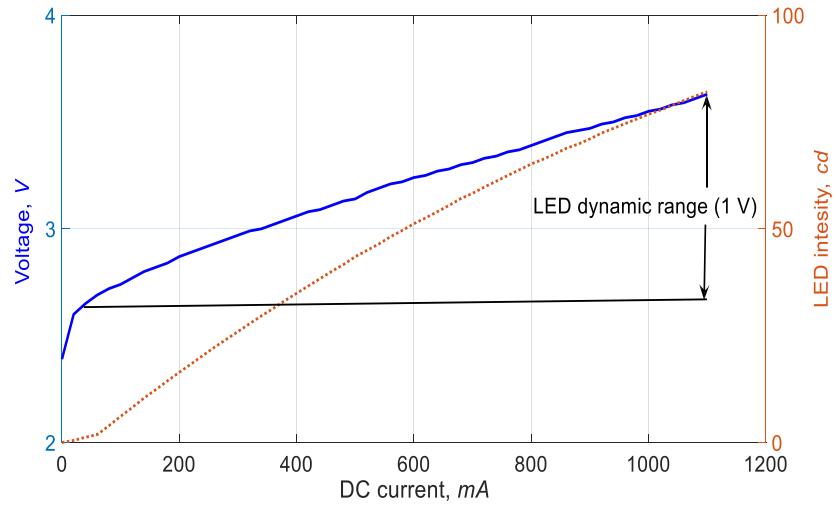
Figure 6.13 Measured L-I-V curves of the 1W white LED
(HPB8-49KxWDx) used in this work.

Note that, the USRP transceiver was interfaced and controlled by a laptop through LabVIEW software. The main Tx and Rx parameters used are presented in Figures 6.14 and 6.15, respectively.
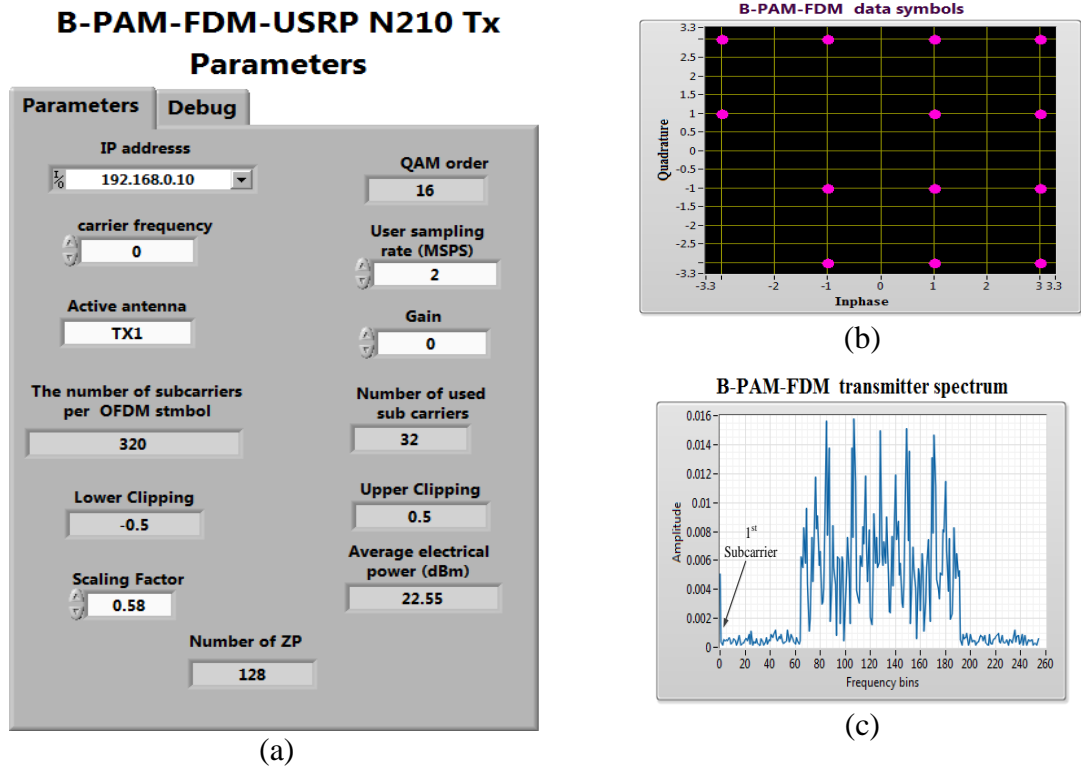
Figure 6.14 LabVIEW control panel of the USRP Tx of B-PAM-FDM, where plots (a), (b) and, (c) depict the B-PAM-FDM Tx parameters, the B-PAM-FDM transmitted symbols, and the B-PAM-FDM transmitted spectrum, respectively.

B-PAM-FDM USRP N210 Rx Parameters

Parameters | Debug

IP addresss
192.168.0.10

carrier frequency
0

Active antenna
RX1

Number of recieved OFDM blocks
1000

Number of subcarriers per OFDM symbol
320

QAM order
16

User sampling rate (MSPS)
2

Gain
0

Number of OFDM symbols per block
4

Number of CP samples
64

Number of ZP
128

(a)

Recieved B-PAM-FDM data symbol

(b)

B-PAM-FDM recieved SPECTRUM
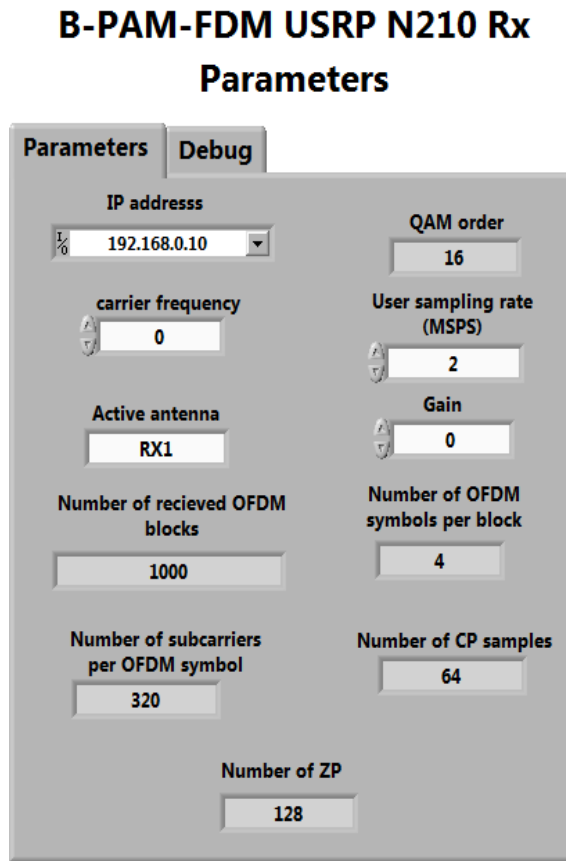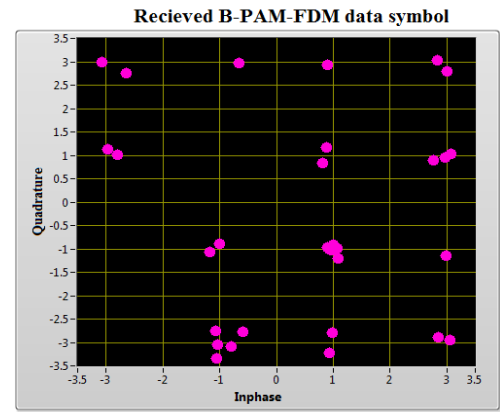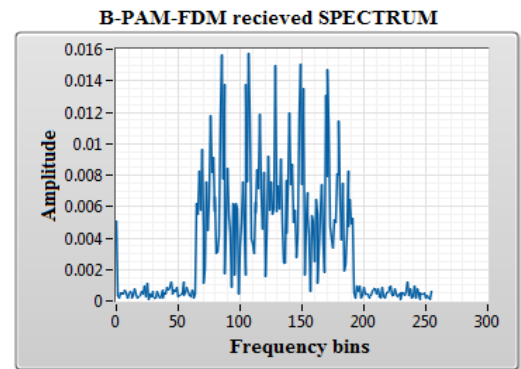
(c)

Figure 6.15 LabVIEW control panel of the USRP Rx of B-PAM-FDM. Note that, the 16-QAM constellation points in (b) were captured at EVM = 10.2%)

At the Tx, 128 and 256 bits were randomly generated, separately mapped to 16-QAM, saved and used to implement the B-PAM-FDM and DCO-OFDM schemes respectively (i.e., 32 and 64 complex data symbols for B-PAM-FDM and DCO-OFDM respectively). Note that, for B-PAM-FDM, the imaginary and the real parts of the complex data symbols were separated to provide 64 real symbols before going through the FFT process. As in LTE [154, 155], the two schemes were zero padded to enhance their spectrum shape, at the cost of the available bandwidth. The ZP insertion technique was implemented by adding a number of zeros at the edges of the subcarriers, before being passed to the IFFT process, as illustrated in Figure 6.16.
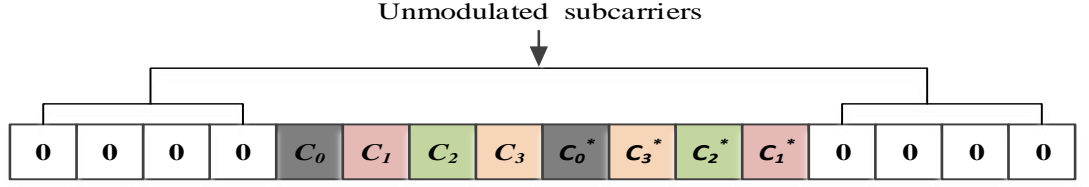
Figure 6.16 B-PAM-FDM subcarriers after inserting 8 zeros at both edges (note that in this figure, the number of subcarriers before ZP is 8)

Unlike DCO-OFDM, in B-PAM-FDM, the first and middle subcarriers are not zeroes. This is because adding a number of zeros at the edges of the subcarriers results in imaginary IFFT output samples unsuitable for IM/DD, as the middle and first subcarriers will not be conjugated (see Figure 6.16). To keep the IFFT output samples of B-PAM-FDM real after the ZP insertion method, the first B-PAM-FDM subcarrier was shifted to the beginning, as illustrated in Figure 6.17 (for further clarification, see the B-PAF-FDM spectrum in Figure 6.14).
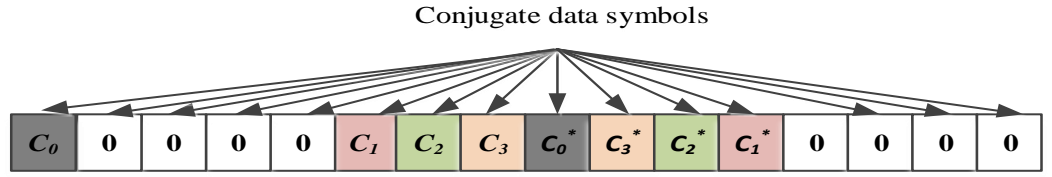
Figure 6.17 The B-PAM-FDM subcarriers after shifting the first subcarrier to the beginning

At the Rx, the light signal was detected and converted back to an electrical signal by the PD, and sent through an SMA cable, USRP Rx, Ethernet cable, Gigabit Ethernet switch and Ethernet cable to the laptop as a baseband digital signal for signal processing and analysis (see Figures 6.11 and 6.12). 1000 OFDM blocks at each P_{avg} value of the two OFDM schemes were received and processed online. Note that, every OFDM block had 4 OFDM time domain symbols, and each symbol consisted of 320 subcarriers (i.e., 320 OFDM subcarriers were transmitted 4000 times at each P_{avg} value, where the average result was considered). The ML algorithm was applied in this experimental work to each OFDM block for synchronisation and frequency-offset correction purposes, by investigating the length of the CP samples (64 samples were used as CP in this work), as shown in Figures 6.18 (Chapter

129

2, subsection 2.3.6). Following implementation of the ML algorithm, each OFDM time domain symbol was fed to the FFT process, where the redundant output subcarriers (i.e., the zero-padded and conjugate subcarriers for the DCO-OFDM scheme and the ZP and repeated subcarriers for B-PAM-FDM scheme) were rejected. Note that, because of the RM process, the first B-PAM-FDM subcarrier affected by DC-bias was replaced by the middle subcarrier in this work.

(a)

(b)
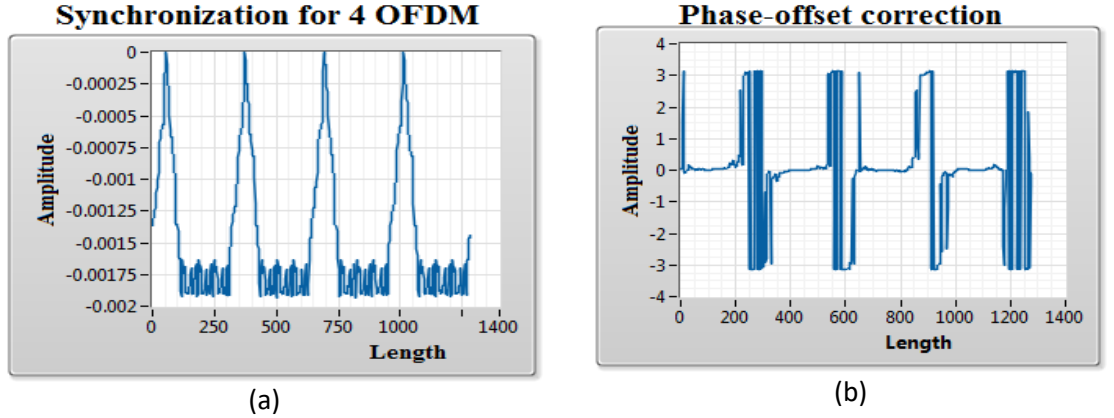
Figure 6.18 ML algorithm applied to an OFDM block to achieve: (a) synchronisation estimation, and (b) frequency-offset estimation

However, as the received OFDM subcarriers carried known data, 8 subcarriers from each OFDM time domain symbol were used to estimate the system transfer function using a Comp type estimation method (Chapter 2, subsection 3.4). After estimating the system transfer function, the ZF algorithm was implemented to equalize the OFDM data symbols (Chapter2, subsection 2.3.5). Finally, the transmitted bits of DCO-OFDM and B-PAM-FDM were reconstructed from the equalized data symbols and saved to be processed offline by a MATLAB program for BER and EVM assessment.

c) Experimental results

P_{max} of the DCO-OFDM and B-PAM-FDM schemes was experimentally evaluated by measuring the EVM at each P_{avg} value within the range $0 \leq P_{avg} \leq 24$ (note that, $P_{max} = P_{avg}$ when EVM = 12.5%). Furthermore, the benefit of the P_{max} penalty was investigated by increasing the distance between the Tx and the Rx (de).

Figure 6.19 plots the EVM vs. P_{avg} of the 16-QAM DCO-OFDM and 16-QAM B-PAM-FDM schemes for $de = 15$ cm. The figure shows that for $P_{avg} \leq 18$ dBm, the EVM% of both schemes decreased by increasing P_{avg}, since the SNR is increased. However, for $P_{avg} > 18$ dBm, the EVM of DCO-OFDM started increasing and the system performance started to deteriorate, as the linear range of the system was no longer applicable at this value. On the other hand, the system performance of B-PAM-FDM started to deteriorate due to the clipping noise when $P_{avg} > 22$ dBm. The figure also demonstrates that the measured P_{max} of the DCO-OFDM and B-PAM-FDM was 20.5 dBm and 22.5 dBm respectively (i.e. the B-PAM-FDM provided 2dBm more P_{avg} in comparison to DCO-OFDM). Furthermore, for $P_{avg} < 18$ dBm, DCO-OFDM required around 3dB more SNR in comparison to B-PAM-FDM to achieve the same EVM % levels, since the odd samples do not carry any data in the B-PAM-FDM scheme.
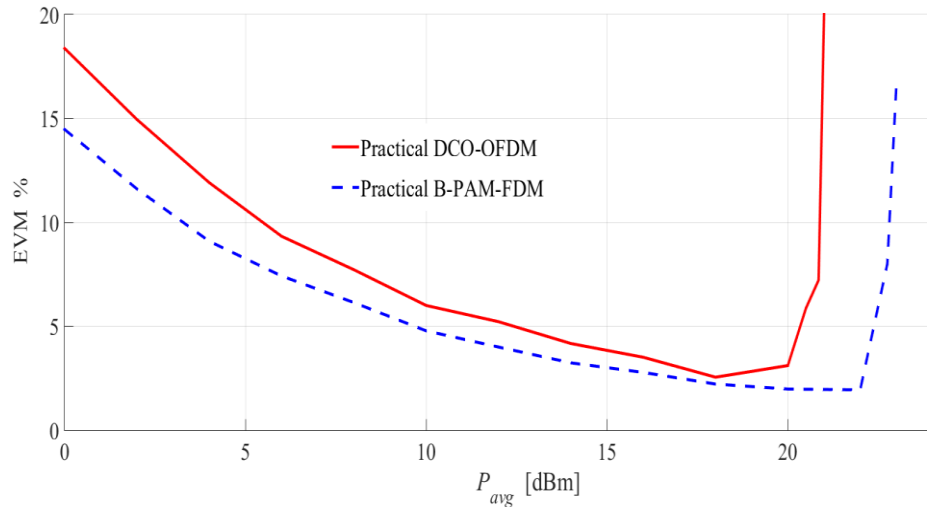
Figure 6.19 The EVM% vs. P_{avg} for 16 QAM DCO-OFDM and 16 QAM B-PAM-FDM.

Following the previous discussions, higher P_{avg} values result in increasing the distance between the Tx and Rx. To determine the maximum achievable distance between the Tx and Rx (d_{max}) for both schemes, P_{avg} of both schemes should be set at P_{max}, de should be increased progressively, and the EVM % should be measured at each de value, where d_{max}

is achieved when EVM % = 12.5% (Note that P_{max} in Figure 5.19 occurs for de = 15 cm). However, as already discussed in the simulation results (see Figure 6.8), decreasing the SNR value (i.e., increasing de) reduces P_{max}. As such, for de > 15 cm, a lower P_{max} should be used (i.e., lower than 20.5 dBm and 22.5 dBm for DCO-OFDM and B-PAM-FDM respectively). In this investigation, P_{avg} values of 20.25 dBm and 22.25 dBm, which occurred in Figure 6.19 for de = 15 cm when EVM % = 7.5%, were considered as the optimum average power (P_{opt}) levels for the DCO-OFDM and B-PAM-FDM schemes respectively, as they can be used for a range of SNR values (i.e., for a range of distances).

In Figure 6.20, P_{avg} of each scheme was set to its P_{opt}, de was varied within the range 15 cm $\le de \le$ 70 cm, and the EVM % was measured after every 2 cm. From this figure, it can be seen that the EVM % of DCO-OFDM and B-PAM-FDM reach the threshold value (i.e., EVM % = 12.5%) for de = 43 cm and 63 cm, respectively. As such, implementing the proposed scheme increased de by 44% in comparison to the traditional DCO-OFDM scheme. Note that, in Figure 6.20, in order to ensure that the achieved distance is the maximum one for both schemes, P_{avg} of both schemes was kept around their P_{opt} value, and d_{max} was achieved when $P_{avg} = P_{opt}$.
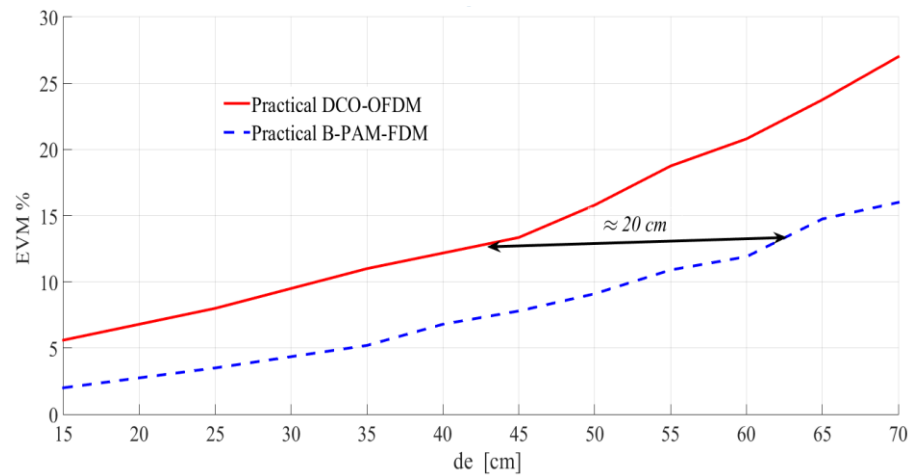
Figure 6.20 EVM% vs. de for the 16-QAM DCO-OFDM and 16 QAM B-PAM-FDM schemes, where P_{avg} of DCO-OFDM and B-PAM-FDM is 20.25 dBm and 22.25 dBm, respectively.

Finally, the BER performance of the two schemes was investigated experimentally as a function of *de*, as illustrated in Figure 6.21, where P_{avg} of both schemes was set at their P_{opt}. The figure demonstrates that for *de* < 45 cm, both schemes achieved the same BER performance (i.e., both schemes reached the noise floor), as the EVM % of the two schemes was less than 12.5% for shorter distances. However, for *de* ≥ 45 cm, the BER performance of DCO-OFDM is being affected as its SNR is dropped down and consequently the EVM % become more than 12.5% while the BER performance of the B-PAM-FDM scheme is start being affected when *de* > 65 cm, which is because the P_{avg} of the proposed scheme is around 2 dBm more than the P_{avg} of the traditional DCO-OFDM.
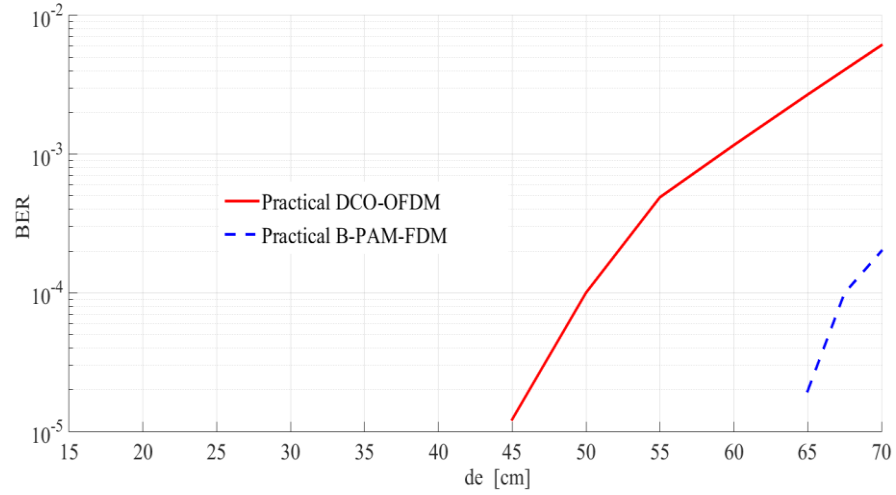
Figure 6.21 The BER vs. *de* for both 16-QAM DCO-OFDM and 16-QAM B-PAM-FDM where, P_{avg} of DCO-OFDM and B-PAM-FDM are 20.25 dBm and 22.25 dBm respectively.

Note, in Chapter 5 all the results of the unipolar OFDM schemes (i.e., ACO-OFDM, ACO-SCFDE and U-PAM-FDM schemes) are taken before zero clipping method. As such, before clipping the anti-symmetric samples of these schemes, which increase their P_{avg} value in Watt twice. However, if the odd samples (zero samples) of B-PAM-FDM are not taken into consideration (as they do not carry any data), the P_{avg} value of B-PAM-FDM in all of the pervious results will be 3 dB higher. For example, Figures 6.3, 6.4 and 6.19 will be replaced by Figures 6.22, 6.23, and 6.24, respectively as illustrated bellow.
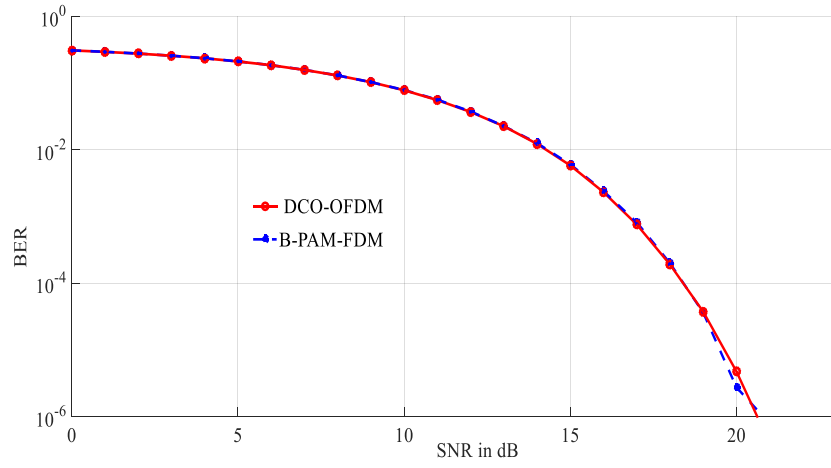
Figures 6.22 SNR vs. BER for 16-QAM DCO-OFDM and 16-QAM B-PAM-FDM
when the odd samples of B-PAM-FDM are not taken into consideration
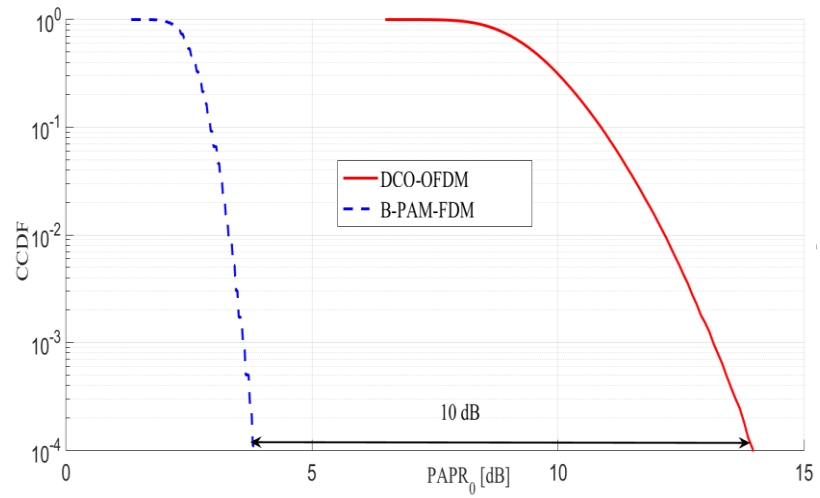
Figures 6.23 CCDF vs. PAPR of the DCO-OFDM and B-PAM-FDM schemes for
256 IFFT points, when the odd samples of B-PAM-FDM are not taken into
consideration
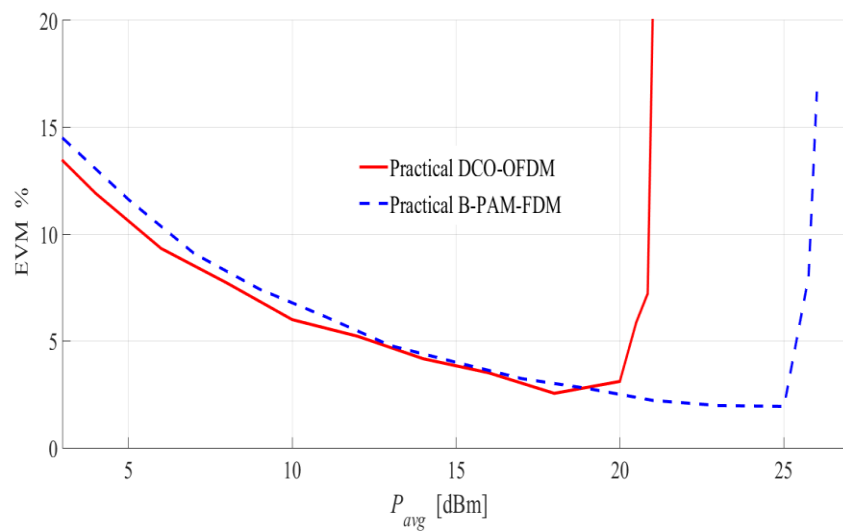
Figures 6.24 EVM % vs. P_{avg} for the 16-QAM DCO-OFDM and
16 QAM B-PAM-FDM schemes, when the odd samples of B-PAM-FDM are taken
into consideration

6.3 Optical interleaved frequency division multiplexing (OIFDM)

A novel optical interleaved frequency division multiplexing signalling scheme for IM/DD based VLC system is presented in this section as a means to significantly improve the DCO-OFDM PAPR, without reducing its spectral efficiency. The significant reduction in the OFDM PAPR value is achieved by exploiting the symmetrical characteristics of the IFDMA time domain symbol where the imaginary and real parts of the IFDMA samples are separated and transmitted through two sub-symbols.

Simulation results shows that the PAPR of the proposed scheme is 10 dB lower than the PAPR of the traditional DC-OFDM scheme. In addition, the results demonstrate that the BER performance of the proposed scheme is significantly superior to that of the DCO-OFDM scheme, when the limited dynamic range of the digital-to-analogue converter and LED are considered. Unlike in the traditional DCO-OFDM scheme, the first subcarrier in OIFDM is not zero, and can be affected by the DC-bias, which will subsequently affect all OIFDM samples in the time domain. However a simple estimation algorithm is used in this work to decrease the effect of the DC-bias at a cost of the required SNR.

6.3.1 OIFDM system description

In this section, an analysis of the proposed OIFDM system, along with a description of the Tx and the Rx structures, are presented. Furthermore, the interleaving mapping is investigated to make IFDMA applicable for IM/DD VLC systems

IOFDM Tx

Figure 6.25 depicts the block diagram of the Tx of the OIFDM scheme, which is similar to the Tx of the standard IFDMA scheme (Chapter 2, subsection 2.3.4.2). The main difference is the inclusion of the IMP block at the Tx of OIFDM, while the intensity demodulation process (IDP) block is inserted at the Rx. The signal processing steps at the Tx are described

as follows. First, the serial binary bits $b_i(t)$ are converted into parallel data streams and mapped onto a group of complex quadrature amplitude modulation (QAM) symbols $\bar{x}$, as given by:

$$\bar{x} = [\bar{x}_0, \bar{x}_1, \bar{x}_2, \dots \bar{x}_{M-1}], \tag{6.11}$$

where $\bar{x}_0, \bar{x}_1, \bar{x}_2, \dots \bar{x}_{M-1}$ refer to the kth QAM complex symbol, and M is the number of data symbols. Note that, as will be explained in detail in subsection 6.3.2, to reduce the DC-bias noise, the first symbol in $\bar{x}$ is unmodulated (i.e., $\bar{x}_0 = 0$).

The complex symbols are transformed to the frequency domain by the FFT block, and its output in the frequency domain is given by:

$$\bar{X}_m = \sum_{k=0}^{M-1} \bar{x}_k \, e^{-j2\Pi\frac{k}{M}m}, \tag{6.12}$$

where $\bar{X}_m$ refers to the mth sub carrier, $m = k = \{0,1,2, \dots \dots M-1\}$, and $\bar{X} = [\bar{X}_0 \, \bar{X}_1, \bar{X}_2 \cdots \bar{X}_{M-1}] \in \mathbb{C}^M$ denotes the set of M-dimensional complex numbers. The interleaving mapping is carried out on $\bar{X}$ by inserting $(Q\text{-}1)$ number of zeros between the adjacent sub-carriers (here $Q = 2$, see Figure 6.25). The mapped output signal is defined as follows:

$$X_i = \begin{cases} \bar{X}_m, & \text{if } i = Qm \text{ where } 0 \leq m \leq M-1 \\ 0, & \text{otherwise} \end{cases} \tag{6.13}$$

where $i = \{0,1,2, \dots N-1\}$, $X = [X_0, X_1, X_2, \dots \dots X_{N-1}]$ and $N = QM$. The mapped frequency domain signal is then converted back to a time domain signal:

$$x_n = \frac{1}{N} \sum_{i=0}^{N-1} X_i \, e^{j2\Pi\frac{i}{N}n}, \tag{6.14}$$

where x_n ($x \in \mathbb{C}^N$) refers to the nth time domain sample after the interleaving process, and $n = \{0,1,2,....N-1\}$. By letting $n = (Mq + m)$ for $0 \le q \le Q - 1$ in (6.14), we obtain [68]:

$$x_n = x_{Mq+m} = \frac{1}{N} \sum_{i=0}^{N-1} X_i \, e^{j2\Pi\frac{i}{N}(Mq+m)}$$

$$= \frac{1}{Q} \frac{1}{M} \sum_{i=0}^{M-1} X_m \, e^{j2\Pi\frac{k}{M} m}$$

$$= \frac{1}{Q} \left| \frac{1}{M} \sum_{i=0}^{M-1} X_m \, e^{j2\Pi\frac{k}{M} m} \right|$$

$$= \frac{1}{Q} x_k. \tag{6.15}$$

From (6.15), it can be clearly seen that x_n is a scaled (in amplitude) version of x_k. Indeed, x_n has the characteristics of a single carrier with a low PAPR. However, due to the interleaving mapping of $\bar{X}$ by Q, x is repeated Q-times over a given symbol period as follows (see Figure. 6.25):

$$x_n = x_{n+Q} = x_{n+2Q}, = .., = x_{n+(Q-1).Q}. \tag{6.16}$$

To make IFDMA applicable for IM/DD VLC systems, the IMP block is inserted after the IFFT process. The IMP block consists of the two following procedures: (*i*) removing the imaginary part of the first half of the OFDM symbol; and (*ii*) removing the real part of the second half of the OFDM symbol. Because of the symmetrical characteristic of x, this process does not result in any loss of information. The real bipolar output time domain samples of the IMP block are then transmitted through two sub-symbols [R, I], which are given by:

$$R = \begin{cases} \text{real } x_n, & \text{or } (n \leq M - 1) \\ 0 & \text{otherwise} \end{cases}. \tag{6.17}$$

$$I = \begin{cases} \text{imag } x_n, & \text{for } (M \leq n < 2M) \\ 0 & \text{otherwise} \end{cases}. \tag{6.18}$$

Note that this scheme can also be a unipolar OFDM scheme, at a cost of halving the spectral efficiency. This is achieved by letting $Q = 4$, which results in repeating the output IFFT time domain symbols of IFDMA four times. In this case, each time-domain OFDM symbol is divided into four sub-symbols, where the 1st, 2nd, 3rd and 4th sub-symbols carry the positive values of the real samples r_+, positive values of the imaginary samples i_+, negative values of the real samples r_-, and negative values of the imaginary samples i_- respectively, as we already demonstrated in [27]. Finally, the combined vector of these sub-symbols ($\bar{\bar{x}}$) is passed through the P/S, CP insertion, DAC, LPF, and clipping modules, before being converted to a unipolar optical signal by passing through the DC-bias and EOC blocks. Note that OIFDM is a real bipolar scheme that has as low a PAPR as that of SCM and as high a spectral efficiency as that of DCO-OFDM.
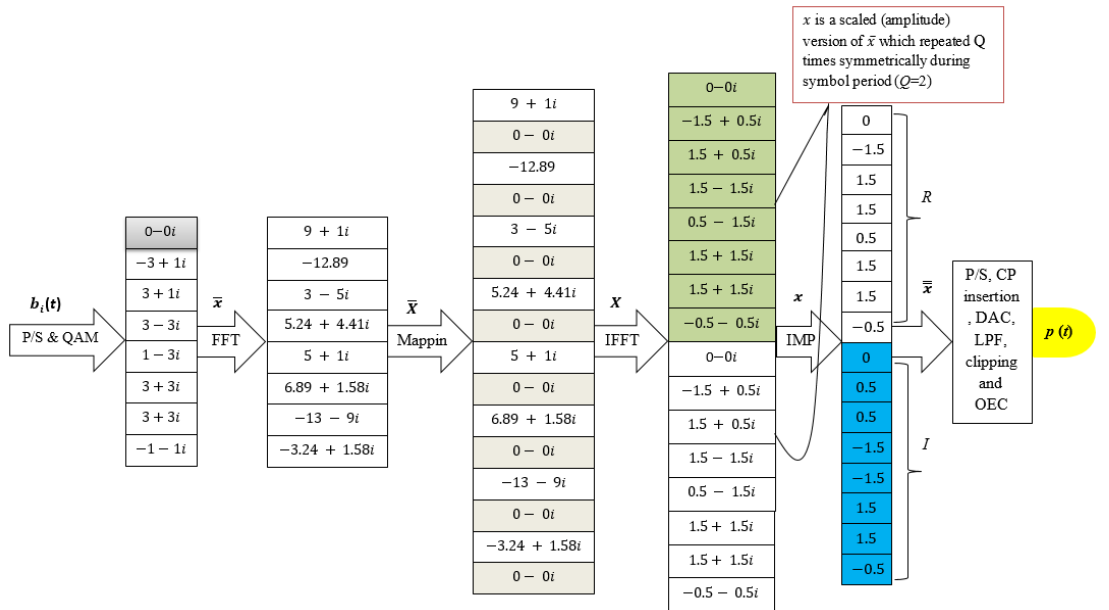
Figure 6.25 An example of the OIFDM Tx signal processing procedure

138

IOFDM Rx

Figure 6.26 shows the block diagram of the OIFDM Rx, which has the opposite functionality to that of the Tx. First, the PD detects the optical data signal and converts it back to an electrical signal $r\ (t)$, where $r(t) = \check{R}p(t) * h(t)$, $\check{R}$ is the responsivity of the PD (which is assumed to be an ideal (i.e. $\check{R}$ =1)), $h(t)$ is the impulse response of the system, and the * symbol denotes the linear convolution operation. $r(t)$ is then impacted by the shot noise and terminal noise, which can be modelled as AWGN, before being passed through the LPF, ADC, and CP removal blocks.

The resulting digital signal yc is subsequently fed to the IDMP block. In this block, the original complex and repeated samples are reconstructed (i.e., x is convoluted with the system impulse response and added to AWGN) and passed through the FFT and equalizer blocks. Three processes are carried out in the equalizer block as follows; i) de-interleaving mapping, where the un-modulated subcarriers are removed; ii) removing the effect of the system by implementing a zero forcing equaliser; and iii) converting the first subcarrier to zero to remove the effect of the DC-bias noise as well as the ambient noise. Finally, the equalised digital signal (YC) passes through the IFFT, symbols estimator, QAM de-mapping, and P/S blocks, to reconstruct the information bits. The symbols estimator process is used to estimate the symbols after converting the first subcarrier to zero, as will be explained in detail in the next subsection.
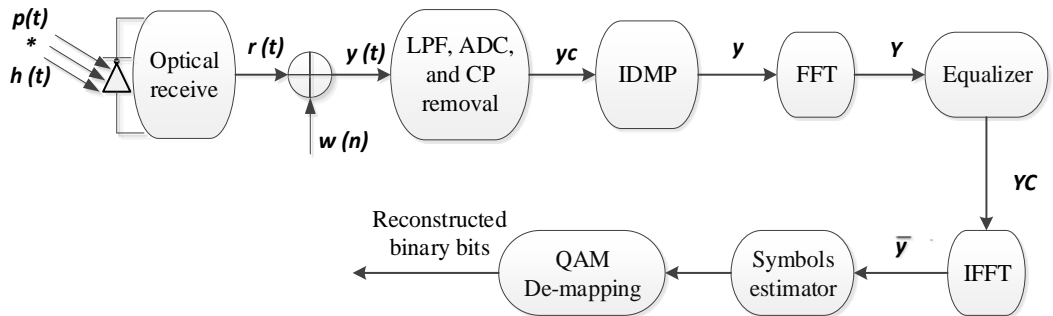
Figure 6.26 Bock diagram of the OIFDM Rx

6.3.2 DC-bias noise reduction algorithm

Because of the DC-bias and the low frequency noise (i.e., ambient noise), the first OIFDM subcarrier at the Rx will be destroyed, which can affect all OIFDM samples at the time domain. This noise is reduced in this work by un-modulating the first OIFDM symbol at the Tx (see Figure 6.25), and converting the first OIFDM subcarrier at the Rx to zero, as described below. Referring to the block diagrams of the OIFDM Tx and OIFDM Rx, the output time domain samples of the IDMP block at the Rx (y), are the output time domain samples of the IFFT block at the Tx (x), added to the DC-bias (B_{DC}) convoluted with the system impose response $h(t)$, and added to AWGN $w(n)$. In other words, $y = x + B_{DC} * h(t) + w(n)$, where $x = [x_0, x_1, x_2 \dots x_{N-1}]$, $x_0 = 0$, and x_n, which was already defined in Equation 6.14, and can be written as:

$$x_n = \frac{1}{N} \sum_{i=0}^{N-1} X_i \, e^{j2\Pi\frac{i}{N} n}$$

$$x_n = \frac{X_0 e^{j0}}{N} + \frac{1}{N} \sum_{i=1}^{N-1} X_i \, e^{j2\Pi\frac{i}{N} n.}$$

$$x_n = \left(\frac{1}{N} \sum_{i=1}^{N-1} X_i \, e^{j2\Pi\frac{i}{N} n.} \right) - \frac{X_0}{N} \tag{6.19}$$

Furthermore, without loss of generality and for the sake of simplicity, $h(t)$ and $w(n)$ are considered to be an ideal (i.e., $y = x + B_{DC}$), and therefore, only the main blocks related to the DC-bias and ambient noise are considered here, as illustrated in Figure 6.27.
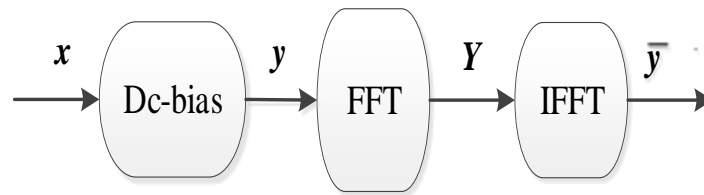
Figure 6.27 Block diagram of the DC-bias reduction algorithm

Implementing an FFT and IFFT on y results in a new time domain vector $\bar{y}$, defined by:

$$\bar{y} = \left(\frac{1}{N} \sum_{i=1}^{N-1} Y_i \, e^{j2\Pi\frac{i}{N} \, n.} \right) - \frac{Y_0}{N} \qquad (6.20)$$

Bearing in mind the FFT properties, only the first subcarrier is affected by the DC-bias and the ambient noise, since the ambient noise only affects the low frequency components (i.e., Y_0). Therefore, Equation 6.20 can be written as:

$$\bar{y} = \left(\frac{1}{N} \sum_{i=1}^{N-1} X_i \, e^{j2\Pi\frac{i}{N} \, n.} \right) - \frac{Y_0}{N} \qquad (6.21)$$

Setting $Y_0 = 0$ in (6.21) results in $x = \bar{y} - \frac{X_0}{N}$. However, since x_0 is not modulated, $\bar{y}_0 = \frac{X_0}{N}$. Finally, the transmitted symbols can be easily reconstructed as follows:

$$x_n = \bar{y}_k - \bar{y}_0 \qquad (6.22)$$

where n and k refer to the nth and k^{th} time domain samples before and after adding the DC-bias respectively.

6.3.3 OIFDM simulation results

In this simulation study, 256 IFFT points and 16-QAM were considered. The LED bandwidth was set to 4 MHz, and the CP duration was 50 ns, which is already mentioned, is the maximum time delay for an indoor VLC multipath channel. Because of the insertion of the FFT and IMP blocks before the implementation of IFFT at the OIFDM Tx, the PAPR value of the proposed scheme is 10 dB lower than the PAPR of the traditional DCO-OFDM scheme. On the other hand, in terms of SNR requirement, the proposed scheme requires more SNR compared to DCO-OFDM, when the clipping noise is not considered. This is because the fist subcarrier in OIFDM is a modulated subcarrier affected by the low frequency noise.

All simulation parameters used in this study are listed in Table 6.1.

Table 6.1 Simulation parameters

Parameter	Value
Number of iterations	1000000
The distance between LED and PD	2 m
Transmitter parameters	
LED Type	OSRAM, SFH 4230 [163]
LED turn on voltage	3 V
LED turn off voltage	4 V
LED linearity	1 V
LED half power angle $\emptyset_{1/2}$	70^0
Receiver parameters	
Cyclic prefix duration	50 ns
PD type	OSD15-5T
PD bandwidth	16 MHz
PD gain	3 dB
PD responsivity	1
PD active area	16 mm^2
Receiver field of view (FOV) (full)	180^0

Results of the CCDF vs PAPR relationship for DCO-OFDM and OIFDM are compared in Figure 6.28, where all PAPR comparisons were carried out at CCDF= 10^{-4} (Pr{PAPR > PAPR$_0$} = 0.0001). From Figure 6.28, it can be seen that the PAPR of the proposed scheme is lower than the PAPR of the traditional DCO-OFDM scheme by 10 dB. This significant improvement is due to the implementation of the FFT and interleaving mapping processes before the implementation of the IFFT process, which makes the PAPR of OIFDM as low as that of the SCM scheme.
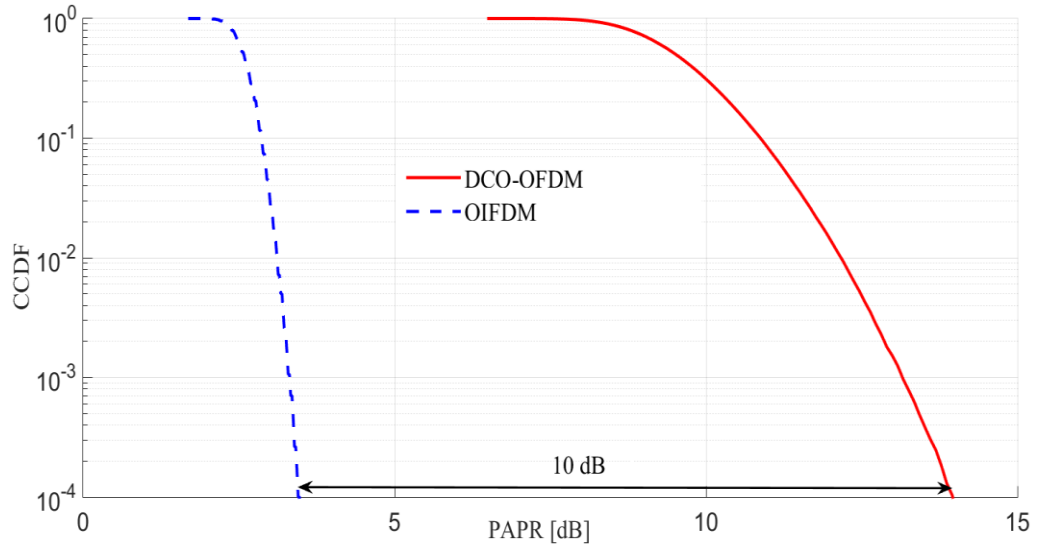
Figure 6.28 CCDF vs. PAPR for DCO-OFDM and OIFDM

The effect of PAPR on the BER performance of both schemes was also simulated, and the results are presented in Figures 6.29 and 6.30, where the dynamic range of the DAC and the dynamic range of the LED were considered respectively.

Figure 6.29 plots the BER performance as a function of DAC dynamic range (DACDR) for the DCO-OFDM and OIFDM schemes, where only the quantization noise was considered (i.e., no AWGN or DC-bias noise were considered in the simulations), and the signal power was set to 10 dBm. The DACDR in dB is calculated by DACDR= $20 \log(2^C - 1)$ where C is the DAC bit resolution (for example, USRP N210 has a DAC of 16 bits resolution) [164]. From Figure 6.29, it can be seen that the BER performance of both schemes improves by increasing the DACDR. This is because the quantization level increases by increasing C, at the cost of the required memory. However, both schemes reach the floor noise at different DACDR levels, where the traditional DCO-OFDM scheme requires ~24 dB of DACDR to reach the floor noise, while the OIFDM scheme requires ~10 dB of DACDR.

Note that since the main aim of this figure is to show the effect of DACDR for both schemes (i.e. no AWGN is added and the transmitted signal power is set to fixed value (i.e. 10dBm)), the DACDR of the presented figure are limited.
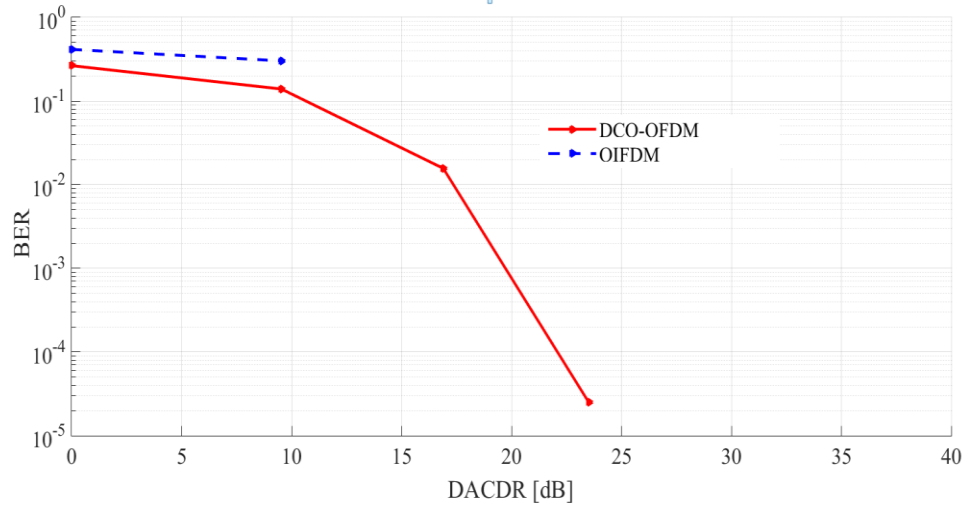
Figure 6.29 DACDR vs. BER for DCO-OFDM and OIFDM, where only the quantization error is considered as the system noise

Finally, Figure 6.30 plots the BER performance as a function of P_{avg} for the two schemes, considering an LED with a limited dynamic range. In order to observe the effect of the limited dynamic range of the LED as well as the DC-bias noise on the BER performance, a high DACDR value is assumed (i.e. DACDR = 83 dB as in the USRP N210 module [156]). In the simulations, the dynamic range of the LED was set to 1V, B_{DC} was set to 3.5 V, P_{avg} of both schemes was varied from 0 dBm to 25 dBm, and the noise power (σ_n^2) was set to -10 dBm. As such, the SNR varied from 10 dB to 35 dB, which is within the reported SNR range of the indoor VLC systems [134].

The results show that for both schemes, when the average power of the electrical signals < 21 dBm (i.e., SNR < 31 dB), we observe no clipping distortion, as only the AWGN and DC-bias noise are the main dominant noise sources at this range. Furthermore, at these P_{avg} levels (i.e., $P_{avg} < 21$), the traditional DCO-OFDM scheme outperforms the OIFDM scheme, due to the fact that the low frequency noise (i.e., the ambient noise and DC-bias noise) only affects the OIFDM scheme, since its first subcarrier is a modulated subcarrier. However, for $P_{avg} \geq 21$ dBm, the OIFDM scheme outperforms the traditional DCO-OFDM scheme, as the BER performance of the latter starts to be affected by the clipping noise when

$P_{avg} = 21$ dBm, while the BER performance of the former starts to be affected by the same noise source when $P_{avg} = 24$ dBm (i.e. OIFDM provide 3 dBm more P_{avg} in comparison to DCO-OFDM).
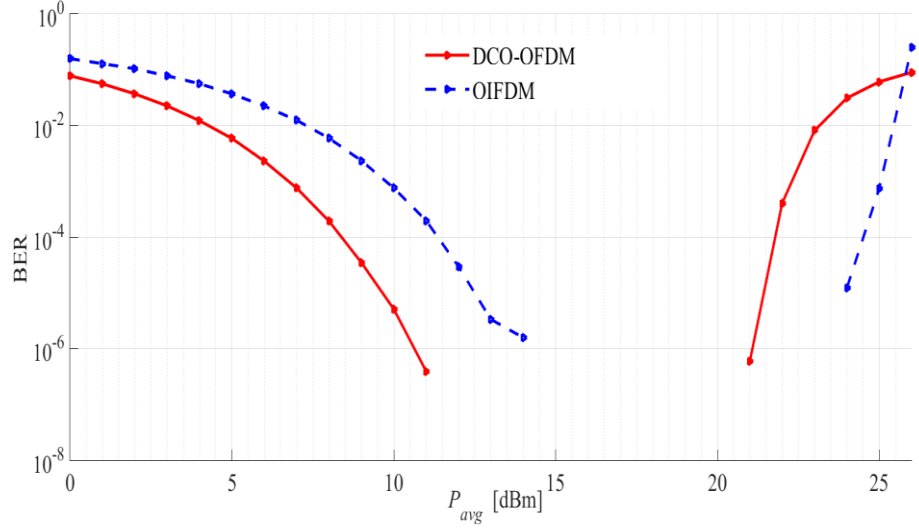
Figure 6.30 BER performance against P_{avg} for DCO-OFDM and IOFDM

6.4 summary

Two new bipolar OFDM schemes, named B-PAM-FDM and OIFDM, were introduced in this chapter as a means to significantly improve the PAPR of the OFDM signal in IM/DD based VLC systems, by making IFDMA scheme suitable for IM/DD. This IM/DD compatibility is achieved in B-PAM-FDM by replacing the interleaving mapping block in the IFDMA Tx by the RM block, and using PAM as a modulation scheme. As such, the output time domain samples of the IFFT are bipolar real samples that have as low PAPR as that of the SCM scheme. The simulation results of B-PAM-FDM were presented in subsection 6.2.2, and showed that the PAPR value of B-PAM-FDM is 7 dB lower than the PAPR value of the traditional DCO-OFDM scheme. The results also showed that the DCO-OFDM requires 3 dB more SNR in comparison to B-PAM-FDM to achieve the same BER performance.

The impact of this PAPR reduction on the system performance was experimentally investigated in subsection 6.2.2, where the results showed that the maximum achieved distance between the Tx and Rx was increased by 44% when the B-PAM-FDM scheme was implemented compared to DCO-OFDM. However, because of the RM process, and due to the fact that the imaginary part of the symbol does not carry any data, the B-PAM-FDM scheme has half the spectral efficiency of the DCO-OFDM scheme (i.e. the same spectral efficiency as the ACO-OFDM and PAM-DMT schemes). However, the spectral efficiency of B-PAM-FDM can be made as high as that of the DCO-OFDM scheme using the TDM method. In addition, the odd B-PAM-FDM time domain samples that not carry any data can be utilised in other VLC applications such as illumination, dimming control, localizations and positioning applications. Furthermore, due to the presence of the RM block, any affected subcarrier in B-PAM-FDM can be easily compensated.

In OIFDM, the symmetrical time domain characteristics of IFDMA were exploited for IM/DD VLC system applications, by symmetrically repeating the IFDMA time domain samples twice during each IFDMA time domain symbol period, which was achieved by setting the interleaving mapping factor at the frequency domain to 2. The simulation results of the OIFDM scheme were presented in subsection 6.3.3, demonstrating that the PAPR value of the proposed scheme is 10 dB lower than that of the DCO-OFDM scheme. The impact of reduced PAPR on the system performance was also simulated, while considering the effect of dynamic range of the digital-to-analogue converter (DACDR) and the LED. The results showed that the DACDR performance is enhanced by almost 14 dB when the OIFDM scheme is considered in comparison to DCO-OFDM. Furthermore, when considering the dynamic range of the LED, the results showed that OIFDM provides 3dBm more P_{avg} in comparison to DCO-OFDM. However, the simulation results also showed that, when the clipping noise is not considered, the DCO-OFDM scheme outperforms the OIFDM

scheme, due to effects of the low frequency noise, which only impact the OIFDM scheme, since its first subcarrier is modulated.

CHAPTER 7

CONCLUSIONS AND FUTURE

WORK

7.1 Conclusions

The main aim of this research work was to enhance the performance of the OFDM modulation scheme in IM/DD based VLC systems. This thesis began reporting this work by providing a general overview of OFDM systems in Chapter 1, where the basic theory behind the OFDM scheme, OFDM channel estimation, and OFDM equalization was presented, and the advantage and disadvantages of OFDM were discussed. The basic theory behind VLC systems and their main challenges were introduced in Chapter 2, and the most popular OFDM schemes used in VLC systems were highlighted in detail in this chapter.

In order to improve the performance of OFDM signals, and subsequently contribute towards addressing some of the challenges presented in Chapter 2, five new modified optical OFDM schemes were introduced in Chapters 4, 5 and 6 of this thesis, as summarised below.

As the first aim of this research work was to increase the ACO-OFDM data rates, and subsequently provide a trade-off between the low data rates of ACO-OFDM and the low power efficiency of DCO-OFDM, PA-ACO-OFDM and PE-ACO-OFDM were introduced in Chapter 4 to improve the ACO-OFDM data rates by up to 33%. This data rate enhancement was demonstrated by exploiting the asymmetrical characteristic of the time domain symbol of ACO-OFDM, where only the first half of the symbol was used to carry

the data samples, while the second half was rejected. Because of the IM/DD requirements, the negative samples of the used ACO-OFDM symbol were inverted to positive ones. These inverted samples were detected at the receiver and converted back to negative ones by inserting higher amplitude pilots at the Tx (as in PA-ACO-OFDM), or by encoding the positions of the negative and positive samples using the QAM constellation order (as in PE-ACO-OFDM). However, inserting higher amplitude pilots in a large PAPR signal, such as an ACO-OFDM signal, and subsequently passing the signal through the limited LED dynamic range, makes PA-ACO-OFDM only suitable for low SNR applications. On the other hand, the data rates of PE-ACO-OFDM increase by increasing the encoded QAM constellation order, thus making the scheme only applicable for high SNR applications.

Following the previous discussion, the implementation of the OFDM scheme in VLC systems is therefore limited by the SNR value, which is a result of the large OFDM PAPR. As such, reducing the PAPR of the optical OFDM signal was the second aim of this research work. This was achieved by adapting the IFDMA RF signal in there different ways, resulting in three new modified OFDM schemes suitable for IM/DD based VLC systems.

In the first modified scheme (U-PAM-FDM (Chapter 3)), the output FFT subcarriers of the IFDMA Tx were conjugated symmetrically around the middle subcarrier except the first one, by making its data symbols real (i.e. PAM). Two other subcarriers were added after the FFT process to make all output subcarriers symmetrically conjugated, subsequently resulting in an asymmetrical real time domain signal suitable for IM/DD. However, although the simulation and experimental results showed that the PAPR of ACO-OFDM and its negative impact on the system performance were reduced when this scheme was implemented, the PAPR of U-PAM-FDM was found to be still higher than the PAPR of IFDMA. This is because adding two new subcarriers after the FFT process resulted in preventing some subcarriers from enjoying the interleaving mapping feature.

Chapter 6, section 6.2 presented the second IFDMA adaptation method, which was achieved by introducing the B-PAM-FDM scheme. To make the even IFFT output time domain

samples of the IFDMA Tx the same as its data symbols, and its odd samples zeros, the output FFT vector of the IFDMA Tx was duplicated in this scheme instead of implementing interleaved mapping like in IFDMA. As such, making the data symbol of B-PAM-FDM real (i.e., PAM) resulted in a bipolar real signal with as low a PAPR as that of IFDMA RF, making it suitable for IM/DD. The experimental results presented in Chapter 6, subsection 6.2.2, showed that the distance between the Tx and Rx was increased by 44% when B-PAM-FDM was implemented compared to DCO-OFDM, due to the PAPR of B-PAM-FDM being 7 dB lower compared to DCO-OFDM (as demonstrated in the simulation results of subsection 6.2.2). Note that since the imaginary parts of B-PAM-FDM data symbols are not utilised, the spectral efficiency of this scheme is a half that of the DCO-OFDM scheme (i.e., the same spectral efficiency of the ACO-OFDM and PAM-DMT schemes).

Finally, in Chapter 6, section 6.3, in the last adapted IFDMA scheme (OIFDM), the interleaving mapping of the IFDMA signal was exploited by setting the interleaving mapping factor to 2, to duplicate its output IFFT time domain vector during each symbol duration. To meet the IM/DD requirements, the imaginary parts were removed from the first half of this vector, while the real parts were removed from the second half. As a result, a new scheme with as low a PAPR as that of IFDMA, and with as high a spectral efficiency as that of DCO-OFDM was realised. However, because the first OIFDM subcarrier is not zero, this scheme requires ~2.5 dB higher SNR to achieve the same BER performance as the DCO-OFDM scheme.

7.2 Future work

Although extensive research has been undertaken in this thesis, a number of issues and challenges related to this research area have not yet been addressed, and may be worth investigating in future. The following future research recommendations are therefore proposed:

- **B-PAM-FDM features investigation:** The unused odd time domain samples in the B-PAM-FDM scheme need to be exploited to double its spectral efficiency by implementing TDM technique. Alternatively, a demonstration of utilising these unused samples in other applications such as illumination, localization and positioning, and time domain synchronization, needs to be implemented.

- **OIFDM DC-bias noise:** Although a new simple algorithm was introduced in this thesis to reduce the DC-bias noise in the OIFDM scheme, further investigations are needed to improve this algorithm, as the simulation results showed that approximately 2.5 dB higher SNR is required as a result of implementing this algorithm.

- **Experimental demonstration of OIFDM transmission using a real time transceiver:** Real time experimental demonstration of OIFDM transmission is critical for evaluating the true potential of the OIFDM transmission.

- **Alternative algorithm to IFFT:** Because the coherence bandwidth of the RF channel is rather small, to reduce ISI in the RF domain, the number of required orthogonal subcarriers should be high. This requires the implementation of IFFT algorithm in order to reduce the complexity, at the cost of introducing a high PAPR time domain signal. However, the requirement of orthogonal subcarriers in VLC systems is not as high as in the RF domain, as the coherence bandwidth of VLC systems is much higher than that of RF systems. Therefore, another algorithm should be used instead of IFFT in order to make the subcarriers orthogonal in VLC systems.

- To further improve the performance of OFDM in the VLC systems, obvious research areas such as error correction codes should be widely investigated in future work.

References

[1] A. Osseiran *et al.*, "Scenarios for 5G mobile and wireless communications: the vision of the METIS project," *IEEE Communications Magazine,* vol. 52, no. 5, pp. 26-35, 2014.

[2] V. Jungnickel *et al.*, "The role of small cells, coordinated multipoint, and massive MIMO in 5G," *IEEE Communications Magazine,* vol. 52, no. 5, pp. 44-51, 2014.

[3] B. Bangerter, S. Talwar, R. Arefi, and K. Stewart, "Networks and devices for the 5G era," *IEEE Communications Magazine,* vol. 52, no. 2, pp. 90-96, 2014.

[4] F. Haider *et al.*, "Spectral efficiency analysis of mobile femtocell based cellular systems," in *Communication Technology (ICCT), 2011 IEEE 13th International Conference on*, 2011, pp. 347-351: IEEE.

[5] M. Uysal, C. Capsoni, Z. Ghassemlooy, A. Boucouvalas, and E. Udvary, *Optical wireless communications: an emerging technology*. Springer, 2016.

[6] Z. Ghassemlooy, W. Popoola, and S. Rajbhandari, *Optical wireless communications: system and channel modelling with Matlab®*. CRC Press, 2012.

[7] Z. Ghassemlooy, L. N. Alves, S. Zvanovec, and M.-A. Khalighi, *Visible Light Communications: Theory and Applications*. CRC Press, 2017.

[8] T. Komine and M. Nakagawa, "Fundamental analysis for visible-light communication system using LED lights," *Consumer Electronics, IEEE Transactions on,* vol. 50, no. 1, pp. 100-107, 2004.

[9] L.-M. Hoa *et al.*, "100-Mb/s NRZ Visible Light Communications Using a Postequalized White LED," *IEEE Photonics Technology Letters,* vol. 21, no. 15, pp. 1063-1065, 2009.

[10] S. Dimitrov and H. Haas, *Principles of LED Light Communications: Towards Networked Li-Fi*. Cambridge University Press, 2015.

[11] W. Zhaocheng, W. Qi, H. Wei, and X. Zhengyuan, "Introduction to Visible Light Communications," in *Visible Light Communications:Modulation and Signal Processing*: Wiley-IEEE Press, 2018, p. 368.

[12] P. A. Haigh, Z. Ghassemlooy, S. Rajbhandari, I. Papakonstantinou, and W. Popoola, "Visible Light Communications: 170 Mb/s Using an Artificial Neural Network Equalizer in a Low Bandwidth White Light Configuration," *Journal of Lightwave Technology,* vol. 32, no. 9, pp. 1807-1813, 2014.

[13] J. Vucic, C. Kottke, S. Nerreter, K. D. Langer, and J. W. Walewski, "513 Mbit/s Visible Light Communications Link Based on DMT-Modulation of a White LED," *Journal of Lightwave Technology, ,* vol. 28, no. 24, pp. 3512-3518, 2010.

[14] M. S. Islim and H. Haas, "Modulation Techniques for Li‐Fi," *ZTECOMMUNICATIONS,* p. 29, 2016.

[15] Y. S. Cho, J. Kim, W. Y. Yang, and C. G. Kang, *MIMO-OFDM Wireless Communications with MATLAB*. John Wiley & Sons, 2010.

[16] D. Tsonev *et al.*, "A 3-Gb/s Single-LED OFDM-Based Wireless VLC Link Using a Gallium Nitride uLED," *IEEE Photonics Technology Letters,* vol. 26, no. 7, pp. 637-640, 2014.

[17] Y. Jiang, Y. Wang, P. Cao, M. Safari, J. Thompson, and H. Haas, "Robust and Low-Complexity Timing Synchronization for DCO-OFDM LiFi Systems," *IEEE Journal on Selected Areas in Communications,* vol. 36, no. 1, pp. 53-65, 2018.

[18] A. A. Abdulkafi, M. Y. Alias, and Y. S. Hussein, "Performance analysis of DCO-OFDM in VLC system," in *Communications (MICC), 2015 IEEE 12th Malaysia International Conference on*, 2015, pp. 163-168: IEEE.

[19] S. D. Mohamed, H. S. Khallaf, H. Shalaby, I. Andonovic, and M. H. Aly, "Two approaches for the modified asymmetrically clipped optical orthogonal frequency division multiplexing system," in *Electronics, Communications and Computers (JEC-ECC), 2013 Japan-Egypt International Conference on*, 2013, pp. 135-139.

[20] S. C. J. Lee, S. Randel, F. Breyer, and A. M. J. Koonen, "PAM-DMT for Intensity-Modulated and Direct-Detection Optical Communication Systems," *IEEE Photonics Technology Letters,* vol. 21, no. 23, pp. 1749-1751, 2009.

[21] F. R. Ávila and L. Lovisolo, "Unsupervised time domain nonlinear post-equalization for ACO-OFDM visible light communication systems," in *Signal Processing Conference (EUSIPCO), 2017 25th European*, 2017, pp. 848-852: IEEE.

[22] J. Xu, W. Xu, H. Zhang, and X. You, "Asymmetrically reconstructed optical OFDM for visible light communications," *IEEE Photonics Journal,* vol. 8, no. 1, pp. 1-18, 2016.

[23] R. Mesleh, "OFDM and SCFDE performance comparison for indoor optical wireless communication systems," in *Telecommunications (ICT), 2012 19th International Conference on*, 2012, pp. 1-5.

[24] K. Acolatse, Y. Bar-Ness, and S. K. Wilson, "Single carrier frequency domain equalization for optical wireless communications," 2015.

[25] C. Wu, H. Zhang, and W. Xu, "On visible light communication using LED array with DFT-Spread OFDM," in *2014 IEEE International Conference on Communications (ICC)*, 2014, pp. 3325-3330.

[26] A. W. Azim, Y. Le Guennec, and G. Maury, "Hermitian symmetry free optical-single-carrier frequency division multiple access for visible light communication," *Optics Communications,* vol. 415, pp. 177-185, 2018.

[27] O. Saied *et al.*, "Single carrier optical FDM in visible light communication," in *Communication Systems, Networks and Digital Signal Processing (CSNDSP), 2016 10th International Symposium on*, 2016, pp. 1-5: IEEE.

[28] H. Liu and G. Li, *OFDM-based broadband wireless networks: design and optimization*. John Wiley & Sons, 2005.

[29] H. Rohling, *OFDM: concepts for future communication systems*. Springer Science & Business Media, 2011.

[30] R. v. Nee and R. Prasad, *OFDM for wireless multimedia communications*. Artech House, Inc., 2000.

[31] K. Fazel and S. Kaiser, *Multi-carrier and Spread Spectrum Systems: From OFMD and MC-CDMA to LTE and WiMAX*. John Wiley & Sons, 2008.

[32] J. Zyren and W. McCoy, "Overview of the 3GPP long term evolution physical layer," *Freescale Semiconductor, Inc., white paper,* 2007.

[33] L. L. Hanzo, Y. Akhtman, L. Wang, and M. Jiang, *MIMO-OFDM for LTE, WiFi and WiMAX: Coherent versus non-coherent and cooperative turbo transceivers*. John Wiley & Sons, 2010.

[34] J. B. Carruthers and J. M. Kahn, "Multiple-subcarrier modulation for nondirected wireless infrared communication," *IEEE Journal on Selected Areas in Communications,* vol. 14, no. 3, pp. 538-546, 1996.

[35] M. Z. Afgani, H. Haas, H. Elgala, and D. Knipp, "Visible light communication using OFDM," in *2nd International Conference on Testbeds and Research Infrastructures for the Development of Networks and Communities* 2006, pp. 6 -134.

[36] S. K. Hashemi, Z. Ghassemlooy, L. Chao, and D. Benhaddou, "Orthogonal frequency division multiplexing for indoor optical wireless communications using visible light LEDs," in *Communication Systems, Networks and Digital Signal Processing, 2008. CNSDSP 2008. 6th International Symposium on*, 2008, pp. 174-178.

[37] A. H. Azhar, T. Tran, and D. O'Brien, "A Gigabit/s Indoor Wireless Transmission Using MIMO-OFDM Visible-Light Communications," *Photonics Technology Letters, IEEE,* vol. 25, no. 2, pp. 171-174, 2013.

[38] W. Shieh and I. Djordjevic, "Orthogonal frequency division multiplexing for optical communication," *ELSEVIER Inc.,* pp. 38-39, 2010.

[39] A. Goldsmith, *Wireless communications*. Cambridge university press, 2005.

[40] A. R. Bahai, B. R. Saltzberg, and M. Ergen, *Multi-carrier digital communications: theory and applications of OFDM*. Springer Science & Business Media, 2004.

[41] F. Xiong, *Digital modulation techniques*. Artech House, 2006.

[42]   T. S. Rappaport, "Wireless Communications--Principles and Practice, (The Book End)," *Microwave Journal,* vol. 45, no. 12, pp. 128-129, 2002.

[43]   H. A. L. Al-Sodani, "New OFDM schemes based on orthogonal transforms for mobile communications systems," 2013.

[44]   U. I. Butt, *A Study On The Tone-Reservation Technique For Peak-To-Average Power Ratio Reduction In Ofdm Systems*. Universal-Publishers, 2010.

[45]   R. W. Chang, "Orthogonal frequency multiplex data transmission system," ed: USA U.S. Patent 3,488,445,, 1966.

[46]   R. Prasad, *OFDM for wireless communications systems*. Artech House, 2004.

[47]   G. Hill, "Peak power reduction in orthogonal frequency division multiplexing transmitters," Victoria University, 2011.

[48]   A. Goel, "Improved PAPR Reduction in OFDM Systems," 2013.

[49]   A. Peled and A. Ruiz, "Frequency domain data transmission using reduced computational complexity algorithms," in *Acoustics, Speech, and Signal Processing, IEEE International Conference on ICASSP'80.*, 1980, vol. 5, pp. 964-967: IEEE.

[50]   A. Al-Jzari and K. Iviva, "Cyclic Prefix Length Determination for Orthogonal Frequency Division Multiplexing System over Different Wireless Channel Models Based on the Maximum Excess Delay Spread," *American Journal of Engineering and Applied Sciences,* vol. 8, no. 1, p. 82, 2015.

[51]   S. Coleri, M. Ergen, A. Puri, and A. Bahai, "Channel estimation techniques based on pilot arrangement in OFDM systems," *Broadcasting, IEEE Transactions on,* vol. 48, no. 3, pp. 223-229, 2002.

[52]   M. Bogdanović, "Frequency domain based LS channel estimation in OFDM based Power line communications," *Automatika–Journal for Control, Measurement, Electronics, Computing and Communications,* vol. 55, no. 4, 2014.

[53]   W. G. Jeon, K. H. Chang, and Y. S. Cho, "An equalization technique for orthogonal frequency-division multiplexing systems in time-variant multipath channels," *IEEE Transactions on Communications,* vol. 47, no. 1, pp. 27-32, 1999.

[54]   L. Rugini, P. Banelli, and G. Leus, "Simple equalization of time-varying channels for OFDM," *IEEE Communications Letters,* vol. 9, no. 7, pp. 619-621, 2005.

[55]   P. Schniter, "Low-complexity equalization of OFDM in doubly selective channels," *IEEE Transactions on Signal Processing,* vol. 52, no. 4, pp. 1002-1011, 2004.

[56]   C. Xiaodong and G. B. Giannakis, "Bounding performance and suppressing intercarrier interference in wireless mobile OFDM," *IEEE Transactions on Communications,* vol. 51, no. 12, pp. 2047-2056, 2003.

[57]   L. Boher, R. Rabineau, and M. Helard, "An Efficient MMSE Equalizer Implementation for 4×4 MIMO-OFDM Systems in Frequency Selective Fast Varying Channels," in *2007 IEEE 18th International Symposium on Personal, Indoor and Mobile Radio Communications*, 2007, pp. 1-5.

[58]   Y. Jiang, M. K. Varanasi, and J. Li, "Performance Analysis of ZF and MMSE Equalizers for MIMO Systems: An In-Depth Study of the High SNR Regime," *IEEE Transactions on Information Theory,* vol. 57, no. 4, pp. 2008-2026, 2011.

[59]   D. Tse and P. Viswanath, *Fundamentals of wireless communication*. Cambridge university press, 2005.

[60]   T.-A. Truong, M. Arzel, H. Lin, B. Jahan, and M. Jezequel, "New low-complexity and robust time synchronization technique for optical IMDD OFDM transmissions," *Optics express,* vol. 22, no. 12, pp. 14322-14340, 2014.

[61]   K. Goroshko, K. Manolakis, L. Grobe, and V. Jungnickel, "Low-latency synchronization for OFDM-based visible light communication," in *2015 IEEE International Conference on Communication Workshop (ICCW)*, 2015, pp. 1327-1332.

[62]   M. F. G. Medina, O. González, S. Rodríguez, and I. R. Martín, "Timing synchronization for OFDM-based visible light communication system," in *2016 Wireless Telecommunications Symposium (WTS)*, 2016, pp. 1-4.

[63] S. Tian, K. Panta, H. A. Suraweera, B. J. C. S. J. C. Schmidt, S. McLaughlin, and J. Armstrong, "A novel timing synchronization method for ACO-OFDM-based optical wireless communications," *IEEE Transactions on Wireless Communications,* vol. 7, no. 12, pp. 4958-4967, 2008.

[64] M. M. Freda and J. M. Murray, "Low-complexity blind timing synchronization for ACO-OFDM-based optical wireless communications," in *2010 IEEE Globecom Workshops*, 2010, pp. 1031-1036.

[65] R. Bouziane and R. Killey, "Blind symbol synchronization for direct detection optical OFDM using a reduced number of virtual subcarriers," *Optics express,* vol. 23, no. 5, pp. 6444-6454, 2015.

[66] T. M. Schmidl and D. C. Cox, "Robust frequency and timing synchronization for OFDM," *IEEE Transactions on Communications,* vol. 45, no. 12, pp. 1613-1621, 1997.

[67] J. J. v. d. Beek, M. Sandell, and P. O. Borjesson, "ML estimation of time and frequency offset in OFDM systems," *IEEE Transactions on Signal Processing,* vol. 45, no. 7, pp. 1800-1805, 1997.

[68] H. G. Myung, L. Junsung, and D. Goodman, "Peak-To-Average Power Ratio of Single Carrier FDMA Signals with Pulse Shaping," in *Personal, Indoor and Mobile Radio Communications, 2006 IEEE 17th International Symposium on*, 2006, pp. 1-5.

[69] C. R. Berger, Y. Benlachtar, and R. Killey, "Optimum clipping for optical OFDM with limited resolution DAC/ADC," in *Signal Processing in Photonic Communications*, 2011, p. SPMB5: Optical Society of America.

[70] M. I. Abdullah, "Comparative study of PAPR reduction techniques in OFDM," 2011.

[71] B. Hanta, "Sc-fdma and lte uplink physical layer design," *Ausgewahlte Kapitel der Nachrichtentechnik, WS,* vol. 2010, 2009.

[72] B. Hanta, "SC-FDMA and LTE uplink physical layer design," *Siminar LTE: Der Mobilfunk der Zukunft, University of Erlangen-Nuremberg, LMK,* 2009.

[73] J. Lim, H. G. Myung, K. Oh, and D. J. Goodman, "Channel-Dependent Scheduling of Uplink Single Carrier FDMA Systems," in *IEEE Vehicular Technology Conference*, 2006, pp. 1-5.

[74] H. G. Myung, "Introduction to single carrier FDMA," in *2007 15th European Signal Processing Conference*, 2007, pp. 2144-2148.

[75] U. S. Jha and R. Prasad, *OFDM towards fixed and mobile broadband wireless access*. Artech House, Inc., 2007.

[76] S. Arnon, *Visible light communication*. Cambridge University Press, 2015.

[77] W. Shao-Wei *et al.*, "A high-performance blue filter for a white-led-based visible light communication system," *Wireless Communications, IEEE,* vol. 22, no. 2, pp. 61-67, 2015.

[78] J. Armstrong, Y. A. Sekercioglu, and A. Neild, "Visible light positioning: a roadmap for international standardization," *IEEE Communications Magazine,* vol. 51, no. 12, pp. 68-73, 2013.

[79] T. Q. Wang, Y. A. Sekercioglu, A. Neild, and J. Armstrong, "Position Accuracy of Time-of-Arrival Based Ranging Using Visible Light With Application in Indoor Localization Systems," *Journal of Lightwave Technology,* vol. 31, no. 20, pp. 3302-3308, 2013.

[80] S. H. Yu, O. Shih, H. M. Tsai, N. Wisitpongphan, and R. D. Roberts, "Smart automotive lighting for vehicle safety," *IEEE Communications Magazine,* vol. 51, no. 12, pp. 50-59, 2013.

[81] P. Luo, Z. Ghassemlooy, H. Le Minh, E. Bentley, A. Burton, and X. Tang, "Performance analysis of a car-to-car visible light communication system," *Applied Optics,* vol. 54, no. 7, pp. 1696-1706, 2015.

[82] S. H. Chang, "A Visible Light Communication Link Protection Mechanism for Smart Factory," in *2015 IEEE 29th International Conference on Advanced Information Networking and Applications Workshops*, 2015, pp. 733-737.

[83] H. Haas, "Visible light communication," in *2015 Optical Fiber Communications Conference and Exhibition (OFC)*, 2015, pp. 1-72.

[84] G. Corbellini, K. Aksit, S. Schmid, S. Mangold, and T. R. Gross, "Connecting networks of toys and smartphones with visible light communication," *IEEE Communications Magazine,* vol. 52, no. 7, pp. 72-78, 2014.

[85] N. O. Tippenhauer, D. Giustiniano, and S. Mangold, "Toys communicating with LEDs: Enabling toy cars interaction," in *2012 IEEE Consumer Communications and Networking Conference (CCNC)*, 2012, pp. 48-49.

[86] Y. Tanaka, S. Haruyama, and M. Nakagawa, "Wireless optical transmissions with white colored LED for wireless home links," in *11th IEEE International Symposium on Personal Indoor and Mobile Radio Communications. PIMRC 2000. Proceedings (Cat. No.00TH8525)*, 2000, vol. 2, pp. 1325-1329 vol.2.

[87] Y. Tanaka, T. Komine, S. Haruyama, and M. Nakagawa, "Indoor visible communication utilizing plural white LEDs as lighting," in *12th IEEE International Symposium on Personal, Indoor and Mobile Radio Communications. PIMRC 2001. Proceedings (Cat. No.01TH8598)*, 2001, vol. 2, pp. F-81-F-85 vol.2.

[88] S. Rajagopal, R. D. Roberts, and S. K. Lim, "IEEE 802.15.7 visible light communication: modulation schemes and dimming support," *IEEE Communications Magazine,* vol. 50, no. 3, pp. 72-82, 2012.

[89] H. Chun *et al.*, "LED Based Wavelength Division Multiplexed 10 Gb/s Visible Light Communications," *Journal of Lightwave Technology,* vol. 34, no. 13, pp. 3047-3052, 2016.

[90] Y. Wang, L. Tao, X. Huang, J. Shi, and N. Chi, "8-Gb/s RGBY LED-Based WDM VLC System Employing High-Order CAP Modulation and Hybrid Post Equalizer," *IEEE Photonics Journal,* vol. 7, no. 6, pp. 1-7, 2015.

[91] "TG7r1, Technical Considerations Document," July 2015.

[92] A. Tsiatmas, C. P. M. J. Baggen, F. M. J. Willems, J. P. M. G. Linnartz, and J. W. M. Bergmans, "An illumination perspective on visible light communications," *IEEE Communications Magazine,* vol. 52, no. 7, pp. 64-71, 2014.

[93] A. Buckley, *Organic light-emitting diodes (OLEDs): Materials, devices and applications*. Elsevier, 2013.

[94] J. Vučić, C. Kottke, K. Habel, and K. D. Langer, "803 Mbit/s visible light WDM link based on DMT modulation of a single RGB LED luminary," in *2011 Optical Fiber Communication Conference and Exposition and the National Fiber Optic Engineers Conference*, 2011, pp. 1-3.

[95] S. Rajbhandari, "Spatial and wavelength division multiplexing for high-speed VLC systems: An overview," in *2016 10th International Symposium on Communication Systems, Networks and Digital Signal Processing (CSNDSP)*, 2016, pp. 1-6.

[96] R. Kraemer and M. Katz, *Short-range wireless communications: emerging technologies and applications*. John Wiley & Sons, 2009.

[97] A. A. Bergh and J. A. Copeland, "Optical sources for fiber transmission systems," *Proceedings of the IEEE,* vol. 68, no. 10, pp. 1240-1247, 1980.

[98] J. Grubor, S. C. J. Lee, K. D. Langer, T. Koonen, and J. W. Walewski, "Wireless High-Speed Data Transmission with Phosphorescent White-Light LEDs," in *33rd European Conference and Exhibition of Optical Communication - Post-Deadline Papers (published 2008)*, 2007, pp. 1-2.

[99] R. X. G. Ferreira *et al.*, "High Bandwidth GaN-Based Micro-LEDs for Multi-Gb/s Visible Light Communications," *IEEE Photonics Technology Letters,* vol. 28, no. 19, pp. 2023-2026, 2016.

[100] W. O. Popoola and H. Haas, "Demonstration of the Merit and Limitation of Generalised Space Shift Keying for Indoor Visible Light Communications," *Journal of Lightwave Technology,* vol. 32, no. 10, pp. 1960-1965, 2014.

[101] X. Huang, J. Shi, J. Li, Y. Wang, and N. Chi, "A Gb/s VLC Transmission Using Hardware Preequalization Circuit," *IEEE Photonics Technology Letters,* vol. 27, no. 18, pp. 1915-1918, 2015.

[102] H. L. Minh *et al.*, "High-Speed Visible Light Communications Using Multiple-Resonant Equalization," *IEEE Photonics Technology Letters,* vol. 20, no. 14, pp. 1243-1245, 2008.

[103] K. Burse, R. N. Yadav, and S. C. Shrivastava, "Channel Equalization Using Neural Networks: A Review," *IEEE Transactions on Systems, Man, and Cybernetics, Part C (Applications and Reviews),* vol. 40, no. 3, pp. 352-357, 2010.

[104]   F. Jiuchao, C. K. Tse, and F. C. M. Lau, "A neural-network-based channel-equalization strategy for chaos-based communication systems," *IEEE Transactions on Circuits and Systems I: Fundamental Theory and Applications,* vol. 50, no. 7, pp. 954-957, 2003.

[105]   D. Tsonev, S. Videv, and H. Haas, "Unlocking Spectral Efficiency in Intensity Modulation and Direct Detection Systems," *IEEE Journal on Selected Areas in Communications,* vol. 33, no. 9, pp. 1758-1770, 2015.

[106]   P. A. Haigh *et al.*, "Multi-band carrier-less amplitude and phase modulation for bandlimited visible light communications systems," *IEEE Wireless Communications,* vol. 22, no. 2, pp. 46-53, 2015.

[107]   H. Elgala, R. Mesleh, and H. Haas, "Non-linearity effects and predistortion in optical OFDM wireless transmission using LEDs," *International Journal of Ultra Wideband Communications and Systems,* vol. 1, no. 2, pp. 143-150, 2009.

[108]   C. Ma, H. Zhang, K. Cui, M. Yao, and Z. Xu, "Effects of LED lighting degradation and junction temperature variation on the performance of visible light communication," in *Systems and Informatics (ICSAI), 2012 International Conference on*, 2012, pp. 1596-1600: IEEE.

[109]   S. Dimitrov and H. Haas, "Optimum Signal Shaping in OFDM-Based Optical Wireless Communication Systems," in *2012 IEEE Vehicular Technology Conference (VTC Fall)*, 2012, pp. 1-5.

[110]   !!! INVALID CITATION !!!

[111]   F. Miramirkhani, M. Uysal, and E. Panayirci, "Channel modeling for visible light communications," in *Optical Wireless Communications*: Springer, 2016, pp. 107-122.

[112]   H. Chun, C.-J. Chiang, and D. C. O'Brien, "Visible light communication using OLEDs: Illumination and channel modeling," in *Optical Wireless Communications (IWOW), 2012 International Workshop on*, 2012, pp. 1-3: IEEE.

[113]   T. Komine and M. Nakagawa, "Performance evaluation of visible-light wireless communication system using white LED lightings," in *Computers and Communications, 2004. Proceedings. ISCC 2004. Ninth International Symposium on*, 2004, vol. 1, pp. 258-263 Vol.1.

[114]   H. Q. Nguyen *et al.*, "A MATLAB-based simulation program for indoor visible light communication system," in *2010 7th International Symposium on Communication Systems, Networks & Digital Signal Processing (CSNDSP 2010)*, 2010, pp. 537-541.

[115]   K. Lee, H. Park, and J. R. Barry, "Indoor Channel Characteristics for Visible Light Communications," *IEEE Communications Letters,* vol. 15, no. 2, pp. 217-219, 2011.

[116]   K. Fan, T. Komine, Y. Tanaka, and M. Nakagawa, "The effect of reflection on indoor visible-light communication system utilizing white LEDs," in *Wireless Personal Multimedia Communications, 2002. The 5th International Symposium on*, 2002, vol. 2, pp. 611-615 vol.2.

[117]   V. Jungnickel *et al.*, "A European view on the next generation optical wireless communication standard," in *2015 IEEE Conference on Standards for Communications and Networking (CSCN)*, 2015, pp. 106-111.

[118]   W. Gu, M. Aminikashani, P. Deng, and M. Kavehrad, "Impact of Multipath Reflections on the Performance of Indoor Visible Light Positioning Systems," *Journal of Lightwave Technology,* vol. 34, no. 10, pp. 2578-2587, 2016.

[119]   Z. Chen, D. Tsonev, and H. Haas, "Improving SINR in indoor cellular visible light communication networks," in *2014 IEEE International Conference on Communications (ICC)*, 2014, pp. 3383-3388.

[120]   P. Chvojka, S. Zvanovec, P. A. Haigh, and Z. Ghassemlooy, "Channel Characteristics of Visible Light Communications Within Dynamic Indoor Environment," *Journal of Lightwave Technology,* vol. 33, no. 9, pp. 1719-1725, 2015.

[121]   F. Miramirkhani and M. Uysal, "Channel modeling and characterization for visible light communications," *IEEE Photonics Journal,* vol. 7, no. 6, pp. 1-16, 2015.

[122]   H. Haas, L. Yin, Y. Wang, and C. Chen, "What is LiFi?," *Journal of Lightwave Technology,* vol. 34, no. 6, pp. 1533-1544, 2016.

[123] M. B. Rahaim, A. M. Vegni, and T. D. C. Little, "A hybrid Radio Frequency and broadcast Visible Light Communication system," in *2011 IEEE GLOBECOM Workshops (GC Wkshps)*, 2011, pp. 792-796.

[124] Y. Qiu, H. H. Chen, and W. X. Meng, "Channel modeling for visible light communications—A survey," *Wireless Communications and Mobile Computing,* 2016.

[125] A. Jovicic, J. Li, and T. Richardson, "Visible light communication: opportunities, challenges and the path to market," *IEEE Communications Magazine,* vol. 51, no. 12, pp. 26-32, 2013.

[126] J. Vučić *et al.*, "230 Mbit/s via a wireless visible-light link based on OOK modulation of phosphorescent white LEDs," in *Optical Fiber Communication Conference*, 2010, p. OThH3: Optical Society of America.

[127] N. Fujimoto and H. Mochizuki, "477 Mbit/s visible light transmission based on OOK-NRZ modulation using a single commercially available visible LED and a practical LED driver with a pre-emphasis circuit," in *National Fiber Optic Engineers Conference*, 2013, p. JTh2A. 73: Optical Society of America.

[128] Z. Yu, K. Ying, R. J. Baxley, and G. T. Zhou, "PAPR reduction for bit-loaded OFDM in visible light communications," in *2015 IEEE Wireless Communications and Networking Conference (WCNC)*, 2015, pp. 334-339.

[129] A. M. Khalid, G. Cossu, R. Corsini, P. Choudhury, and E. Ciaramella, "1-Gb/s Transmission Over a Phosphorescent White LED by Using Rate-Adaptive Discrete Multitone Modulation," *IEEE Photonics Journal,* vol. 4, no. 5, pp. 1465-1473, 2012.

[130] G. Cossu, A. Khalid, P. Choudhury, R. Corsini, and E. Ciaramella, "3.4 Gbit/s visible optical wireless transmission based on RGB LED," *Optics express,* vol. 20, no. 26, pp. B501-B506, 2012.

[131] F. M. Wu *et al.*, "Performance Comparison of OFDM Signal and CAP Signal Over High Capacity RGB-LED-Based WDM Visible Light Communication," *IEEE Photonics Journal,* vol. 5, no. 4, pp. 7901507-7901507, 2013.

[132] J. Armstrong and A. J. Lowery, "Power efficient optical OFDM," *Electronics Letters,* vol. 42, no. 6, pp. 370-372, 2006.

[133] S. C. J. Lee, S. Randel, F. Breyer, and A. J. Koonen, "PAM-DMT for intensity-modulated and direct-detection optical communication systems," *Photonics Technology Letters, IEEE,* vol. 21, no. 23, pp. 1749-1751, 2009.

[134] R. Mesleh, H. Elgala, and H. Haas, "On the performance of different OFDM based optical wireless communication systems," *Optical Communications and Networking, IEEE/OSA Journal of,* vol. 3, no. 8, pp. 620-628, 2011.

[135] K. Acolatse, Y. Bar-Ness, and S. K. Wilson, "Single Carrier Frequency Domain Equalization for Optical Wireless Communications."

[136] S. D. Dissanayake and J. Armstrong, "Comparison of ACO-OFDM, DCO-OFDM and ADO-OFDM in IM/DD systems," *Lightwave Technology, Journal of,* vol. 31, no. 7, pp. 1063-1072, 2013.

[137] J. Tellado, *Multicarrier modulation with low PAR: applications to DSL and wireless*. Springer Science & Business Media, 2006.

[138] S. Deka, P. Saengudomlert, and S. Baruah, "Dimming Consideration for OFDM-Based Visible Light Communications," *ADBU Journal of Engineering Technology,* vol. 2, no. 1, 2015.

[139] Z. Wang, Q. Wang, S. Chen, and L. Hanzo, "An adaptive scaling and biasing scheme for OFDM-based visible light communication systems," *Optics express,* vol. 22, no. 10, pp. 12707-12715, 2014.

[140] J. Armstrong, B. Schmidt, D. Kalra, H. A. Suraweera, and A. J. Lowery, "SPC07-4: Performance of asymmetrically clipped optical OFDM in AWGN for an intensity modulated direct detection system," in *Global Telecommunications Conference, 2006. GLOBECOM '06. IEEE*, 2006, pp. 1-5.

[141] J. Armstrong and B. Schmidt, "Comparison of asymmetrically clipped optical OFDM and DC-biased optical OFDM in AWGN," *Communications Letters, IEEE,* vol. 12, no. 5, pp. 343-345, 2008.

[142] S. D. Dissanayake, K. Panta, and J. Armstrong, "A novel technique to simultaneously transmit ACO-OFDM and DCO-OFDM in IM/DD systems," in *GLOBECOM Workshops (GC Wkshps), 2011 IEEE*, 2011, pp. 782-786.

[143] W. Qi, W. Zhaocheng, and D. Linglong, "Asymmetrical Hybrid Optical OFDM for Visible Light Communications With Dimming Control," *Photonics Technology Letters, IEEE,* vol. 27, no. 9, pp. 974-977, 2015.

[144] F. Yang, J. Gao, and S. Liu, "Novel Visible Light Communication Approach Based on Hybrid OOK and ACO-OFDM," *IEEE Photonics Technology Letters,* vol. 28, no. 14, pp. 1585-1588, 2016.

[145] K. Asadzadeh, "Efficient OFDM Signaling Schemes For Visible Light Communication Systems," 2011.

[146] H. Elgala, R. Mesleh, and H. Haas, "Practical considerations for indoor wireless optical system implementation using OFDM," in *Telecommunications, 2009. ConTEL 2009. 10th International Conference on*, 2009, pp. 25-29.

[147] Midas.components.ltd. (2009). *A 1W white LED with PCB (HPB8-49KxWDx)*. Available: http://www.midascomponents.co.uk/pdf/HPB8-49KxWx.pdf

[148] O. Narmanlioglu, R. C. Kizilirmak, and M. Uysal, "The impact of pulse shaping filters on OFDM-based visible light communications," in *2016 IEEE 10th International Conference on Application of Information and Communication Technologies (AICT)*, 2016, pp. 1-4.

[149] D. Tsonev, S. Sinanović, and H. Haas, "Pulse shaping in unipolar OFDM-based modulation schemes," in *2012 IEEE Globecom Workshops*, 2012, pp. 1208-1212.

[150] THORLABS. (2006). *PDA36A-EC - Si Switchable Gain Detector, 350-1100 nm, 10 MHz BW, 13 mm2, M4 Taps* Available: https://www.thorlabs.com/thorproduct.cfm?partnumber=PDA36A-EC

[151] A. Lipovac, B. Modlic, and M. Grgic, "OFDM error floor based EVM estimation," in *2016 24th International Conference on Software, Telecommunications and Computer Networks (SoftCOM)*, 2016, pp. 1-5.

[152] X. Liu, F. Effenberger, N. Chand, Z. Lei, and L. Huafeng, "Demonstration of bandwidth-efficient mobile fronthaul enabling seamless aggregation of 36 E-UTRA-like wireless signals in a single 1.1-GHz wavelength channel," in *2015 Optical Fiber Communications Conference and Exhibition (OFC)*, 2015, pp. 1-3.

[153] H. Li *et al.*, "Improving performance of mobile fronthaul architecture employing high order delta-sigma modulator with PAM-4 format," *Optics express,* vol. 25, no. 1, pp. 1-9, 2017.

[154] S. C. Yang, *OFDMA system analysis and design*. Artech House, 2010.

[155] R. M. Gray, "Identification and Classification of Orthogonal Frequency Division Multiple Access (OFDMA) Signals used in next generation wireless systems," NAVAL POSTGRADUATE SCHOOL MONTEREY CA DEPT OF ELECTRICAL AND COMPUTER ENGINEERING2012.

[156] Ettus.Research. (2014). *USRP™ N200/N210 networked series*. Available: https://www.ettus.com/content/files/07495_Ettus_N200-210_DS_Flyer_HR_1.pdf

[157] N. INSTRUMENTS. (2017). *USRP-2922 Block Diagram*. Available: http://zone.ni.com/reference/en-XX/help/373380G-01/usrphelp/2922_block_diagram/

[158] Ettus.Research. (2016). *About USRP Bandwidths and Sampling Rates*. Available: https://kb.ettus.com/About_USRP_Bandwidths_and_Sampling_Rates

[159] N. Instruments. (2013, 08/09/2018). *GETTING STARTED GUIDE NI USRP -29xx* Available: http://eduscol.education.fr/sti/sites/eduscol.education.fr.sti/files/ressources/techniques/3801/3801-guide-configuration-usrp-29xx.pdf

[160] N. Instruments. (2017, 01/08/2018). *niUSRP Configure Signal VI*. Available: http://zone.ni.com/reference/en-XX/help/373380G-01/usrpviref/niusrp_configure_signal/

[161] S. Yao and X. Zhang, "Joint Beamforming and DC Bias Optimization in VLC with Dimming Control," in *2017 IEEE 85th Vehicular Technology Conference (VTC Spring)*, 2017, pp. 1-5.

[162] R. C. Kizilirmak and K. Yau Hee, "On the brightness control of ACO-OFDM based VLC systems," in *2015 9th International Conference on Sensing Technology (ICST)*, 2015, pp. 215-218.

[163]   ALLDATASHEET.COM. (2008, 13/02/2018). *SFH4230 Datasheet (PDF) - OSRAM GmbH*. Available: http://www.alldatasheet.com/datasheet-pdf/pdf/218333/OSRAM/SFH4230.html

[164]   Juan Garcia, Stephen G. LaJeunesse, and D. Bartow, "Measuring Spurious Free Dynamic Range in a D/A Converter," *Intersil, Tech. Rep. TB326, January 1995,* 1998.